

The effect of temperature on flow properties of powders

Igino Tomasetta



**UNIVERSITÀ DEGLI STUDI
DI SALERNO**

Department of Industrial Engineering

*Ph.D. Course in Chemical Engineering
(X Cycle-New Series)*

**The effect of temperature
on flow properties of powders**

Supervisors

Prof. Massimo Poletto

Dr. Diego Barletta

Ph.D. student

Igino Tomasetta

Scientific Referee

Prof. Roberto Pantani

Ph.D. Course Coordinator

Prof. Paolo Ciambelli

Acknowledgments

PhD is an important goal for everyone that loves researching as me. However, I could never do that without the contribution of some important people which accompanied me in this experience.

First of all, I want to express my gratitude to my scientific supervisors Prof. Massimo Poletto and Dr. Diego Barletta for their precious guide and contributions during my entire PhD course.

I also would like to thank the scientific referee Prof. Roberto Pantani for his helpfulness and his wise advices in the final period of PhD course.

Thanks to all my PhD colleagues of X cycle and all the people that worked in I2 lab during last three years with which I shared every good and bad times of this unique experience. In particular, a special thank goes to Dr. Mariarosa Scognamiglio and to the Supercritical Fluids Research Group for their valid support, especially in DSC analysis and SEM visualizations.

My dearest thank goes to all my “brothers” of the Franciscan Youth. Their support and the continuous relation with people that wants only my best helps me to interrogate myself about the true meaning of life and to experiment the real and unselfish Love.

I am deeply grateful to my family for their lovely and irreplaceable support. To my father Tonino, my mother Pina, my brother Pasquale and my grandmothers Anna and Iolanda goes my infinite thanks for all the words and gestures with which they encouraged me to believe in myself and to pursue this goal despite the troubles.

Finally, thanks to You, my Lord. Only at the end of this way I can see your merciful work. Despite my doubts and human frailties, through this people You did not cease to help me and to be close to me, because “*when I am weak, then I am strong*” (2 Cor 12, 10). Thank You!

List of publications

Refereed Journals

Tomasetta, I., Barletta, D., Lettieri, P., Poletto, M., 2012, The measurement of powder flow properties with a mechanically stirred Fluidized Bed Rheometer, *Chemical Engineering Science*, **69**, 373-381

Conference Proceedings

Tomasetta, I., Landi, G., Barletta, D., Poletto, M., A shear cell for the measurement of powder flow properties at high temperature, Proc. of the 6th *World Congress on Particle Technology*, April 26-29, 2010, Nuremberg (Germany).

Tomasetta, I., Barletta, D., Poletto, M., Flow properties of powders at high temperature, Proc. of *Bulk Solid Europe 2010*, September 9-10, 2010, Glasgow (Scotland)

Conference Presentations

Bruni, G., Tomasetta, I., Barletta, D., Poletto, M., Lettieri, P., Sensitivity analysis on a rheological model for the flowability of aerated fine powders, Proc. of 9th *International Conference of Chemical and Process Engineering*, May 10-13, 2009, Rome (Italy). In: *Chemical Engineering Transactions*, **17**, 735-740.

Tomasetta, I., Barletta, D., Poletto, M., The effect of temperature on flow properties of fine powders. Proc. of 10th *International Conference of Chemical and Process Engineering*, May 8-11, 2011, Florence (Italy). In: *Chemical Engineering Transactions*, **24**, 655-660.

Index

Index	I
List of figures	III
List of tables	IX
Abstract	XI
Introduction	1
I The state of the art	3
I.1 Particle characterization of granular material	3
I.2 Density of a bulk solid	4
I.3 The interparticle forces	4
I.3.1 Van der Waals' forces	5
I.3.2 Electrostatic forces	6
I.3.3 Capillary forces	7
I.3.4 Comparison of interparticle forces	9
I.3.5 Measurements of the interparticle forces at high temperature	9
I.4 Flow properties of powders	10
I.4.1 The Mohr-Coulomb failure criterion	11
I.4.2 Measurement of the failure and flow properties of powders	13
I.4.2.1 Measurement of flow properties at high temperature - A literature survey	17
I.5 Fluidization	19
I.5.1 The effect of temperature on the fluidization behaviour	23
I.6 The particle-particle approach	25
I.6.1 The dependence of the contact forces on previous consolidation	26
II The aim of the work	29

III Experimental	33
III.1 High Temperature Annular Shear Cell (HT-ASC)	33
III.1.1 Set-up of the High Temperature Annular Shear Cell	36
III.1.2 Procedure with the High Temperature Annular Shear Cell	38
III.2 Scanning Electron Microscope (SEM)	38
III.3 Differential Scanning Calorimeter (DSC)	39
III.4 Materials	41
IV Experimental results	45
IV.1 SEM magnifications	45
IV.2 DSC analysis	45
IV.3 Experimental measurements of flow properties with HT-ASC	49
IV.3.1 FCC powder	50
IV.3.2 Fly ashes	53
IV.3.3 Corundum	54
IV.3.4 Alumina	55
IV.3.5 Glass beads	57
IV.3.6 Glass beads mixed with 1%w of high density polyethylene	59
V Model results and sensitivity analysis	63
V.1 Estimate of the mean curvature radius at contact points	63
V.2 Sensitivity analysis on the theoretical framework	66
V.2.1 FCC powder	67
V.2.2 Corundum	67
V.2.3 Alumina	70
V.2.4 Glass beads	76
V.3 Discussion about the results of the sensitivity analysis	79
Conclusions	81
References	85
List of symbols	89
Appendix A	
The exact analysis of the transmission of stresses in a packed bed	93

List of figures

Figure I.1 <i>Schematic representation of a liquid bridge between particles.</i>	7
Figure I.2 <i>Comparison of the magnitude of interparticle forces. Dashed lines indicate asperity-to-plane contact. Theoretical interparticle forces for single-point contact between equal spheres in air, with particle weight plotted for comparison (Seville et al., 1998).</i>	8
Figure I.3 <i>Schematic representation of the HTMFB: (1) DC motor + axial linear actuator; (2) micromanipulators; (3) heating element + thermocouple; (4) objective + digital camera; (5) LVDT displacement sensor; (6) flexure strip assembly (Pagliai et al., 2004).</i>	9
Figure I.4 <i>Mohr analysis (Neddermann, 1992).</i>	11
Figure I.5 <i>The internal yield locus and the Mohr-Coulomb criterion: (i) $\tau > \mu\sigma + C$; (ii) $\tau = \mu\sigma + C$; (iii) $\tau < \mu\sigma + C$.</i>	12
Figure I.6 <i>The flow function and the Jenike classification of granular materials (Jenike, 1964).</i>	13
Figure I.7 <i>Jenike shear cell. (a) base; (b) ring; (c) lid (Standard Shear Testing Technique, 1989).</i>	14
Figure I.8 <i>Measurement of the yield locus with a shear cell: schematic of the experimental procedure.</i>	14
Figure I.9 <i>The internal yield locus and the main flow and failure parameters.</i>	15
Figure I.10 <i>Schematic of the annular Schulze shear cell (Schulze, 1994).</i>	16
Figure I.11 <i>Schematic of the split-type tensile strength system on high temperature conditions (Kamiya et al., 2002).</i>	18
Figure I.12 <i>The pressure drop across the bed and the bed height as a function of the superficial velocity for a Geldart group A powder.</i>	20

Figure I.13 Geldart's classification of powders.	21
Figure II.1 A concept map represented the logical steps correlating a continuum to a particle-particle approach.	30
Figure III.1 Schematic of the High Temperature Annular Shear Cell.	33
Figure III.2 The annular Schulze Shear Cell SV10.	34
Figure III.3 The modified High Temperature Annular Shear Cell.	35
Figure III.4 Logic of the temperature control of the High Temperature Annular Shear Cell.	35
Figure III.5 Temperature vs. time inside the High Temperature Annular Shear Cell. Solid line (—): set point temperature, T_{SP} . Dashed line (---): lower temperature, T_{DOWN} . Dotted line (···): middle temperature, T_{MID} . Dash-dotted line (-·-·): upper temperature, T_{UP} .	36
Figure III.6 Comparison between yield loci measurements for the FCC powder obtained at 20°C with the SV10 Shear Cell (○, $\sigma_1 = 997$ Pa; □, $\sigma_1 = 1211$ Pa) and the High Temperature Annular Shear Cell (◻, $\sigma_1 = 981$ Pa; †, $\sigma_1 = 1205$ Pa).	37
Figure III.7 Schematic of the Scanning Electron Microscope (SEM).	38
Figure III.8 The Scanning Electron Microscope (SEM) ASSIGN mod. LEO 420 (Department of Industrial Engineering, University of Salerno).	39
Figure III.9 Schematic of the Differential Scanning Calorimetry (DSC): (a) power compensation DSC; (b) heat-flux DSC.	40
Figure III.10 Schematic representation of an experimental DSC curve indicating typical phenomena occurring during the analysis: (A) change of the heat capacity; (B), endothermic process; (C), exothermic process.	41
Figure III.11 Particle size distributions of experimental materials (for each class, $d_{i+1}/d_i = 1.148$). Solid line (—): FCC powder. Dotted line (···): fly ashes. Short dashed line (---): corundum. Dash-dotted line (-·-·): porous alumina. Long dashed line (---): glass beads.	43
Figure IV.1 SEM magnifications of experimental materials; (a) FCC powder ($X = 1000$); (b) fly ashes ($X = 500$); (c) corundum ($X = 500$); (d) porous alumina ($X = 1000$); (e) Glass beads ($X = 200$); (f) Glass beads mixed with HDPE (1%w) ($X = 100$).	46
Figure IV.2 DSC analysis of FCC powder before (a) and after (b) the drying of the sample at 200°C. Solid line (—): increasing temperature. Dotted line (···): decreasing temperature.	47

- Figure IV.3** DSC analysis of fly ashes. Solid line (—): increasing temperature. Dotted line (⋯): decreasing temperature. 48
- Figure IV.4** DSC analysis of corundum powder. Solid line (—): increasing temperature. Dotted line (⋯): decreasing temperature. 48
- Figure IV.5** DSC analysis of porous alumina. Solid line (—): increasing temperature. Dotted line (⋯): decreasing temperature. 49
- Figure IV.6** DSC analysis of glass beads. Solid line (—): increasing temperature. Dotted line (⋯): decreasing temperature. 49
- Figure IV.7** DSC analysis of high-density polyethylene. Solid line (—): increasing temperature. Dotted line (⋯): decreasing temperature. 50
- Figure IV.8** Measured yield loci for FCC powder with HT-ASC at (a) $\sigma_1 \approx 1000$ Pa (○: $\sigma_1 = 997$ Pa, $T = 20^\circ\text{C}$; ◻: $\sigma_1 = 1004$ Pa, $T = 500^\circ\text{C}$) and (b) $\sigma_1 \approx 1200$ Pa (◻: $\sigma_1 = 1205$ Pa, $T = 20^\circ\text{C}$; ×: $\sigma_1 = 1186$ Pa, $T = 500^\circ\text{C}$) 51
- Figure IV.9** Measured flow function of FCC powder at 20°C (●) and 500°C (▲). 52
- Figure IV.10** Measured flow function for fly ashes at 20°C (▲) and 500°C (◆). 52
- Figure IV.11** Measured yield loci for fly ashes with HT-ASC at (a) $\sigma_1 \approx 4000$ Pa (○: $\sigma_1 = 4221$ Pa, $T = 20^\circ\text{C}$; ◻: $\sigma_1 = 4336$ Pa, $T = 500^\circ\text{C}$) and (b) $\sigma_1 \approx 13500$ Pa (◻: $\sigma_1 = 13530$ Pa, $T = 20^\circ\text{C}$; ◻: $\sigma_1 = 13534$ Pa, $T = 500^\circ\text{C}$). 53
- Figure IV.12** Measured flow function for corundum powder at 20°C (●) and 500°C (■). 54
- Figure IV.13** Measured yield loci for corundum powder with HT-ASC at (a) $\sigma_1 \approx 4500$ Pa (○: $\sigma_1 = 4329$ Pa, $T = 20^\circ\text{C}$; ◻: $\sigma_1 = 4652$ Pa, $T = 500^\circ\text{C}$) and (b) $\sigma_1 \approx 14000$ Pa (◻: $\sigma_1 = 14126$ Pa, $T = 20^\circ\text{C}$; ◻: $\sigma_1 = 13795$ Pa, $T = 500^\circ\text{C}$). 55
- Figure IV.14** Measured yield loci for porous alumina with HT-ASC at (a) $\sigma_1 \approx 4000$ Pa (○: $\sigma_1 = 4000$ Pa, $T = 20^\circ\text{C}$; ◻: $\sigma_1 = 4033$ Pa, $T = 500^\circ\text{C}$) and (b) $\sigma_1 \approx 13500$ Pa (◻: $\sigma_1 = 13384$ Pa, $T = 20^\circ\text{C}$; ◻: $\sigma_1 = 13654$ Pa, $T = 500^\circ\text{C}$). 56
- Figure IV.15** Measured flow function for porous alumina at 20°C (▲) and 500°C (◆). 57
- Figure IV.16** Measured flow function for glass beads at 20°C (●) and 500°C (■). 57

Figure IV.17 Measured yield loci for glass beads with HT-ASC at (a) $\sigma_1 \approx 3500$ Pa (○: $\sigma_1 = 3421$ Pa, $T = 20^\circ\text{C}$; □: $\sigma_1 = 3563$ Pa, $T = 500^\circ\text{C}$) and (b) $\sigma_1 \approx 12000$ Pa (◻: $\sigma_1 = 11689$ Pa, $T = 20^\circ\text{C}$; ◻: $\sigma_1 = 11970$ Pa, $T = 500^\circ\text{C}$). 58

Figure IV.18 Measured yield loci for the mixture of glass beads and HDPE (1%w) measured with HT-ASC at 100°C (○) and 125°C (◻) for major principal stress about 3500 Pa. 59

Figure IV.19 SEM magnification of samples of a) glass beads ($X = 80$); b) glass beads + HDPE (1%w) at room temperature ($X = 50$); c) glass beads + HDPE (1%w) after a shear test at 125°C ($X = 80$). 61

Figure V.1 FCC powder - Sensitivity analysis on the mean curvature radius δ assuming pure elastic contact. ●: $\sigma_{t,\text{exp}} - 20^\circ\text{C}$; ■: $\sigma_{t,\text{exp}} - 500^\circ\text{C}$; - - -: $\sigma_{t,\text{el}} (\delta = \delta_{\text{el}}^*)$; —: $\sigma_{t,\text{el}} (\delta = d_{\text{SV}}/20)$; ⋯: $\sigma_{t,\text{el}} (\delta = d_{\text{SV}}/100)$. 68

Figure V.2 FCC powder - Sensitivity analysis on the mean curvature radius δ assuming pure plastic contact. ●: $\sigma_{t,\text{exp}} - 20^\circ\text{C}$; ■: $\sigma_{t,\text{exp}} - 500^\circ\text{C}$; - - -: $\sigma_{t,\text{pl}} (\delta = \delta_{\text{pl}}^*)$; —: $\sigma_{t,\text{pl}} (\delta = d_{\text{SV}}/20)$; ⋯: $\sigma_{t,\text{pl}} (\delta = d_{\text{SV}}/100)$. 68

Figure V.3 FCC powder - Sensitivity analysis on the voidage ε assuming pure elastic contact. ●: $\sigma_{t,\text{exp}} - 20^\circ\text{C}$; ■: $\sigma_{t,\text{exp}} - 500^\circ\text{C}$; —: $\sigma_{t,\text{el}} (\delta = \delta_{\text{el}}^*, \varepsilon = 0.4)$; ⋯: $\sigma_{t,\text{el}} (\varepsilon = 0.36)$; - - -: $\sigma_{t,\text{el}} (\varepsilon = 0.44)$. 69

Figure V.4 FCC powder - Sensitivity analysis on the voidage ε assuming pure plastic contact. ●: $\sigma_{t,\text{exp}} - 20^\circ\text{C}$; ■: $\sigma_{t,\text{exp}} - 500^\circ\text{C}$; —: $\sigma_{t,\text{pl}} (\delta = \delta_{\text{pl}}^*, \varepsilon = 0.4)$; ⋯: $\sigma_{t,\text{pl}} (\varepsilon = 0.36)$; - - -: $\sigma_{t,\text{pl}} (\varepsilon = 0.44)$. 69

Figure V.5 FCC powder - Sensitivity analysis on the compressive strength σ_f assuming pure plastic contact. ●: $\sigma_{t,\text{exp}} - 20^\circ\text{C}$; ■: $\sigma_{t,\text{exp}} - 500^\circ\text{C}$; —: $\sigma_{t,\text{pl}} (\delta = \delta_{\text{pl}}^*)$; ⋯: $\sigma_{t,\text{pl}} (\Delta\sigma_f = +40\%)$; - - -: $\sigma_{t,\text{pl}} (\Delta\sigma_f = -40\%)$. 70

Figure V.6 Corundum - Sensitivity analysis on the mean curvature radius δ assuming pure elastic contact. ●: $\sigma_{t,\text{exp}} - 20^\circ\text{C}$; ■: $\sigma_{t,\text{exp}} - 500^\circ\text{C}$; —: $\sigma_{t,\text{el}} (\delta = d_{\text{SV}}/2)$; ⋯: $\sigma_{t,\text{el}} (\delta = d_{\text{SV}}/20)$; - - -: $\sigma_{t,\text{el}} (\delta = d_{\text{SV}}/100)$; ⋯: $\sigma_{t,\text{el}} (\delta = \delta_{\text{el}}^*)$. 71

Figure V.7 Corundum - Sensitivity analysis on the mean curvature radius δ assuming pure plastic contact. ●: $\sigma_{t,\text{exp}} - 20^\circ\text{C}$; ■: $\sigma_{t,\text{exp}} - 500^\circ\text{C}$; —: $\sigma_{t,\text{pl}} (\delta = d_{\text{SV}}/2)$; ⋯: $\sigma_{t,\text{pl}} (\delta = d_{\text{SV}}/20)$; - - -: $\sigma_{t,\text{pl}} (\delta = d_{\text{SV}}/100)$; ⋯: $\sigma_{t,\text{el}} (\delta = \delta_{\text{pl}}^*)$. 71

Figure V.8 Corundum - Sensitivity analysis on the voidage ε assuming pure elastic contact. ●: $\sigma_{t,exp} - 20^\circ\text{C}$; ■: $\sigma_{t,exp} - 500^\circ\text{C}$; —: $\sigma_{t,el} (\delta = \delta_{el}^*; \varepsilon = 0.4)$; ⋯: $\sigma_{t,el} (\varepsilon = 0.36)$; - - -: $\sigma_{t,el} (\varepsilon = 0.44)$. 72

Figure V.9 Corundum - Sensitivity analysis on the voidage ε assuming pure plastic contact. ●: $\sigma_{t,exp} - 20^\circ\text{C}$; ■: $\sigma_{t,exp} - 500^\circ\text{C}$; —: $\sigma_{t,pl} (\delta = \delta_{pl}^*; \varepsilon = 0.4)$; ⋯: $\sigma_{t,pl} (\varepsilon = 0.36)$; - - -: $\sigma_{t,pl} (\varepsilon = 0.44)$. 72

Figure V.10 Corundum - Sensitivity analysis on the compressive strength σ_f assuming pure plastic contact. ●: $\sigma_{t,exp} - 20^\circ\text{C}$; ■: $\sigma_{t,exp} - 500^\circ\text{C}$; —: $\sigma_{t,pl} (\delta = \delta_{pl}^*)$; ⋯: $\sigma_{t,pl} (\Delta\sigma_f = +40\%)$; - - -: $\sigma_{t,pl} (\Delta\sigma_f = -40\%)$. 73

Figure V.11 Alumina - Sensitivity analysis on the mean curvature radius δ assuming pure elastic contact. ●: $\sigma_{t,exp} - 20^\circ\text{C}$; ■: $\sigma_{t,exp} - 500^\circ\text{C}$; —: $\sigma_{t,el} (\delta = d_{SV}/2)$; ⋯: $\sigma_{t,el} (\delta = d_{SV}/20)$; - - -: $\sigma_{t,el} (\delta = d_{SV}/100)$; -·-: $\sigma_{t,el} (\delta = \delta_{el}^*)$. 74

Figure V.12 Alumina - Sensitivity analysis on the mean curvature radius δ assuming pure plastic contact. ●: $\sigma_{t,exp} - 20^\circ\text{C}$; ■: $\sigma_{t,exp} - 500^\circ\text{C}$; —: $\sigma_{t,pl} (\delta = d_{SV}/2)$; ⋯: $\sigma_{t,pl} (\delta = d_{SV}/20)$; - - -: $\sigma_{t,pl} (\delta = d_{SV}/100)$; -·-: $\sigma_{t,pl} (\delta = \delta_{pl}^*)$. 74

Figure V.13 Alumina - Sensitivity analysis on the voidage ε assuming pure elastic contact. ●: $\sigma_{t,exp} - 20^\circ\text{C}$; ■: $\sigma_{t,exp} - 500^\circ\text{C}$; —: $\sigma_{t,el} (\delta = \delta_{el}^*; \varepsilon = 0.4)$; ⋯: $\sigma_{t,el} (\varepsilon = 0.36)$; - - -: $\sigma_{t,el} (\varepsilon = 0.44)$. 75

Figure V.14 Alumina - Sensitivity analysis on the voidage ε assuming pure plastic contact. ●: $\sigma_{t,exp} - 20^\circ\text{C}$; ■: $\sigma_{t,exp} - 500^\circ\text{C}$; —: $\sigma_{t,pl} (\delta = \delta_{pl}^*; \varepsilon = 0.4)$; ⋯: $\sigma_{t,pl} (\varepsilon = 0.36)$; - - -: $\sigma_{t,pl} (\varepsilon = 0.44)$. 75

Figure V.15 Alumina - Sensitivity analysis on the compressive strength σ_f assuming pure plastic contact. ●: $\sigma_{t,exp} - 20^\circ\text{C}$; ■: $\sigma_{t,exp} - 500^\circ\text{C}$; —: $\sigma_{t,pl} (\delta = \delta_{pl}^*)$; ⋯: $\sigma_{t,pl} (\Delta\sigma_f = +40\%)$; - - -: $\sigma_{t,pl} (\Delta\sigma_f = -40\%)$. 76

Figure V.16 Glass beads - Sensitivity analysis on the mean curvature radius δ assuming pure elastic contact. ●: $\sigma_{t,exp} - 20^\circ\text{C}$; ■: $\sigma_{t,exp} - 500^\circ\text{C}$; —: $\sigma_{t,el} (\delta = d_{SV}/2)$; ⋯: $\sigma_{t,el} (\delta = d_{SV}/20)$; - - -: $\sigma_{t,el} (\delta = d_{SV}/100)$; -·-: $\sigma_{t,el} (\delta = \delta_{el}^*)$. 77

Figure V.17 Glass beads - Sensitivity analysis on the mean curvature radius δ assuming pure plastic contact. ●: $\sigma_{t,exp} - 20^\circ\text{C}$; ■: $\sigma_{t,exp} - 500^\circ\text{C}$; —: $\sigma_{t,pl} (\delta = d_{SV}/2)$; ⋯: $\sigma_{t,pl} (\delta = d_{SV}/10)$; - - -: $\sigma_{t,pl} (\delta = d_{SV}/100)$; -·-: $\sigma_{t,pl} (\delta = \delta_{pl}^*)$. 77

Figure V.18 *Glass beads - Sensitivity analysis on the voidage ε assuming pure elastic contact.* ●: $\sigma_{t,\text{exp}} - 20^\circ\text{C}$; ■: $\sigma_{t,\text{exp}} - 500^\circ\text{C}$; —: $\sigma_{t,\text{el}} (\delta = \delta_{\text{el}}^*; \varepsilon = 0.4)$; ⋯: $\sigma_{t,\text{el}} (\varepsilon = 0.36)$; - - -: $\sigma_{t,\text{el}} (\varepsilon = 0.44)$. 78

Figure V.19 *Glass beads - Sensitivity analysis on the voidage ε assuming pure plastic contact.* ●: $\sigma_{t,\text{exp}} - 20^\circ\text{C}$; ■: $\sigma_{t,\text{exp}} - 500^\circ\text{C}$; —: $\sigma_{t,\text{pl}} (\delta = \delta_{\text{pl}}^*; \varepsilon = 0.4)$; ⋯: $\sigma_{t,\text{pl}} (\varepsilon = 0.36)$; - - -: $\sigma_{t,\text{pl}} (\varepsilon = 0.44)$. 78

Figure V.20 *Glass beads - Sensitivity analysis on the compressive strength σ_f assuming pure plastic contact.* ●: $\sigma_{t,\text{exp}} - 20^\circ\text{C}$; ■: $\sigma_{t,\text{exp}} - 500^\circ\text{C}$; —: $\sigma_{t,\text{pl}} (\delta = \delta_{\text{pl}}^*)$; ⋯: $\sigma_{t,\text{pl}} (\Delta\sigma_f = +40\%)$; - - -: $\sigma_{t,\text{pl}} (\Delta\sigma_f = -40\%)$. 79

List of tables

Table I.1 <i>Classification of granular materials</i> (Neddermann, 1992)	3
Table I.2 <i>Expressions of van der Waals' force</i> (Masuda et al., 2006)	5
Table III.1 <i>Data of the High Temperature Annular Shear Cell</i>	34
Table III.2 <i>Material properties</i>	42
Table IV.1 <i>Results of measurements performed with HT-ASC</i>	62
Table V.1 <i>Best fitting mean curvature radius δ^* assuming elastic (δ_{el}^*) and plastic (δ_{pl}^*) deformation</i>	65

Abstract

Changes of cohesive flow properties of powders at high temperature are observed in many industrial process units, such as fluidized bed reactors, granulators and dryers. Many authors investigated the behaviour of powders at high temperature through fluidization experiments (Formisani *et al.*, 1998 and 2002; Lettieri *et al.*, 2000 and 2001), measurements of the interparticle forces (Pagliai *et al.*, 2004 and 2007) and direct measurements at the bulk level (Kamiya *et al.*, 2002). However, the understanding of the effect of temperature on interparticle interactions and flow properties of bulk solid is not clear yet.

A common approach in engineering science consists of the direct characterization of the rheology of powders like bulk solids by means of shear cells. In this work a High Temperature Annular Shear Cell, originally designed at University of Salerno, was set-up and used to measure yield loci up to 500°C and to directly evaluate the effect of temperature on the macroscopic flow properties of sample of fluid cracking catalyst powder, fly ashes, corundum, synthetic porous α -alumina and glass beads.

Different behaviour was observed for each material. The flowability of the FCC powder, fly ashes and corundum did not show change as the temperature increased differently from glass beads and, at lower extent, porous alumina for which an increment of the cohesive behaviour was observed.

In order to give an interpretation of the effect of temperature on the interparticle interactions, a theoretical framework was developed according to the particle-particle approach of Rumpf (1974) and Molerus (1985 and 1993). Furthermore, the availability of a microscopic model able to estimate quantitatively the interparticle interactions might extend the experimental findings to different compaction conditions, in particular lower than within the powder tester.

For this purpose, the tensile strength of the powder experimentally evaluated was related to contact forces acting between particles by coupling the Rumpf equation with the equation of the contact force. Only van der Waals' forces were assumed as present inside the bulk solid, according to DSC analysis performed in this work that revealed no melting points and

formation of liquid bridges for all materials in the range of operating temperature.

With this regard two alternative assumptions of elastic or plastic deformation at the contact point of particles were considered. Both the assumptions provide correct order of magnitude results in terms of tensile strength, provided that a plausible value of the local curvature at contact points of particles is taken into account by correctly considering the effect of surface roughness and asperities, according to SEM magnification performed for all the materials.

A sensitivity analysis on the main parameters of the theoretical framework was performed. Both the increasing cohesive consolidation and the slight increase of the cohesive behaviour with the temperature suggest the occurrence of the plastic deformation of the contact points and, therefore, that the plastic deformation assumption should be adopted to explain the effect of the temperature on the interparticle interactions. However, at room temperature, the effect of consolidation seems to be correctly represented considering also the decrease of the voidage.

Finally, a significant increase of the macroscopic cohesive behaviour of powder with the temperature was measured in presence of a liquid phase which promoted the aggregation of the particles, as verified with shear tests and SEM magnifications performed on sample of glass beads mixed with the low-melting temperature high-density polyethylene (HDPE) powder.

Introduction

The handling of granular materials is of the greatest importance in the chemical industry. It is estimated on a weight basis roughly one-half of the products and at least three-quarters of the raw materials are in the form of granular solids at process conditions (temperature, pressure, etc.) often different from ambient conditions.

Fluidization is one of the most common unit operation involving granular materials at high temperature. The rapid mixing and circulation of solids allows for a uniform temperature in the system. Therefore, high temperature operations in fluidized beds can be controlled simply and reliably. Other than fluidization, powders at high temperature are relevant in many others industrial applications, for instance, in the granulation, the filtering of hot gases, in the drying of pharmaceutical granules, in the curing of ceramics, in the combustion of solid fuels and regeneration of nuclear waste.

In this work, the effect of temperature on flow behaviour of powders was studied. Measurements of yield loci and flow functions of chosen materials were carried out with the High Temperature Annular Shear cell, an annular shear cell designed at University of Salerno and able to operate up to 500°C. Subsequently, a theoretical framework was applied in order to give a novel contribute to the correct interpretation of the effect of temperature on flow properties of powders and on the magnitude of the interparticle interactions.

Chapter I is a short review of the state of the art, mainly focused on the literature concerning the effect of temperature on the failure and flow properties of powders. The last section of this chapter deals with the particle-particle approach developed by Rumpf (1974) and Molerus (1993) in order to correlate bulk flow properties with interparticle interactions. This is, in fact, the approach adopted in this work for a better understanding and interpretation of the experimental results at high temperature.

The aim of this work is defined in details in Chapter II.

Chapter III describes apparatus, materials and methods employed in this PhD work. The modified High Temperature Annular Shear Cell, the set-up and the procedure of this apparatus are illustrated, such as the Scanning Electron Microscope and the Differential Scanning Calorimeter used for the

evaluation of the surface properties and of the thermal behaviour of materials. Materials data are also listed.

Chapter IV reports all the experimental results of this work. SEM magnifications, DSC analysis and shear measurements performed with HT-ASC from room temperature up to 500°C for FCC powder, fly ashes, corundum, synthetic porous α -alumina, glass beads and a mixture of glass beads and the low melting point high density polyethylene (HDPE) are showed and commented. Yield loci and flow functions evaluated at different temperature are showed and compared for all the materials.

In Chapter V, the results and a sensitivity analysis on the main parameters of the theoretical framework are reported and discussed. In particular, an interpretation of the experimental evidences is provided correlating the macroscopic flow behaviour of powders with the interparticle forces following the theory of Rumpf and Molerus described in Chapter I.

Finally, the main conclusions of this work are summarized and suggestions for the future work are proposed.

In appendix, all the mathematical steps of the particle-particle approach are reported according to the assumptions of Rumpf and Molerus.

Chapter I

The state of the art

I.1 Particle characterization of granular materials

A granular material can be defined as any material composed of many individual solid particles, irrespective of the particle size. Thus the term granular material embraces a wide variety of materials from the coarsest colliery rubble to the finest icing sugar.

Particle size and shape are basic characteristics of bulk solids and are of fundamental importance in most applications involving such material. Table I.1 lists a classification of granular materials according to size and some of the common terms relating to particle size.

In spite of their importance, no universally accepted method has yet emerged to define particle dimension. In fact, most of particles show a distribution of particle size and are normally not spherical. Therefore, the term diameter is not able to characterize the dimension of a bulk solid and it

Table I.1 *Classification of granular materials* (Neddermann, 1992)

Size range [μm]	Standard terms		Characteristics
	Component	Bulk	
30000 – 3000 (but may be as low as 1000 μm)	grain and lump	broken solid	Free-flowing, but could cause mechanical arching problems during discharge from bins and silos
1000 – 300	granule	granular solid	Easy-flowing with cohesive effects if % of fines is high
< 100	particle	powder	
(i) 100 – 10	particle	granular powder	may show cohesive effects and some handling properties
(ii) 10 – 1	particle	superfine powder	highly cohesive: very difficult to handle
(iii) <1	particle	ultrafine powder	extremely difficult (or impossible) to handle

is necessary to define an equivalent diameter as a diameter having the same value of a particular physical property as the particle of interest and a mean diameter which takes into account the particle size distribution.

Considering a distribution of particles where n_i defines the number of particles having diameter d_i , the surface mean diameter d_{SV} was defined as the diameter which preserves the volume-surface ratio of particles. Also known as *Sauter mean diameter*, it is calculated by:

$$d_{SV} = \frac{\sum_i n_i d_i^3}{\sum_i n_i d_i^2} \quad (\text{I.1})$$

Therefore, it is equally important to define parameters describing the shape of a particle. One approach is to define the sphericity ψ of the particle as:

$$\psi \equiv \frac{\text{surface area of a sphere having the same volume as the particle}}{\text{surface area of the particle}} \quad (\text{I.2})$$

Clearly, $\psi \leq 1$, where $\psi = 1$ for spherical particles. All factors remaining the same as ψ deviates from unity, the particle becomes less spherical and consequently less flowable (more cohesive) and more difficult to handle.

I.2 Density of a bulk solid

The most important characteristics of a particle are its size, its shape and its density. In a granular material, the density of particles does not correspond to the density of the bulk solid. In fact, there are two densities of interest: the density of the particles ρ_p and the density of the mixture of solid and interstitial gas, which is known as bulk density ρ_b . These are related by:

$$\rho_b = \rho_p (1 - \varepsilon) + \rho_f \varepsilon \quad (\text{I.3})$$

where ε is the void fraction, defined as the volumetric fraction of the material occupied by the interstitial fluid having density ρ_f .

The particle density ρ_p can differ from the density of the material when particle shows cavities and porosity inside. In this case, an inner voidage ε_i can be defined and related the particle density ρ_p by:

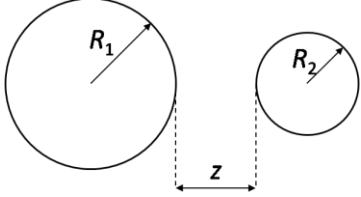
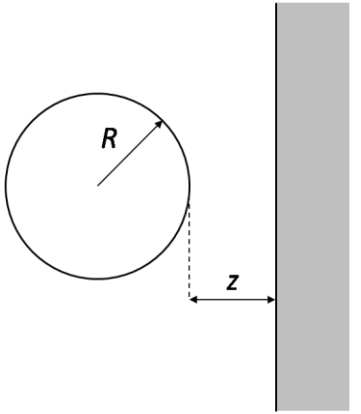
$$\rho_p = \rho_s (1 - \varepsilon_i) \quad (\text{I.4})$$

where ρ_s is density of the solid material.

I.3 The interparticle forces

The adhesive force between particles or a particle and a solid surface plays an important role in powder-handling processes. The van der Waals' force, the electrostatic force, and the capillary force are the main sources of interparticle forces. Obviously, when these forces are high, the powder becomes less free-flowing and therefore difficult to handle.

Table I.2 Expressions of van der Waals' force (Masuda *et al.*, 2006)

	$F_{\text{vdW}} = \frac{AR_1R_2}{6(R_1 + R_2)z^2} \quad (\text{I.5})$
	$F_{\text{vdW}} = -\frac{AR}{6z^2} \quad (\text{I.6})$

1.3.1 Van der Waals' forces

The Dutch physicist van der Waals was the first to point out that deviations from the ideal-gas law at high pressures could be explained by assuming that molecules in a gas attract each other (van der Waals, 1873). Therefore, this so-called van der Waals force is a consequence of the general attraction between molecules on the surface. In particular, the force acts between two macroscopic bodies such as particle-particle and particle-wall (London, 1930; Lifshitz, 1956).

In Table I.2, the equations representing the van der Waals' force are listed (Masuda *et al.*, 2006).

The constant A in these equations is called the *Hamaker constant* and takes into account the properties of the material of the particles and of any third material between the two bodies. However, only van der Waals attraction in air is considered in this work.

The values of the Hamaker constant in air are generally about 10^{-20} J, (Visser, 1972). The separation distance z in the equations in Table I.2 is usually taken as $z_0 = 0.4$ nm (= 4 Å) in air (Krupp, 1967).

At the contacting surfaces, it is very difficult that the surface of particle is perfectly smooth. It seems justifiable to consider a curvature radius taking

into account asperities and the shape not perfectly spherical of particles. In the case of rough surface, asperities limit the approach of two particles and the effective separation distance is larger, thereby limiting the van der Waals attraction. For these reasons, the nominal particle diameter often overestimates the characteristic diameter of the contact area.

According to these hypotheses, eq. (I.5) becomes (Schubert, 1982):

$$F_{\text{vdw}} \approx \frac{A\delta}{12z_0^2} \quad (\text{I.7})$$

where δ is the values of a mean curvature radius at the contacting surface.

When particles are subjected to compression or consolidation, equilibrium holds at contact between forces due to the external stress, the attraction force due to the van der Waals interaction and the elastic or plastic resistance force of the material. By simple modification of the classical Hamaker theory, Dahneke (1972) was able to compute the increase of the van der Waals' force with increasing flattening of the contact point. Dahneke's result for the van der Waals' force acting between two particles is:

$$F_{\text{vdw}} = \frac{A\delta}{12z_0^2} \left(1 + \frac{2h}{z_0} \right) \quad (\text{I.8})$$

where h denotes the sum of flattenings of both particles.

With a monodisperse distribution of perfectly smooth spherical particles of an absolutely rigid materials, δ corresponds to the diameter of the particles and $h = 0$. With these hypotheses, eq. (I.8) becomes equivalent to eq. (I.5).

1.3.2 Electrostatic forces

Particles with different electric charge attract each other.

Between two charged particles, coulombic force F_{ec} acts and the force is approximately calculated by the following equation:

$$F_{\text{ec}} = -\frac{1}{4\pi\zeta_r\zeta_0} \frac{q_1q_2}{z^2} \quad (\text{I.9})$$

where q_1 and q_2 are the total charges of the particles, z is the distance between centers of the particles, ζ_0 and ζ_r are the dielectric constant of free space and the relative dielectric constant, respectively.

Electrostatic force can be attractive or repulsive, in spite of the charge of particles, differently from van der Waals' force, that is only attractive.

Electrostatic interaction can occur also between a charged particle and an uncharged surface because of to its own image charge. When a charged particle approaches a surface, it induces an "image charge" in the surface. The image force F_{ei} that acts is (Masuda *et al.*, 2006):

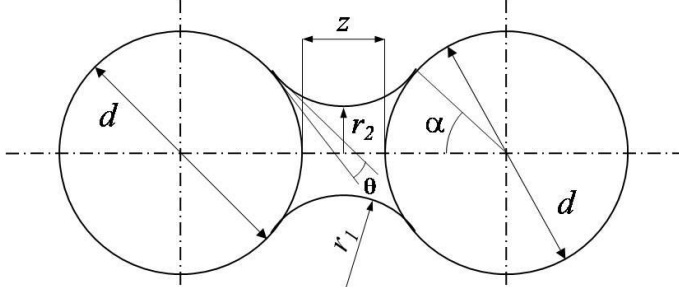


Figure I.1 Schematic representation of a liquid bridge between particles.

$$F_{ei} = \frac{1}{4\pi\xi_r\xi_0} \frac{\xi - \xi_r\xi_0}{\xi + \xi_r\xi_0} \frac{q^2}{(2z)^2} \quad (\text{I.10})$$

where q is the particle charge and ζ is the dielectric constant of the wall material.

1.3.3 Capillary forces

When a liquid phase forms in the bulk solid of particles, for example when the relative humidity of atmosphere is relatively high (>65%) or a chemical component melts at high temperature, a liquid bridge is formed at the contact point of two particles, as shown in Figure I.1, resulting in a component additional to the van der Waals attraction.

Let's consider two identical spheres of diameter d , joined by a liquid bridge of half-angle α and separated by distance z , as shown in Figure I.1. Following the Fisher's theory (1926), the total force exerted through the bridge can be considered as the contribution of:

- the surface tension σ_s , acting on the solid-liquid interface:

$$F_1 = 2\pi r_2 \sigma_s \quad (\text{I.11})$$

- the capillary pressure, ΔP , arising from the curvature of liquid meniscus at the fluid-liquid interface:

$$F_2 = \pi r_2^2 \Delta P \quad (\text{I.12})$$

The total capillary force will be given by the sum of eqs. (I.11), (I.12):

$$F_{\text{cap}} = 2\pi r_2 \sigma_s + \pi r_2^2 \Delta P \quad (\text{I.13})$$

If the cross section of the liquid bridge is approximated by a circular arc, capillary pressure ΔP is expressed by:

$$F_{\text{cap}} = \sigma_s \left(\frac{1}{r_1} - \frac{1}{r_2} \right) \quad (\text{I.14})$$

If it is assumed that r_1 is very much higher than r_2 , the geometric relations among particle diameter d , r_1 and r_2 give the following simplified equation for contacting sphere of the same size:

$$F_{\text{cap}} \cong \pi\sigma_s d \quad (\text{I.15})$$

For a spherical particle on a plane wall, it becomes

$$F_{\text{cap,wall}} \cong 2\pi\sigma_s d \quad (\text{I.16})$$

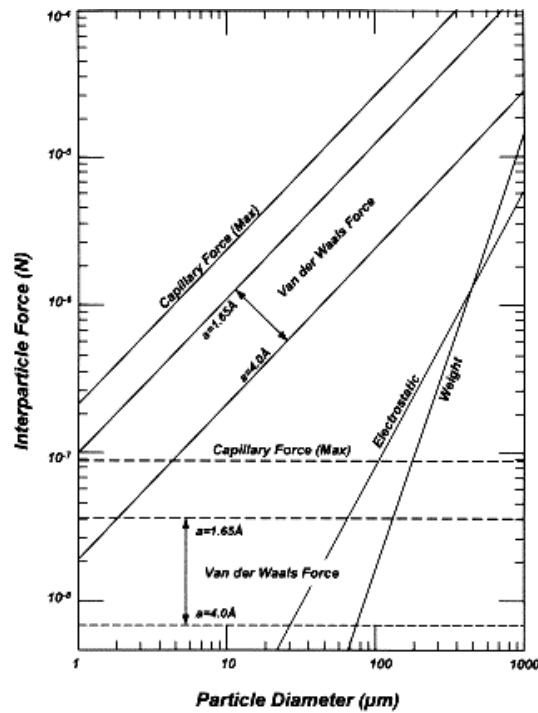


Figure I.2 Comparison of the magnitude of interparticle forces. Dashed lines indicate asperity-to-plane contact. Theoretical interparticle forces for single-point contact between equal spheres in air, with particle weight plotted for comparison (Seville *et al.*, 1998).

- | | |
|---------------|--|
| van der Waals | <ul style="list-style-type: none"> i. $A = 6.5 \times 10^{-20}$ J (quartz) ii. values presented for interparticle separations of 1.65 Å and 4.0 Å iii. dashed lines assume asperity-to-plane contact with asperity radius 0.1 μm |
| capillary | <ul style="list-style-type: none"> i. $\sigma_s = 72.8 \times 10^{-2}$ N m⁻¹ (water) ii. values are maximum, eq. (I.15) iii. dashed lines indicate asperity contact as above |
| electrostatic | <ul style="list-style-type: none"> i. maximum force (opposite sign) ii. $\zeta_r = 1$; $\zeta_0 = 8.9 \times 10^{-12}$ C² N⁻¹ m⁻² iii. charge density = 10 μC m⁻² |
| weight | <ul style="list-style-type: none"> iii. $\rho_p = 3 \times 10^3$ kg m⁻³ |

1.3.4 Comparison of interparticle forces

Comparison of the magnitude of interparticle forces is showed in Figure I.2. The capillary force is the dominating force, as long as the liquid bridge is formed. Without the liquid bridge, the van der Waals force dominates.

It may be more plausible that interparticle forces depend more on the particle surface than on the bulk. Therefore, the van der Waals and capillary forces depend more on the local curvature of the particle (presence of asperities) than the particle radius.

The magnitude of the interparticle forces becomes negligible compared to that of the gravitational force when the particle size exceeds a certain value. The gravitational force can be expressed by the following equation

$$F_g = \frac{\pi d^3}{6} \rho_p g \quad (\text{I.17})$$

where ρ_p is the particle density and g is the acceleration due to gravity.

This result is also plotted in Figure I.2 and suggests, for the set of chosen variables, that spherical particles of diameter of order $100 \mu\text{m}$ should exhibit interparticle van der Waals forces equal to their single particle weight.

1.3.5 Measurements of the interparticle forces at high temperature

It is by understanding interparticle forces that the particle technologists are able to optimize procedures and to design equipments for industrial plants processing granular materials. At these purposes, it is equally

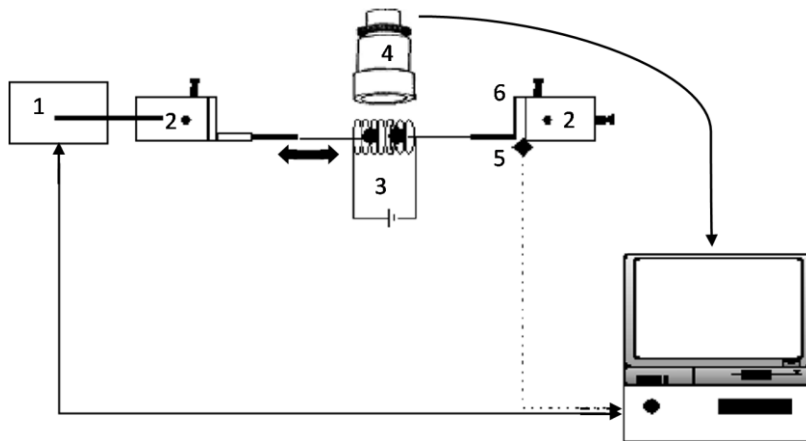


Figure I.3 Schematic representation of the HTMF: (1) DC motor + axial linear actuator; (2) micromanipulators; (3) heating element + thermocouple; (4) objective + digital camera; (5) LVDT displacement sensor; (6) flexure strip assembly (Pagliai *et al.*, 2004).

important measure the forces acting between two particles.

For this purpose, many experimental equipments were developed. They are mainly based on the measurements of the displacement caused by these forces on a cantilever system able to deform for very small forces (10^{-9} N) (Luckman, 1989).

To the contrary, it is so difficult to evaluate these forces at high temperature, mainly because of difficulties related to design a heating system operating at the same time of the measurement device.

Pagliai *et al.* (2004 and 2007) developed a novel technique, called High Temperature Micro-Force Balance (HTMFB), which combines these two aspects and allows a direct observation of the physical phenomena (Figure I.3). Particles, which can be of diameters as low as 10 μm , are attached on the tips of micropipettes, connected to two micromanipulators, under the focus of the microscope lens. This device permits to measure the strength of a liquid bridge formed between particles, either by the addition of a liquid onto the particles or by melting the particle surfaces (i.e. as occurs during sintering). The particles are positioned within the coils of a heating element calibrated with a thermocouple in order to reach temperatures up to 1000°C. Of the two micromanipulators, one is held static whilst the other causes the particles to separate via a linear actuator at high resolution (0.1 μm), driven by a DC motor. A digital camera, plugged into a personal computer (PC) and fitted in the microscope objective, grabs image sequences for each run of experiments for later analysis of, for example, the surface effects. The separation of the particles causes a flexure strip mounted on the static micromanipulator to bend, under loads as low as 10^{-6} N. The linear variable differential transformer (LVDT) displacement sensor provides the position of the strip with a resolution of 20 nm, with the data collected by a data logger in the PC.

For the Hooke's law, the relevant force of the liquid bridge F_{cap} can be calculated by:

$$F_{\text{cap}} = \kappa \cdot \Delta D \quad (\text{I.18})$$

where κ is the spring constant and ΔD the displacement of the bending strip.

I.4 Flow properties of powders

A possible approach for a macroscopic analysis of the rheological behavior of powders consists of measuring the interparticle interactions and integrating them on all the population of particles. However, this approach is much problematic since has to take into account of particle size distribution, shape and surface properties of particles which are difficult to correctly evaluate.

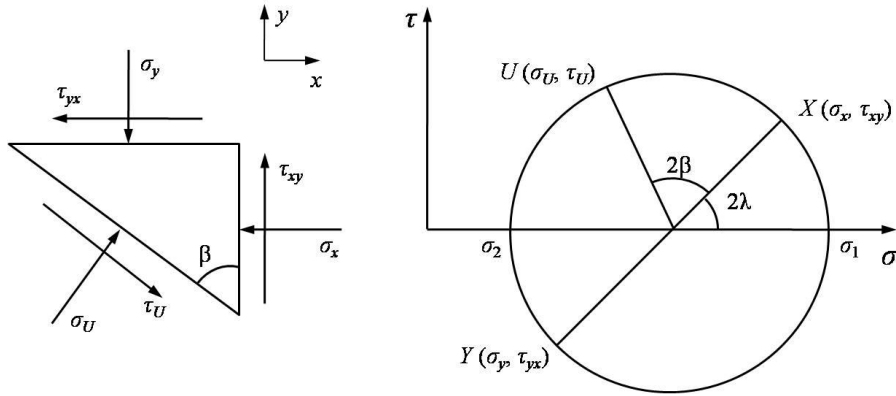


Figure I.4 Mohr analysis (Neddermann, 1992).

Another approach more common in engineering science consists of a direct characterization of the rheology of powders like a bulk solid.

This approach follows the Mohr analysis of a continuum solid. According to this analysis, considering a set of σ , τ axes, the state of stresses in any point of a solid can be represented by a circle, commonly known as Mohr's circle. Every point on the circle, corresponding to a combination of normal stress, σ , (considered as positive when compressive) and shear stress, τ , defines a specific plane of stresses. As shown in Figure I.4, a plane inclined at β anticlockwise from x -plane is given by the end of the radius inclined at 2β anticlockwise from the radius to the point X , as shown by point U . In particular the stresses on the y -plane, for which θ is 90° , are therefore given by the other end of the diameter from the point X . There are two planes of particular interest, namely those on which the shear stress is zero. These are known as the *principal planes* and are indicated in Figure I.4 as σ_1 and σ_2 , called the *major* and *minor principal stresses*. It can be seen that the major principal plane lies at an angle λ clockwise from the x -plane and that the minor principal plane lies at an angle $90 - \lambda$ anticlockwise from the x -plane.

1.4.1 The Mohr-Coulomb failure criterion

In order to analyze the behavior of granular materials when they are subjected to a force, the Coulomb yield criterion is adopted. Following this criterion, a perfect elastic behavior is hypothesized when the force is below a critical value while a perfect plastic behavior is considered when the force exceed this critical value. This value does not depend on the slip plane or the rate of deformation but only on the normal stress applied on the slip plane. In general, it can be written as:

$$\tau = f(\sigma)$$

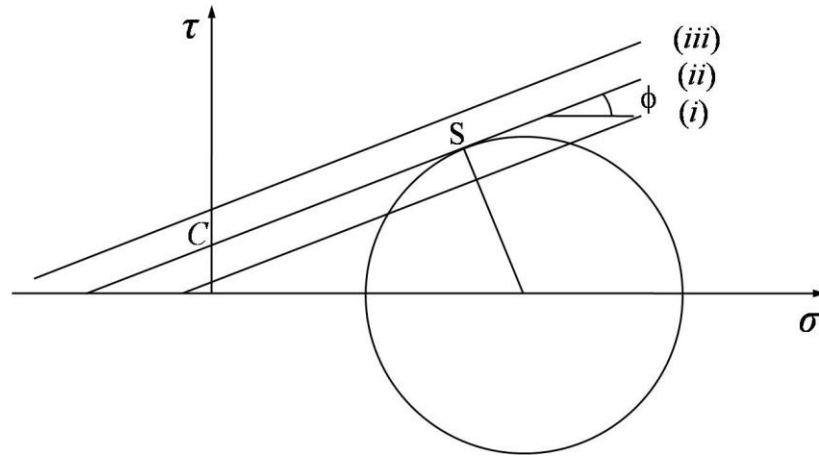


Figure I.5 The internal yield locus and the Mohr-Coulomb criterion:
 (i) $\tau > \mu\sigma + C$; (ii) $\tau = \mu\sigma + C$; (iii) $\tau < \mu\sigma + C$.

This relationship is commonly known as *internal yield locus*.

For many materials, the expression takes linear form:

$$\tau = \mu\sigma + C \quad (\text{I.19})$$

where μ and C are called respectively the *coefficient of friction* and the *cohesion* and depends on the material. The *angle of internal friction* ϕ , that is the slope of the yield locus, is related to the coefficient of internal friction μ by the relationship $\mu = \tan\phi$.

For the Coulomb yield criterion, shown in Figure I.5, on any plane $\tau < \mu\sigma + C$ no failure will occur. If, in the other hand, $\tau = \mu\sigma + C$, a slip plane will be formed. Value of $\tau > \mu\sigma + C$ cannot occur, except perhaps transiently. The Mohr-Coulomb failure criterion derives from the conjunction of the Mohr analysis and the Coulomb yield criterion. For this criterion, in failure condition the Mohr's circle identifying the state of stresses of bulk solid can be only tangent to the yield locus and the tangency point represents the failure plane of the material, like the point S of Figure I.5.

A slip plane along a bounding surface or a wall can occur when a bulk solid is subjected to a force. Similarly to the case of the internal failure, the *wall yield locus* is defined as the upper limit of shear stress on the wall plane. It depends on the type of powder and on the material of the wall and the following linear relationship is commonly adopted:

$$\tau_w = \mu_w\sigma_w + A_w \quad (\text{I.20})$$

where subscripts W indicates stresses in wall region. The wall yield locus is not tangent to the principal Mohr's circle which, on the other hand, represents the state of stresses inside the bulk of the powder. Finally, μ_w is

the coefficient of wall friction and A_w is the adhesion. The angle of wall friction ϕ_w , as the angle of internal friction ϕ , is related to μ_w by $\mu_w = \tan\phi_w$.

1.4.2 Measurements of the failure and flow properties of powders

Different types of equipments and test are able to evaluate the failure properties of granular materials at ambient condition (Schweddes, 2003).

A very intuitive test is the *uniaxial test*. A sample is filled into a cylinder with frictionless walls and is consolidated under a normal stress σ_1 leading to a bulk density ρ_b . After removing the walls, the sample is loaded with an increasing normal stress up to the point of failure. The stress at failure is the *unconfined yield strength* f_c . Greater is the unconfined yield strength, greater is the cohesive behavior and worse is the flowability of the material. The plot of the unconfined yield strength f_c vs. the normal stress σ_1 is commonly known as *flow function*, which is one of the key parameter in the design of hoppers and silos. Jenike (1964) introduced a classification of granular material according to the ratio of σ_1 and f_c called *flow factor* ff_c (Figure I.6):

- $ff_c < 1$: granular materials are known as hardened;
- $1 < ff_c < 2$: granular materials are known as very cohesive;
- $2 < ff_c < 4$: granular materials are known as cohesive;
- $4 < ff_c < 10$: granular materials are known as easy flowing;
- $ff_c > 10$: granular materials are known as free flowing.

However, the main limit of the uniaxial test is that only cohesive powders can be studied since they do not yield after the walls have been removed.

The more common equipments for the evaluation of the failure and flow properties are the *shear cells*. They consist of measuring the force F able to generate a slip plane inside a sample of granular material for a specified applied normal load N . There are translational or rotational shear cells according to the shear plane is generated for translation or rotation of the

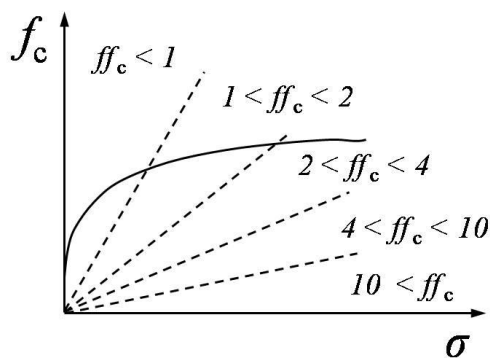


Figure I.6 The flow function and the Jenike classification of granular materials (Jenike, 1964).

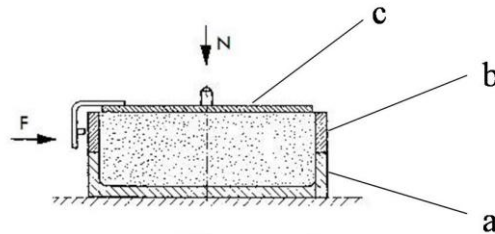


Figure I.7 Jenike shear cell. (a) base; (b) ring; (c) lid (Standard Shear Testing Technique, 1989).

components of the shear cell.

The most important translational shear cell is the *Jenike shear cell*. It consists of a circular base, a ring placed on top of the base and a lid (Figure I.7). A powder sample is filled into the base and the ring.

The test procedure follows two steps. The first step, known as preconsolidation or *preshear*, consists of applying a horizontal shear in the sample by moving forwards the ring at a specified preconsolidation load, σ_c , applied on the lid hold steady. Preshear is applied until steady state conditions are reached and detected by a constant value of measured shear force, τ_c , necessary to hold the lid in steady position. The second step, known as *shear*, consists of applying again a shear within the sample with a normal load applied, σ , on the lid lower than the preconsolidation load.

The maximum of the registered shear force measured on the lid allows calculating the incipient shear stress of the material, τ , as consolidated during the preshear and is a function of the applied normal load. Repetition of these steps with decreasing normal loads during shear steps allows evaluating the internal yield locus.

A schematic of the experimental procedure of the measurement of the internal yield locus is shown in Figure I.8.

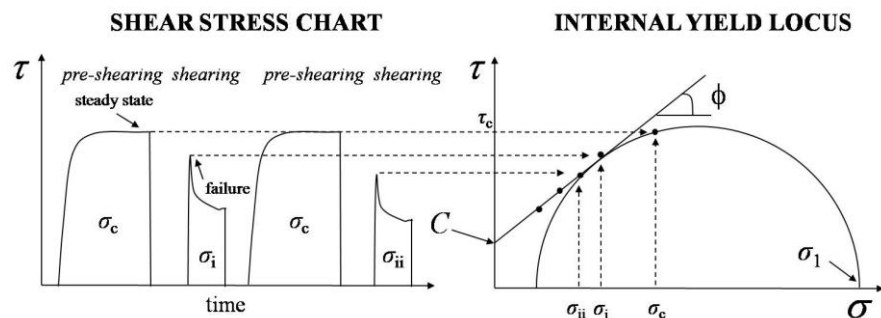


Figure I.8 Measurement of the yield locus with a shear cell: schematic of the experimental procedure.

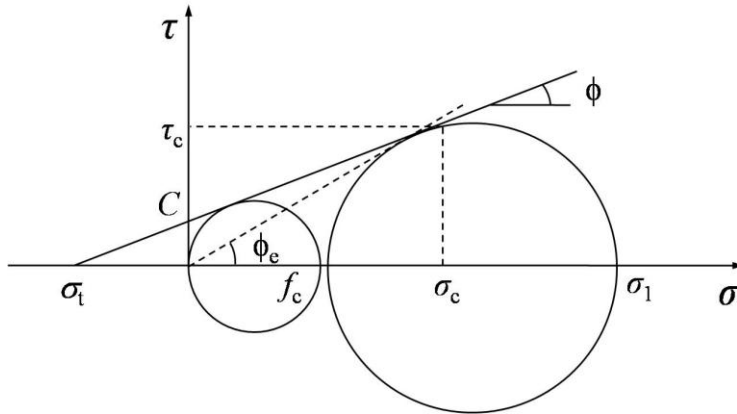


Figure I.9 The internal yield locus and the main flow and failure parameters.

The internal yield locus is the best fitting line with the measured value in a σ, τ diagram. The detailed experimental procedure was developed by the Working Party on the Mechanics of Particulate Solids within the European Federation of Chemical Engineering and described in the “Standard Shear Testing Technique for Particulate Solids using the Jenike Shear Cell” (1989).

The major principal stress σ_1 of the preconsolidation is evaluated by the intersection of the σ -axis and the Mohr’s circle tangent to the yield locus and passing to the point of consolidation (σ_c, τ_c) . Each yield locus is parametric with the consolidation level of the bulk solid, defined by the major principal stress σ_1 . With higher preconsolidation loads, the bulk density ρ_b increases and the yield locus moves upwards.

The *unconfined yield strength* f_c is estimated by the intersection of the σ -axis and the Mohr’s circle tangent to the yield locus and passing to the origin of the axis. Each yield locus gives one pair of values of the unconfined yield strength f_c and the major consolidation stress σ_1 from which is possible to plot the flow function. It can be easily calculated by geometric consideration as:

$$f_c = \frac{2C \cos \phi}{1 - \sin \phi} \quad (\text{I.21})$$

Another key parameter is the *effective angle of internal friction* ϕ_e , the angle between the σ -axis and the tangent to the principal Mohr’s circle. It is a measure of the inner friction at steady state flow and is very important in the design of hoppers and silos.

A less intuitive concept for granular materials is the *tensile strength* σ_t . It represents the resistance force to separate two layers of material by means of a tensile force. It is evaluated by the intersection of the negative σ -axis and

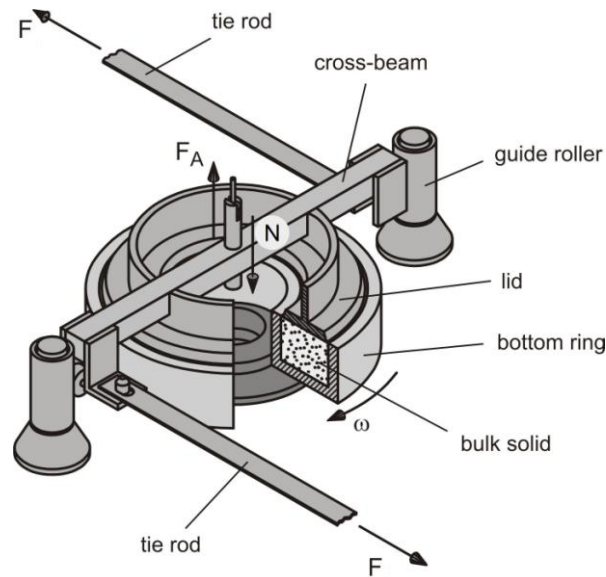


Figure I.10 Schematic of the annular Schulze shear cell (Schulze, 1994).

the yield locus. It is not equal to zero when interparticle attractive interactions are present. It can be simply calculated as:

$$\sigma_t = \frac{C}{\tan \phi} \quad (\text{I.22})$$

All these parameters are represented in Figure I.9.

Translational shear cells, as the Jenike shear cell, show the following disadvantages: no measurements at low consolidation levels are possible, the maximum strain is small and much time is needed for a test. The rotational annular shear cells, as the Schulze Ring Shear Tester schematically represented in Figure I.10, provide comparable results with Jenike shear cell, do not have limits of strain and are able to perform measurements at small normal stresses (< 1 kPa) by means of a balancing system of the lid of the cell, indicated by the force F_A . The experimental procedure follows the same principle of the Jenike shear cell, with repeated steps of *preshear* and *shear*. In this case, the measured variable is the torque needed to the rotation of the lid from which the shear stress τ is derived.

In the other hand, the evaluation of the wall yield locus does not required two steps. Shear stresses are measured formerly for decreasing normal loads and subsequently increasing normal loads until to the initial maximum value without *preshear*. In this case, the measured shear is not the peak of the curve, like for the internal yield locus, but the constant value representing steady state conditions. For this reason, the wall yield locus is not function of the consolidation level and of the packing of the powder.

1.4.2.1 Measurements of flow properties at high temperature – A literature survey

Few works about the direct evaluation of the flow properties of powders at high temperature are in literature. In the most of case, the increase of the cohesive behaviour of powders as the temperature increases was observed. In some papers, measurements at high temperature were performed through shear cells.

MgSO₄ and CaSO₄ powders was analyzed by Smith *et al.* (1997) with a Jenike shear cell at ambient condition after that the sample was preheated for 1 h at 750°C. Experimental results for consolidation load of 40-200 kPa show an increase of the flow function as the temperature increases for all the analyzed powders. SEM observations and X-ray diffraction measurements showed agglomerates formed during the preheating of the sample. However, with this technique it is not possible to control the temperature of the powders during the test.

This disadvantage was worked out performing measurements inside heated chambers where the temperature is opportunely controlled. (Pilz e Loeffler, 1995; Kanaoka *et al.* 2001).

Yield loci at 20°C, 400°C and 850°C of a fine quartz powder ($d_{0.5} = 3.32 \mu\text{m}$) for a consolidation load of 3 kPa was evaluated with a Jenike shear cell (Pilz e Loeffler, 1995). Also in this case, an increase of the cohesive behaviour of granular material as the temperature increases was observed. Furthermore, the effect of different experimental procedures was studied. In particular, yield loci were measured when preshear was performed before and after the heating of the sample. Greater values of shear stresses were measured in the first case. Unfortunately, measurements at lower consolidation levels are not possible with this apparatus.

Kanaoka *et al.* (2001) performed measurements at high temperature (up to 950°C) and at low consolidation level (< 1 kPa) on fly ash particles ($d_{0.5} = 2.35 \mu\text{m}$) by means of a Powder Bed Tester placed in a heated chamber. It measures the stress able to generate the shear of a moving plate on a preconsolidated powder sample packed in a fixed plate. The Powder Bed Tester has the advantages that measurements are possible at low consolidation stresses. On the other hand, measurements performed by this apparatus evaluate the adhesion of the powder respect to a specified wall sample but does not allow estimating the internal flow properties. The measured properties are underestimated respect to those evaluated with the standard Jenike shear cell (Schwedde, 2003). However, in this study an increase of the adhesive force was measured as the temperature increase. Furthermore, sintering and agglomeration occurred for temperature greater than 800°C as demonstrated by thermogravimetric and SEM analysis.

Besides shear test, different techniques are available to evaluate the flow properties of granular materials at high temperature.

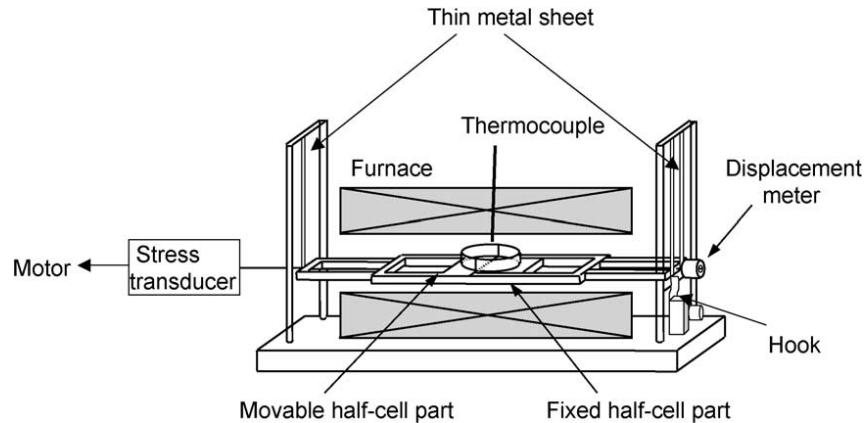


Figure I.11 Schematic of the split-type tensile strength system on high temperature conditions (Kamiya *et al.*, 2002).

A split cell is a circular cell equally divided into a stationary part and a movable part. It measures the tensile strength able to separate in horizontal direction the movable part from the fixed part of the cell filled of powder. Kamiya *et al.* (2002) placed this apparatus in a heated chamber, as shown in Figure I.11, and perform measurements on ashes and silica powder up to 900°C. An increment of the tensile strength with the increasing temperature was observed up to 800°C. Above 800°C, experimental results for the ashes showed a faster increase of the tensile strength with the temperature because of the formation of liquid bridges and sintering phenomena. Below 800°C, the increase of the cohesive behaviour was explained with alteration of the surface properties of particles, according to IR spectroscopy analysis on the experimental materials.

Similar to Kamiya *et al.* (2002), Hurley *et al.* (2006) carried out measurements by means of a split cell with a porous metallic bottom through which air was pulled. The aim of this work was to study the effect of temperature on the adhesive and cohesive properties of dusts of combustion in order to evaluate its role on the efficiency of candle filters. Different results came out. For one type of dust, a decrease of the tensile strength with the temperature increase was observed up to 400°C. However, when alteration of the chemical composition, new crystalline structure or sintering occur at high temperature, a different behaviour was observed and chemical aspects have to be considered for a correct interpretation of the phenomena occurring at high temperature.

Measurements of torque necessary to the rotation of an impeller into a bed of different samples of cohesive powders were performed by Zimmerlin *et al.* (2008) up to 700°C. The increase of the torque as the temperature increases was observed. Also in this case, it was explained as an increase of the cohesive behaviour of powders with increasing temperature.

Ripp and Ripperger (2010) designed an annular shear cell according to Schulze operating from 80°C to 220°C. For this purpose, an electric heater was placed on the upper part of the lid while the vertical walls and the bottom of the cell were provided with a double casing through which a heating or a cooling medium can flow. An impressive experimental campaign was conducted and wall friction and internal friction at different temperature were evaluated for different kinds of powders. From this work, a not univocal effect of temperature was determined for all the types of powders.

I.5 Fluidization

Fluidization is one of the most common unit operation involving granular materials. As its name implies, it is a process that transforms a bed of solid particles into a fluid-like state through an upwards flow of gas or liquid. The fluid-like properties of fluidized beds make them attractive for industrial processes where a solid (often the catalyst for a reaction) and a gas are to be put in contact. Moreover, the rapid mixing and circulation of solids allows for a uniform temperature in the system. Therefore, high temperature operations in fluidized beds can be controlled simply and reliably.

Let us consider a bed of fine solid particles is placed in a vessel and fitted with a porous baseplate and a fluid (gas or liquid) is pumped upwards through the base. Now, if the fluid velocity is gradually increased, the drag force acting on the particle rises and the pressure drop through the bed will also increase until the point at which the drag force is equal to the gravitational force holding the particles within the container. At this point, the bed will expand upwards as the particles become suspended in the flowing stream. In this condition, the particles are then said to be *fluidized* and the bed takes the appearance and responds in the same way of a liquid.

The superficial velocity at which this phenomenon occurs is called minimum fluidization velocity u_{mf} and depends on the physical properties of the fluid and the solid particles.

Its value can be found by measuring the pressure drop across the bed as a function of fluid velocity, as shown in Figure I.12. Furthermore, at the minimum fluidization condition, the force exerted by the upwards flowing fluid is equal to the gravitational force acting on the particles, then:

$$\frac{\Delta P}{H_{mf}} = [\rho_p (1 - \varepsilon_{mf}) + \rho_f \varepsilon_{mf}] g \quad (I.23)$$

where ΔP is the pressure drop across the bed, H_{mf} and ε_{mf} are the height and the void fraction of the bed at minimum fluidization, respectively.

However, many empirical and semi-empirical equations are available to evaluate u_{mf} starting from the physical properties of the solid particles and the fluid. They are mainly based on the principle of extending the pressure

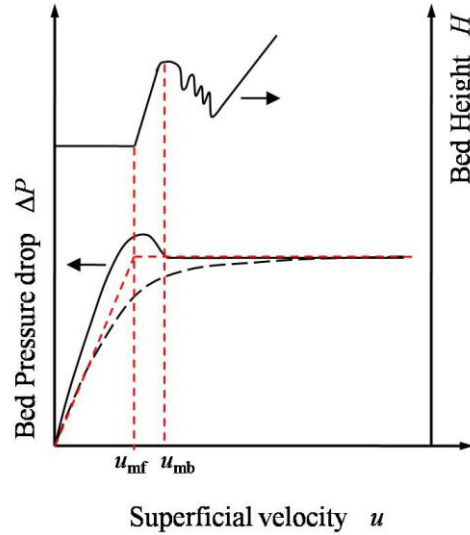


Figure I.12 The pressure drop across the bed and the bed height as a function of the superficial velocity for a Geldart group A powder.

drop relations for packed beds to the minimum fluidization condition, where the superficial velocity is u_{mf} .

One of the problems to predict u_{mf} is the minimum fluidization voidage fraction ϵ_{mf} is unknown a priori. Wen and Yu (1966) reported two valid empirical relationships for a wide range of particles:

$$\frac{1 - \epsilon_{mf}}{\Psi^2 \epsilon_{mf}^3} \sim 11 \quad (\text{I.24})$$

$$\frac{1 - \epsilon_{mf}}{\Psi \epsilon_{mf}^3} \sim 14 \quad (\text{I.25})$$

Combining these equations with the Ergun equation at minimum fluidization:

$$\frac{\Delta P}{H_{mf}} = \frac{150(1 - \epsilon_{mf})^2}{\epsilon_{mf}^3} \frac{\eta u_{mf}}{(\Psi d_{SV})^2} + \frac{1.75(1 - \epsilon_{mf})}{\epsilon_{mf}^3} \frac{\rho_f u_{mf}^2}{\Psi d_{SV}} \quad (\text{I.26})$$

where η is the viscosity of the fluidizing gas (or fluid), they obtained the generalized correlation:

$$Re_{mf} = (33.7^2 + 0.0408 \times Ar)^{1/2} - 33.7 \quad (\text{I.27})$$

where:

$$Re_{mf} = \frac{u_{mf} d_{SV} \rho_f}{\eta} \quad (\text{Reynolds number}) \quad (\text{I.28})$$

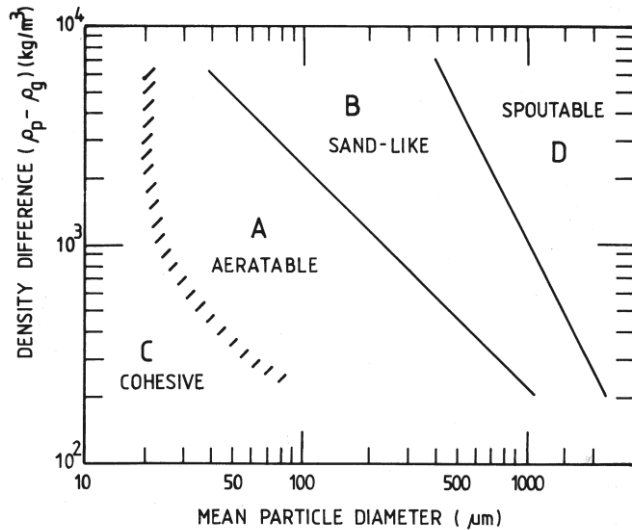


Figure I.13 Geldart's classification of powders.

$$Ar = \frac{d_{sv}^3 \rho_f (\rho_p - \rho_f) g}{\mu^2} \quad (\text{Archimedes number}) \quad (\text{I.29})$$

from which u_{mf} can be estimated knowing only the physical properties of fluid and solids.

If the fluid is a gas, at superficial velocity above u_{mf} , it is observed experimentally gas bubbles form within the bed for many powders. The value of superficial velocity at which bubbles appear is called minimum bubbling velocity u_{mb} and, such as for u_{mf} , also depends on the physical properties of the particles. Above this velocity, the bed is essentially divided in a dense or emulsion phase, where gas goes through the particles rather like in a packed bed, and a bubble phase, where much of the gas is out of contact with solids. If the fluid is a liquid, bubbles form are rarely observed.

A convenient classification of powders has been suggested by Geldart (1973) in according to the experimentally observed behaviors at fluidization conditions. He arranged granular materials into four groups (Figure I.13):

- group A: powders characterized by a relatively small particle size ($d = 30 - 150 \mu\text{m}$) and a low particle density ($< 1500 \text{ kg m}^{-3}$). They show a good expansion of the emulsion phase as the fluidizing gas velocity increases and form bubbles for a minimum bubbling velocity u_{mb} , always greater than u_{mf} (as shown in Figure I.12).
- group B: powders which begin to bubble at gas velocity just in excess to u_{mf} and characterized by $d = 150 - 500 \mu\text{m}$ and densities in the range $1500 - 4000 \text{ kg m}^{-3}$. The dense phase voidage of these

powders remain more or less constant to the minimum fluidization value as the fluid velocity increases.

- group C: cohesive powders of very small size ($d < 30 \mu\text{m}$) shaped far from spherical. They are difficult to fluidize.
- group D: very large size and very dense powders. Normally, they are fluidizable but no bubble form. This is probably due to the dense phase gas velocity higher than the velocity of bubbles formed.

Liu *et al.* (1996) carried out fluidization experiments for solid particles belonging to Geldart group A, B and D with liquids of changing viscosity and with CO_2 under ambient to supercritical conditions. Results showed fluidization quality changes progressively from aggregative, normally associated with gas fluidized systems in which a portion of the rising fluid pass through the bed in the form of bubbles as soon as fluid velocity exceed the minimum fluidization velocity, to particulate, usually referring to liquid fluidized bed which expands uniformly and homogenously from minimum fluidization to dilute-phase transport. They defined a transitional fluidization, characterized by the transition homogenous to heterogeneous fluidization as the fluid velocity rises, which generally includes:

- solid particles belonging to Geldart group A fluidized in gases at ambient condition;
- group B fluidized in gases with elevated pressure;
- group D, fluidized in supercritical gas or liquids relatively low density and viscosity.

These patterns form a continuous spectrum consisting of gradual and progressive changes as particle size, particle and fluid densities and fluid viscosity vary.

Wang *et al.* (1998) conducted experiments on the fluidization of many types of Geldart group C particles, showing that the fluidizing process of fine particles usually involves plugging, channeling, disrupting and agglomerating. Furthermore, they showed agglomerates vary in size and density with the superficial velocity and the cohesiveness of the material and behave as the same as single particles.

The Geldart classification considers only hydrodynamic parameters like the diameter and the density of particles and the density of the fluid, and does not take into account the interactions between particles. Both the behaviour of a powder in a fluidized bed and the initial point of fluidization are governed by the interparticle forces as long as its magnitude is of the order of, or larger than, the gravitational and the fluid-dynamic forces, also acting on the particles under these circumstances.

Molerus (1982) derived equivalent limiting conditions of the Geldart classification by taking into account the interparticle forces and demonstrated that:

- separation of Geldart group A from Geldart group C is due to the dominance of the cohesion forces in the type C compared to the hydrodynamic and gravitational forces;
- separation of Geldart group B from Geldart group A follows from the negligible magnitude of the interparticle forces in the fluidization condition in type B compared to the hydrodynamic and gravitational forces.

On the transition between homogenous and bubbling regime, many works try to define what is the controlling factor between the hydrodynamic and interparticle forces. However, the question is still now controversial.

Massimilla and Donsì (1972 and 1973) carried out bed expansion experiments in a semicircular column with a transparent flat wall and discovered through microscopic observations cavities and micro channels into the bed of the same order as the particle size. This mode of bed expansion was explained by considering the role of interparticle forces which act to stabilize cavities and microchannels, playing an important role in the fluidization behaviour of fine powders.

On the effect of the interparticle forces on the homogenous fluidization, Mutsers and Rietema (1977) carried out experiments on a tilting fluidized bed. In these experiments, it is appeared possible tilting the bed until a certain angle without the powder sliding. These clearly demonstrated a powder structure with a certain mechanical strength exists in the expanded state of homogenous fluidization because of the no-negligible presence of the interparticle interactions.

1.5.1 The effect of temperature on the fluidization behaviour

Research on the influence of temperature on fluidization has been gaining interest, but findings are still controversial. A satisfactory understanding of the phenomena which are responsible for modifications in the structure of fluidized beds, and therefore responsible for changes in the flow behaviour, from ambient to high temperature, has not yet been adequately achieved.

Xie and Geldart (1995) performed measurements at different temperatures ($\leq 500^\circ\text{C}$) of the incipient fluidization and bubbling velocities and the voidage at the minimum bubbling point for samples of various size fractions of FCC powders and found that these parameters decrease as the temperature increase. Furthermore, they compared these values with values estimated from some existing correlations, normally based entirely on hydrodynamics considerations. Although these equations predict well for the coarser fraction at ambient temperature, they become increasingly inaccurate as particle size is decreased and this is believed to be the result of ignoring the interparticle forces.

Subramani *et al.* (2007) conducted experiments of fluidization up to 700°C on different Geldart B powders and developed two new correlations

improving the prediction of the voidage and the velocity at minimum fluidization at high temperature.

Yang (2007) did not take into account interparticle forces and re-interpreted the Geldart's classification considering pressure and temperature different from ambient condition. In particular, only the effect on the viscosity and the density of the fluid with these two variables was considered. Increasing the operating pressure will increase the fluid density, while not changing viscosity it will increase the tendency to Group A behaviour. Increasing the temperature, however, will have different results depending on the decrease of the fluid density and the increase of viscosity.

With a different approach, Formisani *et al.* (1998, 2002) found out the voidage in the fixed state and at incipient fluidization, the dense phase voidage of a bubbling fluidized bed increasing practically linear with temperature. They carried out bed expansion and collapse test up to 700°C on different samples of FCC powders, silica sand and corundum and demonstrated that, taking correctly into account the thermal variation of the incipient fluidization voidage, some classical equations of fluidization theory, as Carman-Kozeny's and Ergun's, based only on hydrodynamic forces, take again their predictive ability.

Lettieri *et al.* (2000 and 2001) confirmed the Formisani's experimental results in which the incipient and dense phase voidage of a bubbling fluidized bed increase with temperature. Additionally, they demonstrated the increase of temperature leads significant modifications of the fluidization dynamics because of the increase of interparticle interaction. In fact, SEM observations of Geldart group A samples after bed expansion and collapse experiments at high temperature (up to 700°C) revealed the formation of stable aggregates, as if the effect of the temperature increase caused a transition from a Group A to a Group C type of behaviour.

Bruni *et al.* (2006) performed an extensive experimental campaign aimed at studying the influence on fluidization of changing the size distribution of the fine sub-cuts (particles below 45 μm) of Group A powders (alumina powders) up to 400°C. Fluidization experiments showed that fines addition did not affect the quality of fluidization while significant changes were observed in bed collapse test. In particular, a decrease of the dense phase collapse rate was observed with the increasing temperature. It was related to the changes of the packing of the structure, more compacted as the dimension of fines decrease. Furthermore, the validity of the Richardson-Zaki correlation was verified by changing the parameters of the equation with the fines percentage and the temperature. Results were explained with the effect of the increase of the relative weight of the interparticle forces on the mass forces due to the decreasing mean dimension of particles.

Although the effect of temperature on the fluidization is not univocally explained, the common interpretation is that interparticle forces have to be

necessarily taken into account for understanding the flow behaviour of powders in fluidization and changing the temperature.

I.6 The particle-particle approach

The state of stress in a point of a continuum is completely determined by the symmetrical stress tensor, which can be graphically represented by Mohr's circle. As described in previous paragraphs, the Mohr's circle is also used for the representation of stress state on powder sample as well as in theoretical models based on continuum mechanics. This continuum approach allows simplifying particularly the analysis of the failure and flow properties of granular materials and to apply directly experimental findings and measurements to standard procedures for the design of industrial equipments. However, the main disadvantage of this method consists of the difficulty to extend experimental evidences to engineering applications providing different packing conditions of powders.

On the other hand, for science and technology it is useful to combine the continuum approach and a particle-particle approach in order to provide a better understanding of the mechanical properties of bulk solids. Furthermore, by means of a microscopic model able to estimate quantitatively the interparticle interactions it might be possible to extend the experimental findings derived from shear testers to different compaction conditions.

According to the particle-particle approach of Rumpf (1974) and Molerus (1985), in order to relate bulk solids properties to binary interparticle interactions a randomly packed bed consisting of monodisperse spheres can be assumed. In particular, in this approach the following assumptions were considered:

1. particles are assumed to be spherical;
2. the contact areas between particles are small enough in comparison with the particle surfaces. Consequently, contact areas can be assumed as contact points;
3. the contact points are distributed over the sphere surface with equal probability;
4. the packing structure is isotropic. In particular, area porosity and volume porosity are equal for arbitrarily orientated planes in the packing.
5. the transmission of an isostatic state of compressive stress with three equal principal stresses was further assumed.

From these hypotheses, Rumpf and Molerus derived the following equation relating the isostatic stress with a mean isotropic contact force:

$$\sigma = \frac{F_c}{d^2} \frac{k(\varepsilon) (1 - \varepsilon)}{\pi} \quad (\text{I.30})$$

where σ is the normal isostatic stress, F_c is the mean isotropic contact force and k is the coordination number, the number of contacts per particles, dependent from the packing and, then, the voidage of the powder bed. The exact analysis of Molerus (1993) was reported in Appendix A.

According to Smith (1929), for porosities usually founds in bulk solids:

$$k\varepsilon \approx 3.1 \approx \pi \quad (\text{I.31})$$

It follows thus from previous equation that, in any point of the bulk solid:

$$\sigma = \frac{F_c}{d^2} \frac{(1-\varepsilon)}{\varepsilon} \quad (\text{I.32})$$

1.6.1 The dependence of the contact forces on previous consolidation

Eq. (I.8) of paragraph I.3.1 has already introduced the physical phenomenon of flattening occurring at the contact point of particles when they are submitted to compression or consolidation.

This is the case of *preshear* during tests performed with shear cell, when the sample of powder is initially compacted at a specified consolidation level, defined by the major principal stress σ_1 , by an applied external normal load.

Considering environmental conditions where liquid bridge and electrostatic force do not occur and where van der Waals' forces play a dominant role, an equilibrium holds between the normal force, F_N , due to the external consolidation force, the attraction force due to the van der Waals interaction, F_{vdw} , and the resistance force of the material, F_W :

$$F_N + F_{vdw} = F_W \quad (\text{I.33})$$

where the external compression force F_N , according to (I.31), is equal to:

$$F_N = \frac{\sigma_1 \varepsilon d^2}{(1-\varepsilon)} \quad (\text{I.34})$$

In particular, the material can exert two kinds of resistance: elastic or plastic.

With purely elastic behaviour, the repulsive force may be considered as elastic resistance force between the contacting particles. If only elastic resistance exists, powders do not show a cohesive behaviour increasing with the consolidation. In fact, if the system is unloaded, the pure elastic repulsion brings the system back to the initial state before the application of the consolidation load and no memory is kept of the consolidation on the single contact point. It means that the magnitude of cohesion value do not depend on previous consolidation. In this case, when the system is freed, like when a tensile stress is applied, the contact force is defined by the classical equation of the van der Waals' force of eq. (I.7).

On the other hand, when the plastic irreversible deformation occurs at contact point of particles during consolidation, the extent of particle flattening at the contact point has to be taken into account for the correct

evaluation of the adhesion force. In fact, when the external load, F_N , is removed, the generated flattening remains, affecting the magnitude of the van der Waals' interaction also when the consolidation load is removed, as showed in eq. (I.8).

It is worth to notice the flattening of the contact point is a function of the consolidation load which, therefore, affects also the magnitude of the interparticle force. For small plastic deformation, the resistance force is (Molerus, 1993):

$$F_w = F_{pl} = p_f \pi \delta h \quad (I.35)$$

Let us consider the force balance eq. (I.35), including eq. (I.8) for the van der Waals' force and eq. (I.35) for the plastic resistance of the material. The force balance becomes:

$$F_N + \frac{A\delta}{12z_0^2} \left(1 + \frac{2h}{z_0} \right) = p_f \pi \delta h \quad (I.36)$$

From eq. (I.36) the analytical solution of the dimension of flattenings, h , at the consolidation contact can be easily computed. Inserting it in eq. (I.8), it is possible to obtain the adhesion force due to van der Waals interaction at a flattened contact as:

$$F_{vdw} = \frac{A\delta}{12z_0^2} \frac{1 + (2F_N / \pi p_f \delta z_0)}{1 - (A / 6\pi p_f z_0^3)} \quad (I.37)$$

The main problem of this approach, both for elastic or plastic behaviour, is related to the difficulty to know with greater accuracy the properties of materials appearing in eqs. (I.8) and (I.37), such as the Hamaker constant A , the compressive strength σ_f and the mean curvature radius δ .

In this work, the condition of a static bulk solid submitted to a previous consolidation, where the only contact forces are van der Waals' forces, was assumed corresponding to the theoretical definition of *tensile strength* σ_t , introduced in par. I.4.2. With this hypothesis, according to eq. (I.32):

$$\sigma_t = \frac{F_{vdw}}{d^2} \frac{(1 - \varepsilon)}{\varepsilon} \quad (I.38)$$

However, this will be focused in more detail in chapter V.

Chapter II

The aim of the work

This work is a part of a much broader research of the Powder Technology group of the Department of Industrial Engineering of University of Salerno aimed at investigating the flow behaviour of powders under realistic process conditions.

Changes of cohesive flow properties of powders at high temperature are observed in many industrial process units, such as fluidized bed reactors, granulators and dryers.

Many authors investigated the behaviour of powders at high temperature through fluidization experiments (Formisani *et al.*, 1998; Lettieri *et al.*, 2000 and 2001), direct measurements (Pagliai *et al.*, 2004 and 2007) and evaluation on the bulk solid (Kanaoka *et al.*, 2001; Kamiya *et al.*, 2002), with different interpretation on the role of temperature on the flow behaviour of powder. Although from the literature the increase of the cohesive behaviour appears clear when liquid bridges occur between particles, the effect of temperature on van der Waals' kind of forces is still controversial, in particular at low consolidation levels of powder, as in fluidization, where the relative weight of interparticle forces is greater because of the decrease of mass forces.

Furthermore, conventional testers and procedures are not suitable for measuring the powder flow properties at high temperature.

The first part of this PhD course was aimed to the development of an experimental apparatus able to study the behaviour of powders at high temperature. Shear cells are the more common testers to evaluate the flow behaviour of powders. In this work, an annular Schulze shear cell HT-ASC, originally designed at University of Salerno, was developed and set-up in order to perform measurement up to 500°C. In this novel way, it was possible to evaluate the effect of temperature on the powder flow properties by the direct measurements of yield loci on different materials.

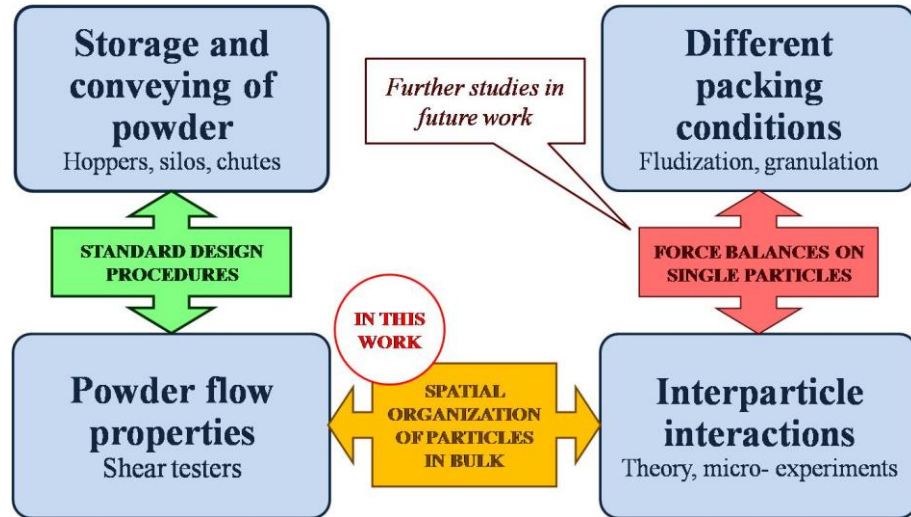


Figure II.1 A concept map represented the logical steps correlating a continuum to a particle-particle approach.

The aim of the second part of this PhD course was to give an interpretation of the physical phenomena occurring at microscale. For this purpose, the development of a theoretical framework was needed, considering simplifying hypotheses, according to the particle-particle approach developed by Rumpf (1974) and Molerus (1985) and describing the correct spatial organization of particles in bulk. In fact, this approach allows correlating the measured powder flow properties to the interparticle interactions in order to give qualitative and quantitative explanations to the experimental evidences at macroscale level.

This particle-particle approach is not commonly adopted in engineering science because of the complexity to directly evaluate interparticle forces and parameters like the Hamaker constant and the mean curvature radius at contact point which implies also difficult to predict interactions between particles. Therefore, the analysis of the powders as bulk solid is preferred and standard procedures utilizing powder flow properties evaluated by shear cells are commonly adopted for the design of equipments for storage and conveying of powder, like silos, hoppers and chutes, where the powder is in compacted conditions.

The aim of the work is also associated to the possibility to extend experimental measurements performed in consolidated conditions by shear cell to other compaction conditions, especially lower such as in fluidization. The quantitative evaluation of interparticle interactions from measurements performed on a bulk solid might be the key step in this way of the research. In fact, from the knowledge of the magnitude of the interparticle interactions

appears possible to predict the behaviour of powder considering different packing conditions, at room and high temperature, by the development of proper mathematical models considering force balances on single particles considering the appropriate hypotheses for the specific applications.

Therefore, the development of a theoretical framework correlating powder flow properties to interparticle interactions, as this work pursues, can be seen as a preliminary step associated to this aim.

As observed in following chapters, results of this study, at room temperature such as at high temperature, are encouraging and suggest further studies in future work.

Chapter III

Experimental

III.1 High Temperature Annular Shear Cell (HT-ASC)

Shear cells are commonly used to evaluate the failure and flow properties of granular materials at ambient condition. Although the large use of powders at high temperature in industrial equipments and plants, conventional testers and procedures are not still suited for testing powder flow properties at high temperature.

A Schulze shear cell was modified at University of Salerno in order to perform measurements of the powder flow properties at high temperature. Figure III.1 shows a schematic of the new High Temperature Annular Shear Cell. It consists of a bottom annular trough containing the powder sample and an annular lid placed on the top of the sample like an annular Schulze shear cell. The lid is fixed at a crossbeam connected by two tie-rods to two

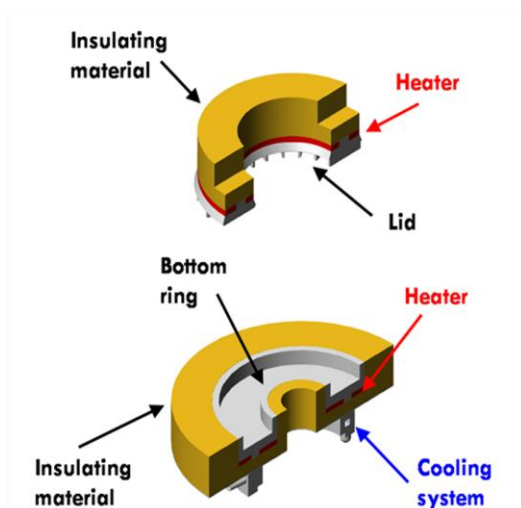


Figure III.1 Schematic of the High Temperature Annular Shear Cell.

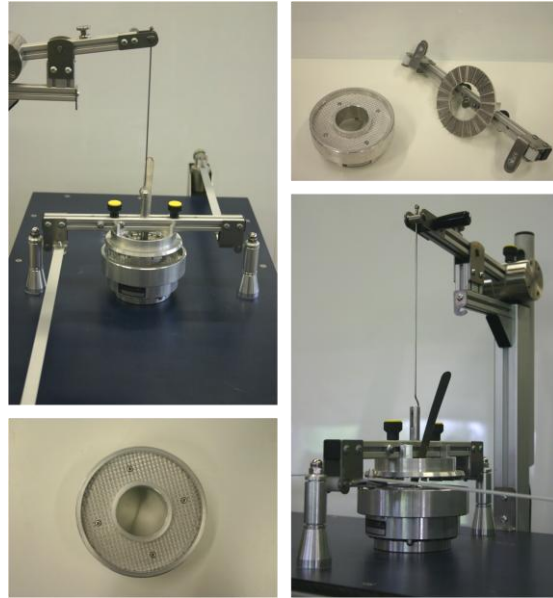


Figure III.2 *The annular Schulze Shear Cell SV10.*

load beams. These allow measuring the shear force acting on the shear plane developed inside the powder sample by the rotation of the bottom ring relative to the lid for a specified normal load, exerted by weight pieces placed on a hanger connected to the crossbeam.

To heat the cell and the powder sample contained in it, electric heaters were introduced below the cell bottom and on the lid. In order to minimize the temperature gradient within the sample and for safe operation of the cell, a covering insulating material was placed around the trough of the cell and above the lid.

A cooling system was designed to cool the cell base where it is in contact

Table III.1 *Data of the High Temperature Annular Shear Cell*

<i>Bottom Ring:</i>	
inner diameter	60 mm
outer diameter	120 mm
nominal height	10 mm
internal volume	95.08 mm
<i>Lid:</i>	
inner diameter	62 mm
outer diameter	118 mm
<i>Power supplier:</i>	
lower heater	600W
upper heater	260W

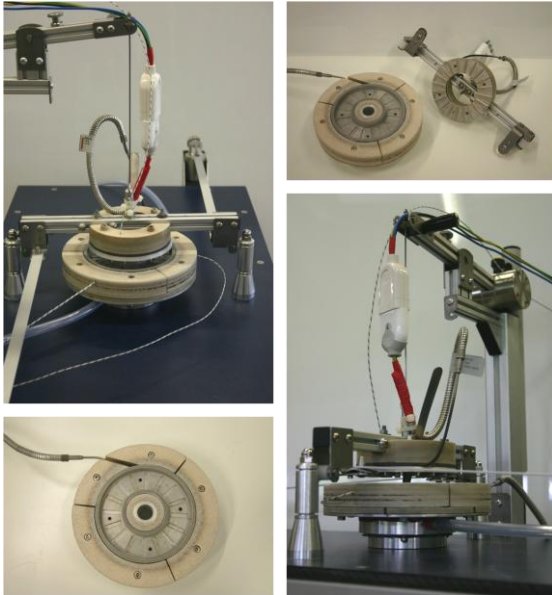


Figure III.3 *The modified High Temperature Annular Shear Cell.*

with the gears of the rotation mechanism of the tester. Indeed, in order to keep the cell base in contact with the instrument gears at room temperature, the insulating material below the trough of the cell is over a metal disk acting as a fin refrigerated by a water stream flowing inside a cavity in the ring at the base of the cell inserted in the rotating gear.

Figures III.2 and III.3 show some pictures of the original SV10 Schulze

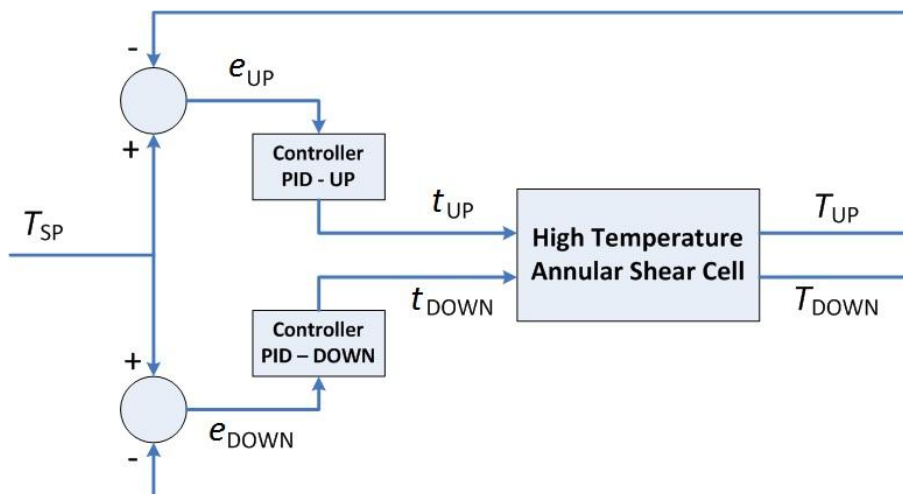


Figure III.4 *Logic of the temperature control of the High Temperature Annular Shear Cell.*

shear cell and the modified High Temperature Annular Shear Cell. The main data of the modified shear cell are listed in Table III.1.

III.1.1 Set-up of the High Temperature Annular Shear Cell

In this work, the set-up of the HT-ASC was performed.

A temperature control system was developed to achieve a constant temperature in the powder sample. In particular, the temperature vertical uniformity inside the powder sample is verified and controlled by a PID temperature control system. It consists of three J thermocouples measuring the temperature at three different depths of the sample. A dedicated

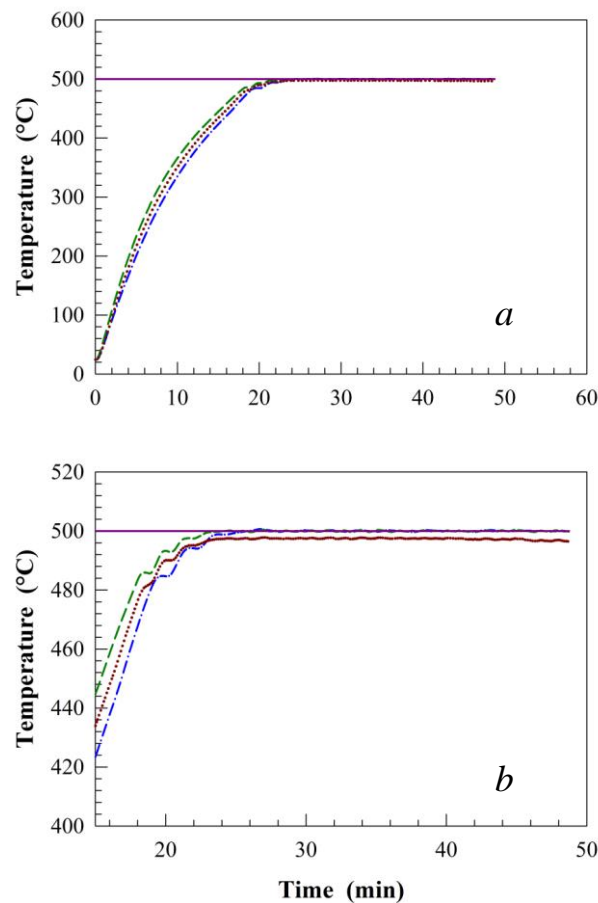


Figure III.5 Temperature vs. time inside the High Temperature Annular Shear Cell. Solid line (—): set point temperature, T_{SP} . Dashed line (---): lower temperature, T_{DOWN} . Dotted line (···): middle temperature, T_{MID} . Dash-dotted line (·-·): upper temperature, T_{UP} .

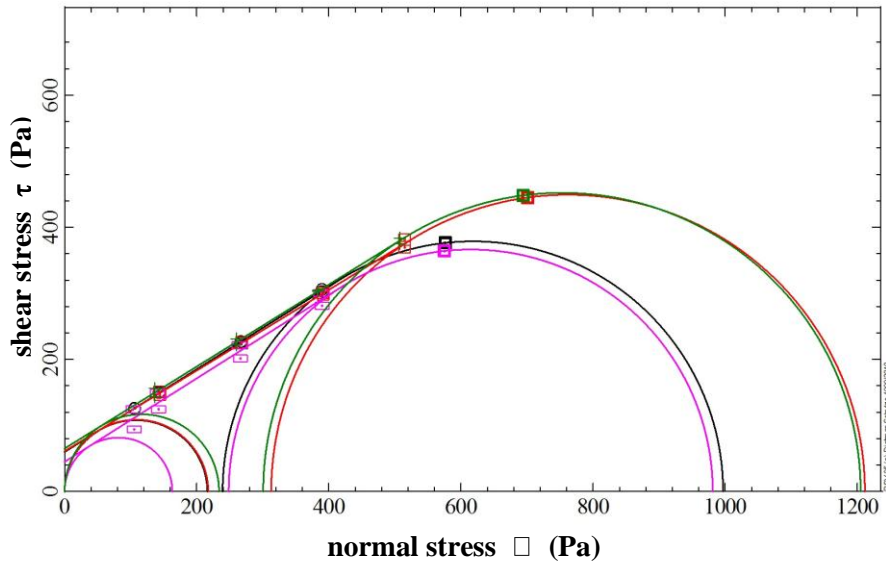


Figure III.6 Comparison between yield loci measurements for the FCC powder obtained at 20°C with the SV10 Shear Cell (○, $\sigma_1 = 997$ Pa; □, $\sigma_1 = 1211$ Pa) and the High Temperature Annular Shear Cell (□, $\sigma_1 = 981$ Pa; +, $\sigma_1 = 1205$ Pa).

LabView software was developed for this purpose.

It acquires these values for sample temperature monitoring. The top and bottom temperature, T_{UP} and T_{DOWN} , are compared with the set-point temperature T_{SP} in order to control with two separate PID loops the heating power on the lid and on the trough separately, as show in Figure III.4. The differences between T_{UP} , T_{DOWN} with T_{SP} , e_{UP} and e_{DOWN} respectively, define the time percentages t_{UP} and t_{DOWN} of an assigned period for which heaters are turned on. All PID parameters are set so that about 25 minutes are necessary to reach the steady state without temperature overshoots during experiments. Figures III.5a and III.5b show the temperature with the time during heating of the cell with a sample of FCC powder (see par. III.2) for a set-point temperature of 500°C. In particular, a constant temperature along the sample depth can be observed.

After the design of the temperature control system, the set-up of the HT-ASC was completed verifying the equivalence of the measurements performed by the modified shear cell with the original Schulze shear cell at room temperature.

A comparison between yield loci of FCC powders measured at room temperature by the High Temperature Annular Shear Cell and the standard Schulze Ring Shear Tester SV10 cell was performed for two specified normal load. Figure III.6 shows the good agreement between the experimental results, confirming the correspondence of the measurements

carried out by the modified High Temperature Annular Shear Cell and the original SV10 Shear Cell.

III.1.2 Procedure with the High Temperature Annular Shear Cell

The experimental procedure to evaluate high temperature yield loci of the material with the modified cell mainly followed the standard procedure for shear tests with the annular Schulze shear cell, with the two steps of *preshear* and *shear* previously described in par. I.4.2.

In this case, samples were subjected to a drying process in an oven at 200°C before filling the bottom ring of the cell and positioning it on the desk of the Ring Shear Tester in order to remove the volatile components (i.e. moisture contents). Indeed, for FCC powder, having a high content of humidity before the pretreatment, an upward gas flow through the gap between the lid and the outer wall of the trough of the cell was observed at about 150°C, invalidating the test (see par. IV.2)

Afterwards, thermocouples and cooling system are set and the lid and the weights for consolidation are placed according to the standard procedure. In order to achieve the desired operating temperature, before starting the shear test, heaters were activated and some time was waited to let the temperature reach the steady state at the desired value at all measurement points.

Each measurement was repeated twice.

III.2 Scanning Electron Microscope (SEM)

The Scanning Electron Microscope (SEM) is a type of microscope that uses a beam of electron to produce a magnified image of a sample. In a

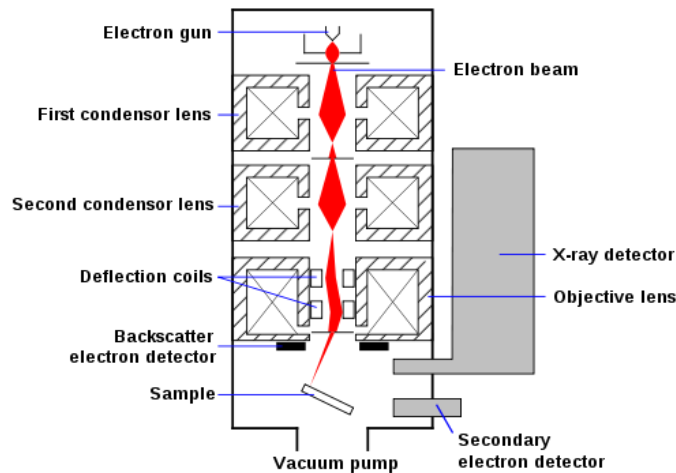


Figure III.7 Schematic of the Scanning Electron Microscope (SEM).



Figure III.8 *The Scanning Electron Microscope (SEM) ASSIGN mod. LEO 420 (Department of Industrial Engineering, University of Salerno).*

typical SEM an electron beam carrying a significant amount of kinetic energy passes through the sample and interacts with it. The beam decelerates and dissipates its energy as a variety of signals (secondary electrons, backscattered electrons, diffracted backscattered electrons, X-ray) which produce SEM images up to magnification about from about 10 to 500000 times and allow making evaluations about morphology and topography of the sample.

Figure III.7 shows a schematic of the Scanning Electron Microscope. In particular, the beam emitted by an electron gun is focused by one or two condenser lens before passing through deflection coils that deflect the beam so that the SEM furnishes a raster scan of the sample. Detectors of secondary and backscattered electrons necessary to produce the image of the sample complete the equipment.

Differently from an optical microscope that uses light to image the sample, and other type of electron microscope like TEM, SEM do not produces at any time images of the sample but provides raster scanning of the specimen.

In this work, SEM magnification of samples of experimental materials was performed by a SEM ASSIGN mod. LEO 420 available at the Department of Industrial Engineering of University of Salerno (Figure III.8) in order to analyze the shape and surface of the particles and to evaluate their role on the magnitude of interparticle interactions.

III.3 Differential Scanning Calorimeter (DSC)

Differential scanning calorimetry (DSC) is a technique that measures the energy necessary to maintain a nearly zero temperature difference between a substance and an inert reference material, as the two specimens are subjected

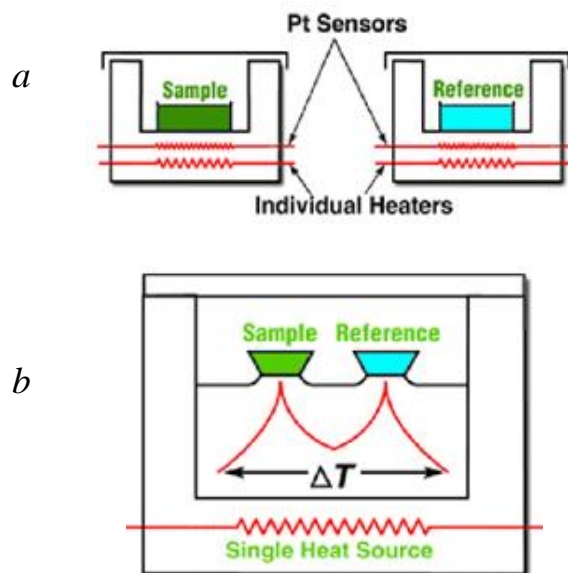


Figure III.9 Schematic of the Differential Scanning Calorimetry (DSC): (a) power compensation DSC; (b) heat-flux DSC.

to identical temperature regimes in an environment heated or cooled at a controlled rate. The basic principle of this technique is that when the sample undergoes a physical or chemical transformation, such as phase transitions or decomposition, more or less heat will need to flow to it than the reference to maintain both at the same temperature, depending on the process is exothermic or endothermic.

There are two types of DSC systems in common use.

In *power-compensation* DSC (Figure III. 9a) temperatures of the sample and reference are controlled independently using separate, identical furnaces. The temperatures of the sample and reference are made identical by varying the power input to the two furnaces; the energy required to do this is a measure of the enthalpy or heat capacity changes in the sample relative to the reference.

In *heat-flux* DSC (Figure III. 9b), as the apparatus DSC Mettler Toledo 822 used in this work and placed at the Department of Industrial Engineering of University of Salerno, the sample and reference are connected by a low-resistance heat-flow path. The assembly is enclosed in a single furnace. Enthalpy or heat capacity changes in the sample cause a difference in its temperature relative to the reference. The resulting heat-flow is small because the sample and reference are in good thermal contact and ensures the nearly zero temperature difference between the sample and the reference. The temperature difference is recorded and can be also related to the enthalpy change in the sample using calibration experiments.

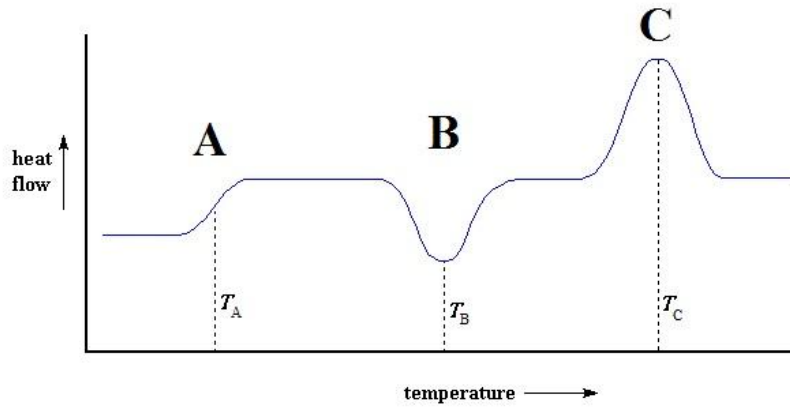


Figure III.10 Schematic representation of an experimental DSC curve indicating typical phenomena occurring during the analysis: (A) change of the heat capacity; (B), endothermic process; (C), exothermic process.

A typical experimental curve obtained by a DSC analysis is showed in Figure III.10. Assuming heat flow as positive when outgoing from the sample, a variation as occurs at point A indicates a change of the heat capacity, i.e. due to a glass transition. A negative peak, as point B, indicates that an endothermic process occurred, as melting or evaporation of the sample of a component of the materials. Likewise, the positive peak C signifies an exothermic process, as crystallization.

According to the objective of this PhD work, DSC analysis was performed in order to verify the occurring of transformation that, in such way, can affect the powder flow properties, like phase transitions. In particular, the temperature program adopted for these tests provides a linear temperature increase from 25°C to 500°C at 10°C/min, a time of 15 min during which the temperature is held constant and a linear temperature decrease from 500°C to 25°C at 10°C/min. The heat flow was assumed positive when outgoing from the sample.

III.4 Materials

Measurements of the flow properties were carried out on different experimental materials.

The particle size distributions of materials are showed in Figure III.11 (Malvern Instruments Mastersizer 2000).

In Table III.2 the main data of experimental materials are listed.

FCC powder is a zeolite mainly composed by silica and alumina. It is commonly used as catalyst in fluidized and mobilized bed in cracking of petroleum at temperatures higher than 650°C. The very large use in chemical

industry suggested to analyze the flow behaviour of this material at high temperature.

According to Xie (1997), the Hamaker constant and the compressive strength of silica were chosen.

Fly ashes are usually separated by hot flue gas of combustion. Although extensive efforts have been paid to develop dust collectors and filter capable to operate at higher than 800°C, many problems should still be solved. One of the most important issue is the raise of adhesive force of particle at high temperature which causes the raise of pressure drop and make the cleaning of filter surface affects the performance of dust collector, especially the release of dust from a filter element. For these reasons, the knowledge of the cohesive behaviour at high temperature is fundamental for the correct design of these devices and for the definition of the optimized working conditions. These powders show a wide particle size distribution with a high percentage of fines. Furthermore, because of the unknown composition, it was not possible to establish the Hamaker constant and the compressive strength of the material. For these reasons, it is not able to provide modeling or quantitative evaluations at particle level with these experimental materials.

Measurements at high temperature were performed on the same corundum powder for which Formisani *et al.* (2002) found a change of the porosity with the temperature in fixed and fluidized state not predictable with the classic equations as Ergun and Carman-Kozeny, taking into account only the hydrodynamic properties. In order to give a novel contribution to their research project, this material was kindly provided by these authors.

Yield loci at high temperatures were measured also for a sample of synthetic porous α -alumina. The same Hamaker constant, A , and the compressive strength, σ_f , were considered for this powder and corundum. Although corundum is the natural form of α -alumina, the traces of impurities and the different surface properties can imply difference in the behavior of the two

Table III.2 *Material properties*

	FCC powder	Fly ashes	Corundum	Alumina	Glass beads
ρ_p (kg m ⁻³)	1400	-	4000	1730	2200
d_{10} (μ m)	37.1	3.5	54.9	57.3	119.7
d_{50} (μ m)	72.8	27.2	84.1	96.8	163.4
d_{90} (μ m)	134.1	123.1	128.8	159.8	223.2
d_{sv} (μ m)	41.4	7.5	79.8	89.1	158.9
A (10 ⁻²⁰ J)	15.0	-	14.0	14.0	6.5
σ_f (GPa)	1.50	-	2.95	2.95	1.10

* (Israelachvili, 1992)

** (Shackelford *et al.*, 2000)

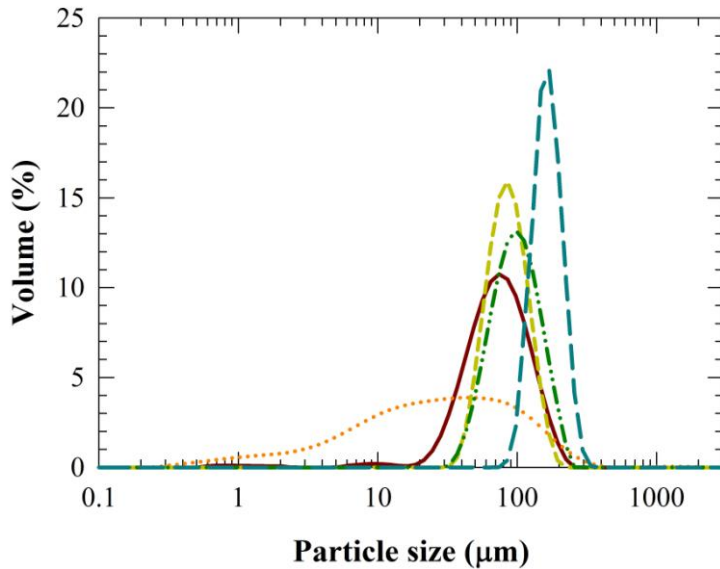


Figure III.11 Particle size distributions of experimental materials (for each class, $d_{i+1}/d_i = 1.148$). Solid line (—): FCC powder. Dotted line (⋯): fly ashes. Short dashed line: (---): corundum. Dash-dotted line (-·-·-): porous alumina. Long dashed line (- -): glass beads.

materials. The particle density ρ_p for alumina reported in Table IV.2 takes into account also the internal porosity of particles.

Finally, a sample of glass beads was analyzed as reference material.

Moreover, glass beads mixed with a sample of high-density polyethylene (HDPE) were studied. The objective was to observe experimentally on a prototype material the effect of temperature when liquid bridges and capillary forces occur. In fact, HDPE has a low melting point about 110°C . Therefore, a mixture of glass beads with a selected fraction of high-density polyethylene ($d_{0.1} = 113.0 \mu\text{m}$; $d_{0.5} = 214.6 \mu\text{m}$; $d_{0.9} = 391.8 \mu\text{m}$; $d_{SV} = 180.7 \mu\text{m}$) of the 1% of weight percentage was prepared.

Chapter IV

Experimental results

IV.1 SEM magnifications

SEM magnifications of sample of all materials were carried out in order to observe the shape and the surface properties of particle and to make qualitative and quantitative evaluations at the microscale level, in particular about the magnitude of the interparticle interactions and the their role affecting the flow properties of powders at high temperature as well as at room temperature.

Figure IV.1 reports the images of the performed SEM magnifications. They show a very rough surface for FCC particles and porous alumina differently from corundum and glass beads. Furthermore, the high sphericity shape of this material is the closest to the Rumpf and Molerus hypotheses in the derivation of their models, confirming the consistency to use glass beads as reference material. On the other hand, corundum powder is characterized by a very low sphericity.

For FCC, alumina and corundum, these evidences suggest to consider mean curvature radius at the contact point lower than the mean particle size for the quantitative evaluation of the interparticle forces. Finally, SEM magnification for fly ashes confirms the wide range of particle size while particles of HDPE can be clearly observed in Figure IV.1f, mixed to the glass beads.

IV.2 DSC analysis

In order to evaluate the thermal behaviour of materials and better understand the physical phenomena occurring between particles at high temperature, DSC (Differential Scanning Calorimetry) analysis were performed on the experimental materials.

According to the objective of this PhD work, DSC analysis was performed in order to verify the occurring of transformation that, in such way, can affect the powder flow properties, like phase transitions. In

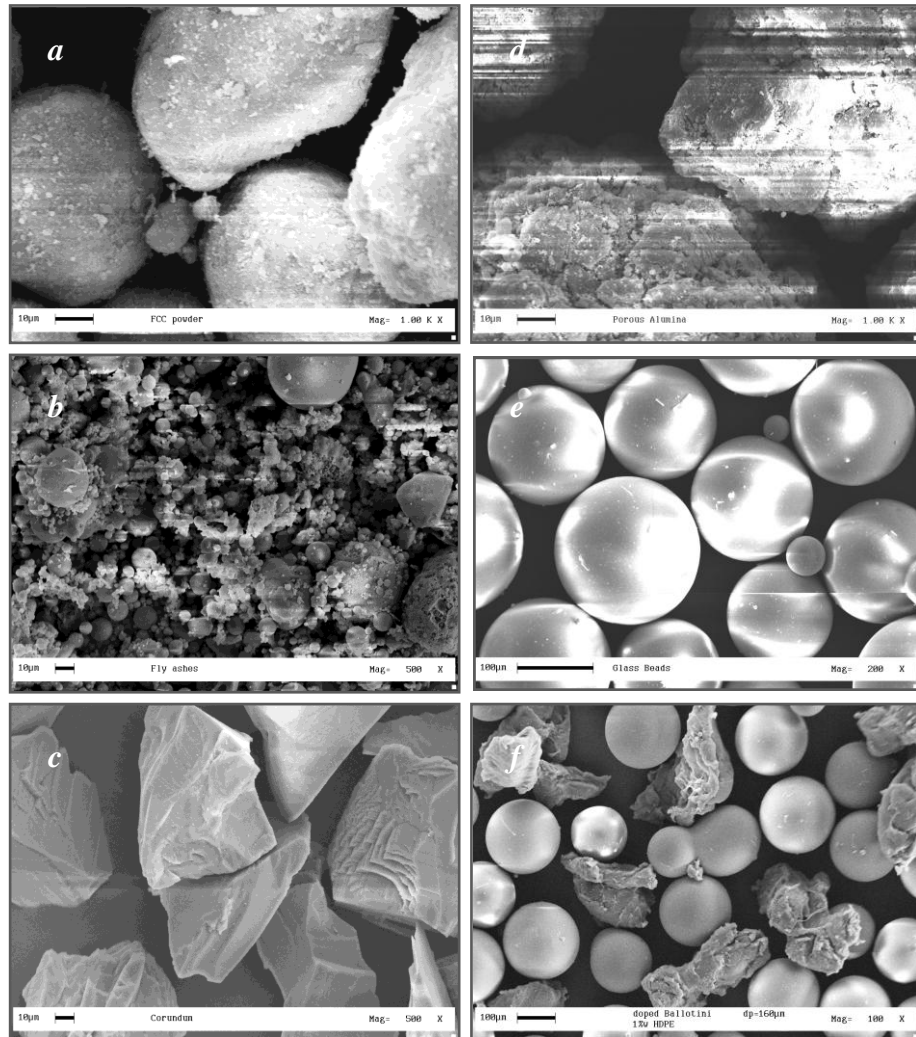


Figure IV.1 SEM magnifications of experimental materials; (a) FCC powder ($X = 1000$); (b) fly ashes ($X = 500$); (c) corundum ($X = 500$); (d) porous alumina ($X = 1000$); (e) Glass beads ($X = 200$); (f) Glass beads mixed with HDPE (1%w) ($X = 100$).

particular, the temperature program adopted for these tests provides a linear temperature increase from 25°C to 500°C at 10°C/min, a time of 15 min during which the temperature is held constant and a linear temperature decrease from 500°C to 25°C at 10°C/min. The heat flow was assumed positive when outgoing from the sample.

Figures IV.2a and IV.2b report the DSC curve for FCC powder before and after the drying of the sample of the material in an oven at 200°C, according to the procedure for shear test with HT-ASC (par. III.1.2). The

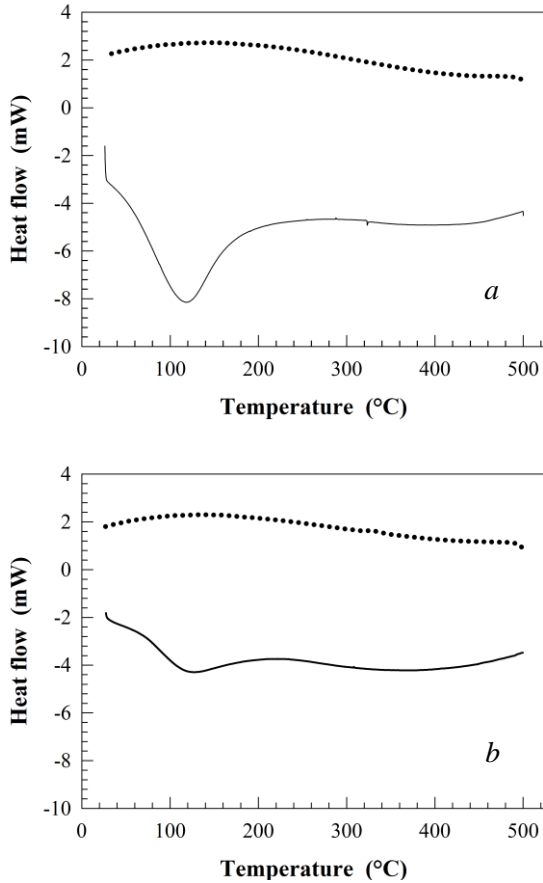


Figure IV.2 DSC analysis of FCC powder before (a) and after (b) the drying of the sample at 200°C. Solid line (—): increasing temperature. Dotted line (····): decreasing temperature.

more prominent negative peak slightly about 100°C of the first case is due to the presence of moisture which evaporates at this temperature. In fact, a humidity of 8.70% was measured for FCC powder before the pretreatment in front of a 1.39% of the second case (OHAUS Humidity Analyzer MB45), confirming that a drying treatment is necessary before the tests. However, no melting points were observed up to 500°C.

The behaviour of fly ashes in the DSC test is showed in Figure IV.3. The two small negative peaks at about 50°C and under 450°C are probably due to the presence of impurities in the sample which disappears during the decreasing temperature step.

For the corundum powders, porous alumina and glass beads, nothing significant was observed during the DSC test. For these materials, like for

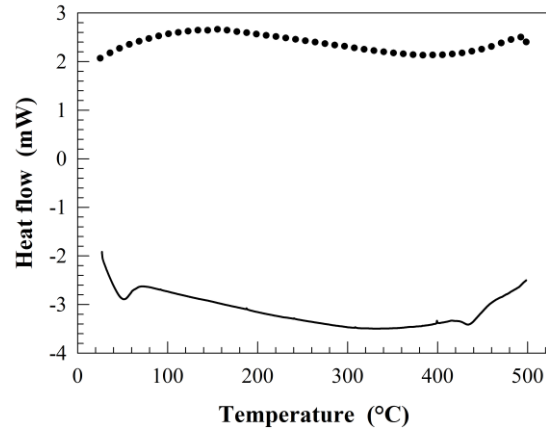


Figure IV.3 DSC analysis of fly ashes. Solid line (—): increasing temperature. Dotted line (····): decreasing temperature.

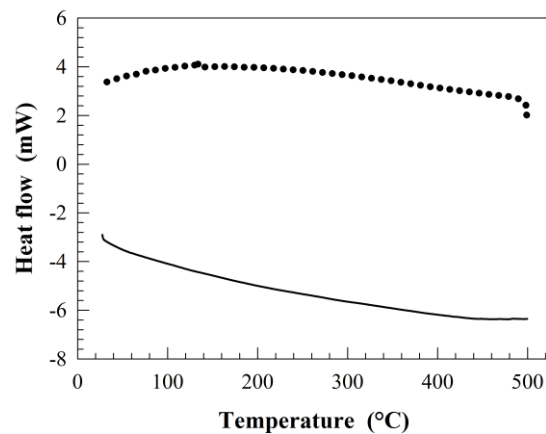


Figure IV.4 DSC analysis of corundum powder. Solid line (—): increasing temperature. Dotted line (····): decreasing temperature.

fly ashes, DSC analysis show there are not melting points or other phase transitions in this temperature range, as reported in Figures IV.4, IV.5 and IV.6.

For these materials no liquid bridges occur during tests and interparticle interactions are not related to capillary forces.

On the other hand, the DSC curve of high-density polyethylene (HDPE), reported in Figure IV.7, shows a phase transition corresponding to the melting of the material between 100°C and 120°C. This test was performed with a different temperature program, providing a linear temperature

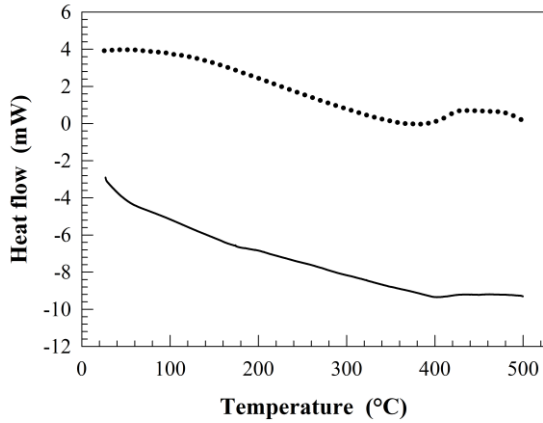


Figure IV.5 DSC analysis of porous alumina. Solid line (—): increasing temperature. Dotted line (····): decreasing temperature.

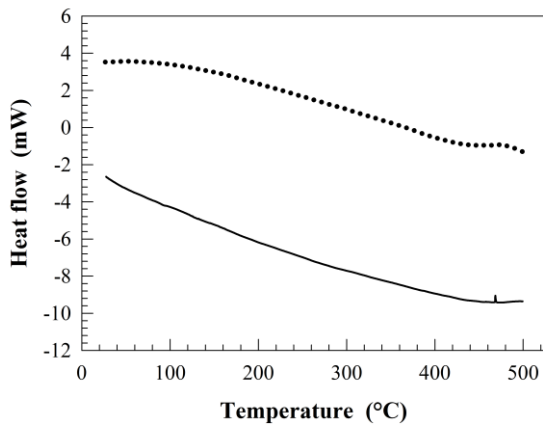


Figure IV.6 DSC analysis of glass beads. Solid line (—): increasing temperature. Dotted line (····): decreasing temperature.

increase from 25°C to 250°C at 10°C/min, a time of 15 min during which the temperature is held constant and a linear temperature decrease from 250°C to 25°C at 10°C/min. For the mixture of glass beads and HDPE liquid bridge will occur during shear test performed at temperature higher than the melting point.

IV.3 Experimental measurements of flow properties with HT-ASC

After the set-up of the High Temperature Annular Shear Cell through which the ability of the modified shear cell to correctly operate up to 500°C

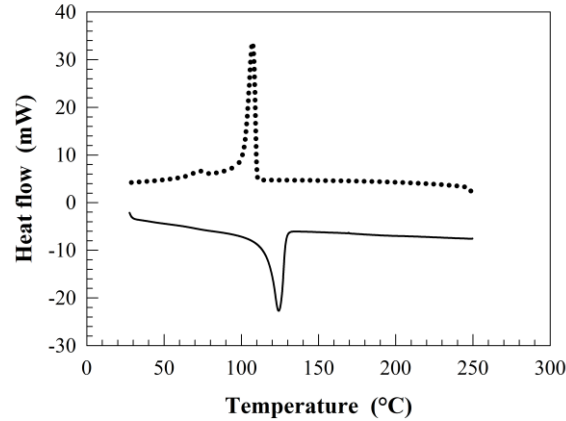


Figure IV.7 DSC analysis of high-density polyethylene. Solid line (—): increasing temperature. Dotted line (····): decreasing temperature.

was verified, yield loci and powder flow properties are directly measured for specified conditions of consolidation and temperature in order to highlight the effect of temperature on the flow behaviour of powders.

In this section, experimental results are distinctly reported for each experimental material. All experimental values are listed in Table IV.1 at the end of the chapter.

IV.3.1 FCC powder

Yield loci of the FCC powder were measured at 20°C (room temperature) and 500°C.

In order to extend the experimental evidences to fluidized condition, in which FCC powder is commonly utilized in chemical industry, shear tests were performed at low consolidation level for major principal stress σ_1 about 1000 Pa and 1200 Pa.

Measured yield loci are reported in Figure IV.8. Although a shift upwards with the temperature was observed at $\sigma_1 \approx 1000$ Pa, the same behaviour is not repeated at higher consolidation level. Inspection of the flow functions in Figure IV.9 does not show a significant change of the flow properties of FCC powder with the increasing temperature. In particular, experimental results do not evidence a monotone behaviour.

Somehow, this was expected. FCC powder is commonly used as catalyst of cracking of oil in fluidized bed and it is desirable that the flow properties of this powder do not change up to the operating temperature of 650–750°C. On the other hand, it is not in agreement with the results of Xie and Geldart (1995), for which the inability to estimate the properties of fluidized bed at

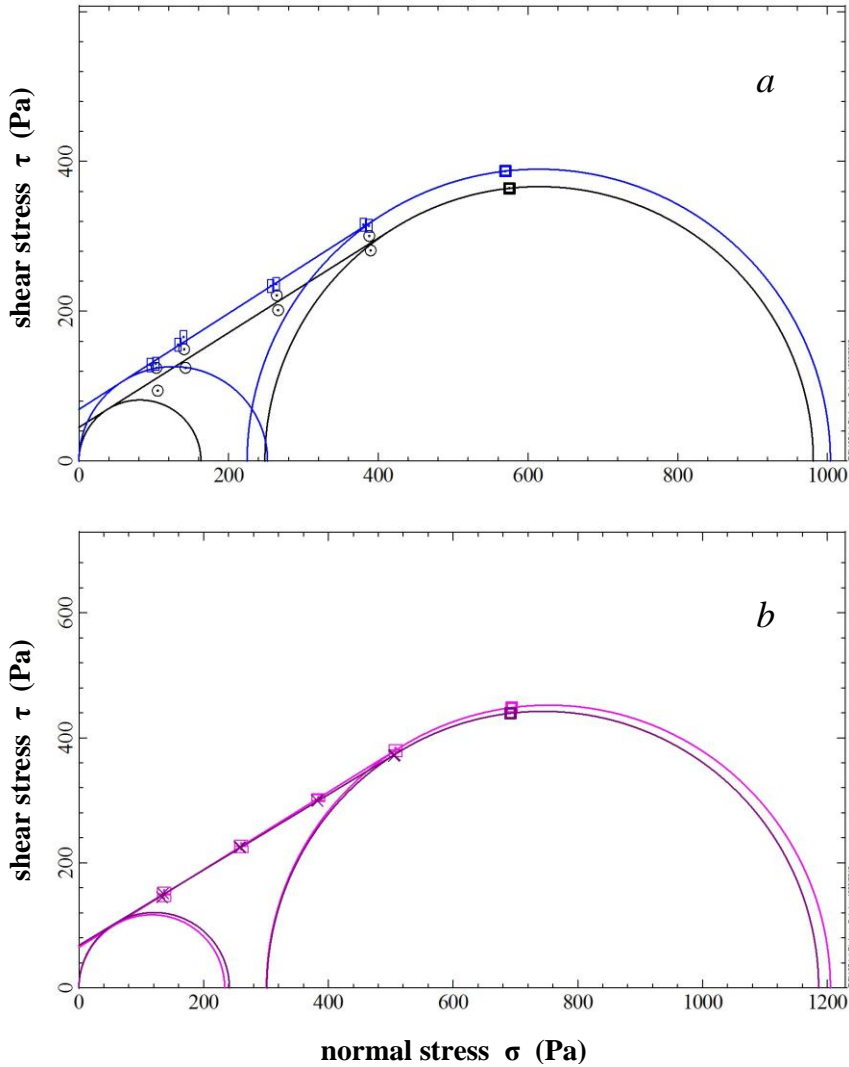


Figure IV.8 Measured yield loci for FCC powder with HT-ASC at (a) $\sigma_1 \approx 1000 \text{ Pa}$ (\circ : $\sigma_1 = 997 \text{ Pa}$, $T = 20^\circ\text{C}$; \square : $\sigma_1 = 1004 \text{ Pa}$, $T = 500^\circ\text{C}$) and (b) $\sigma_1 \approx 1200 \text{ Pa}$ (\square : $\sigma_1 = 1205 \text{ Pa}$, $T = 20^\circ\text{C}$; \times : $\sigma_1 = 1186 \text{ Pa}$, $T = 500^\circ\text{C}$).

high temperature by classic correlations based only on hydrodynamic hypotheses was the result of the increase of the relative weight of the interparticle forces.

However, measurements performed at the lower consolidation levels do not appear fully reliable. This is probably due to the contribution of the forces exerted on the cell lid by the electric wiring of the lid heater that

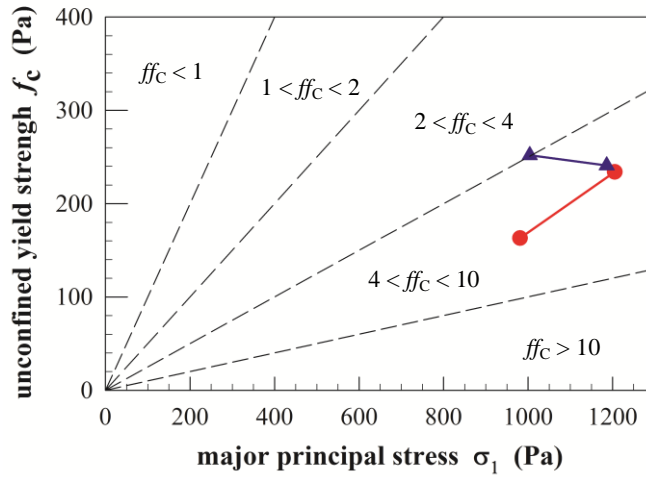


Figure IV.9 Measured flow function of FCC powder at 20°C (●) and 500°C (▲).

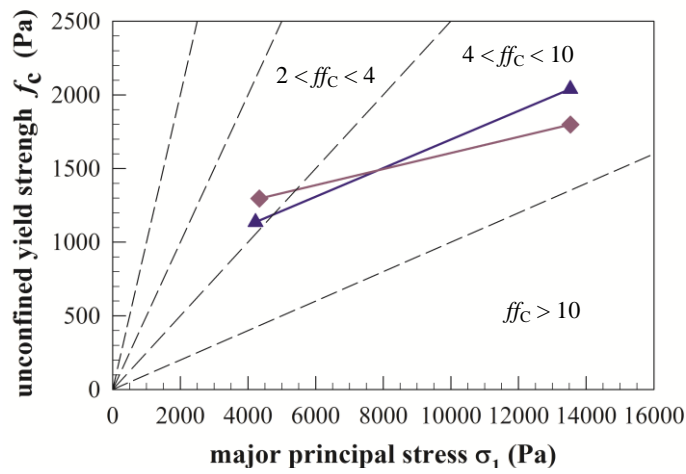


Figure IV.10 Measured flow function for fly ashes at 20°C (▲) and 500°C (◆).

should be completely isolated. These contributions are difficult to be completely neutralized or accurately accounted for and have a non negligible effect on the points of the yield loci as the measurements were performed at low σ values.

For this reason, tests for all the other materials were performed at higher consolidation loads.

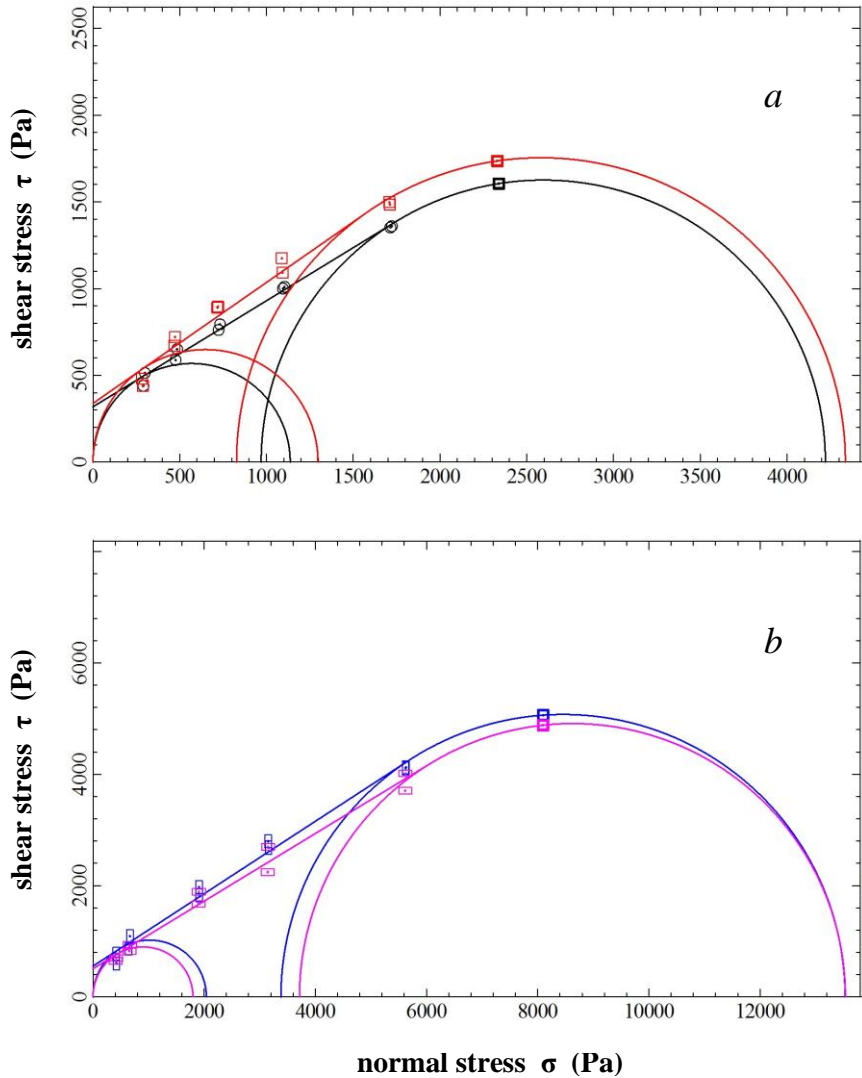


Figure IV.11 Measured yield loci for fly ashes with HT-ASC at (a) $\sigma_1 \approx 4000$ Pa (\circ : $\sigma_1 = 4221$ Pa, $T = 20^\circ\text{C}$; \square : $\sigma_1 = 4336$ Pa, $T = 500^\circ\text{C}$) and (b) $\sigma_1 \approx 13500$ Pa (\circ : $\sigma_1 = 13530$ Pa, $T = 20^\circ\text{C}$; \square : $\sigma_1 = 13534$ Pa, $T = 500^\circ\text{C}$).

IV.3.2 Fly ashes

The cohesive behaviour at high temperature of fly ashes affects the correct working of filters and separators of flue gases of combustion.

For this powder, shear tests were performed at 20°C and 500°C for normal consolidation stress σ_1 about 4000 and 13500 Pa.

Figures IV.10 and IV.11 represent flow function and yield loci evaluated at room and high temperature.

Also in this case, the flow properties of powder samples do not show significant change with the temperature.

IV.3.3 Corundum

Measured flow functions and yield loci for corundum powders at 20°C and 500°C for major principal stress σ_1 about 4500 Pa and 14000 Pa are shown in Figure IV.12 and IV.13

These experimental evidences, for which no significant variation of flow behaviour of powder was observed, are not in agreement with the conclusions of Formisani *et al.* (2002). In fact, in the absence of electrostatic and capillary forces, they attributed the increase of the voidage in fixed and fluidized state at high temperature as an increase of the van der Waals forces and not only to the effect of the increase of viscosity of the fluidizing gas. According to these authors, the increase of van der Waals interactions should have increased the cohesive behaviour of powders and flow properties as the cohesion and the unconfined yield strength. On the other hand, Figure IV.12 shows flow functions evaluated at room and high temperature almost overlapped as well as the results reported in Table IV.1 does not differ significantly. The particle-particle analysis developed in detailed in chap. V will try to interpret this experimental evidences and the physical phenomena occurring at microscale.

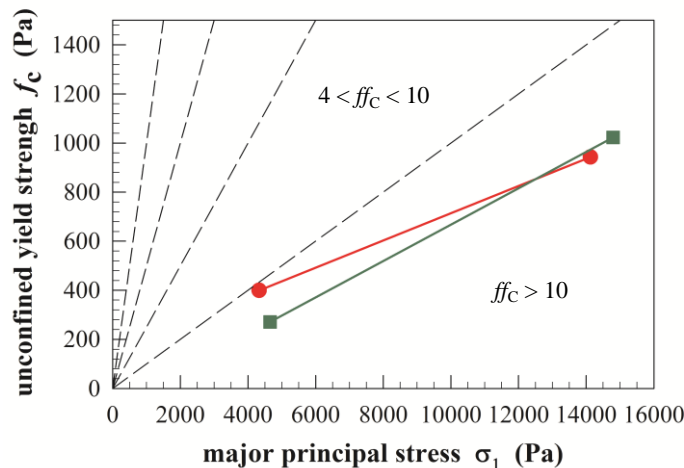


Figure IV.12 Measured flow function for corundum powder at 20°C (●) and 500°C (■).

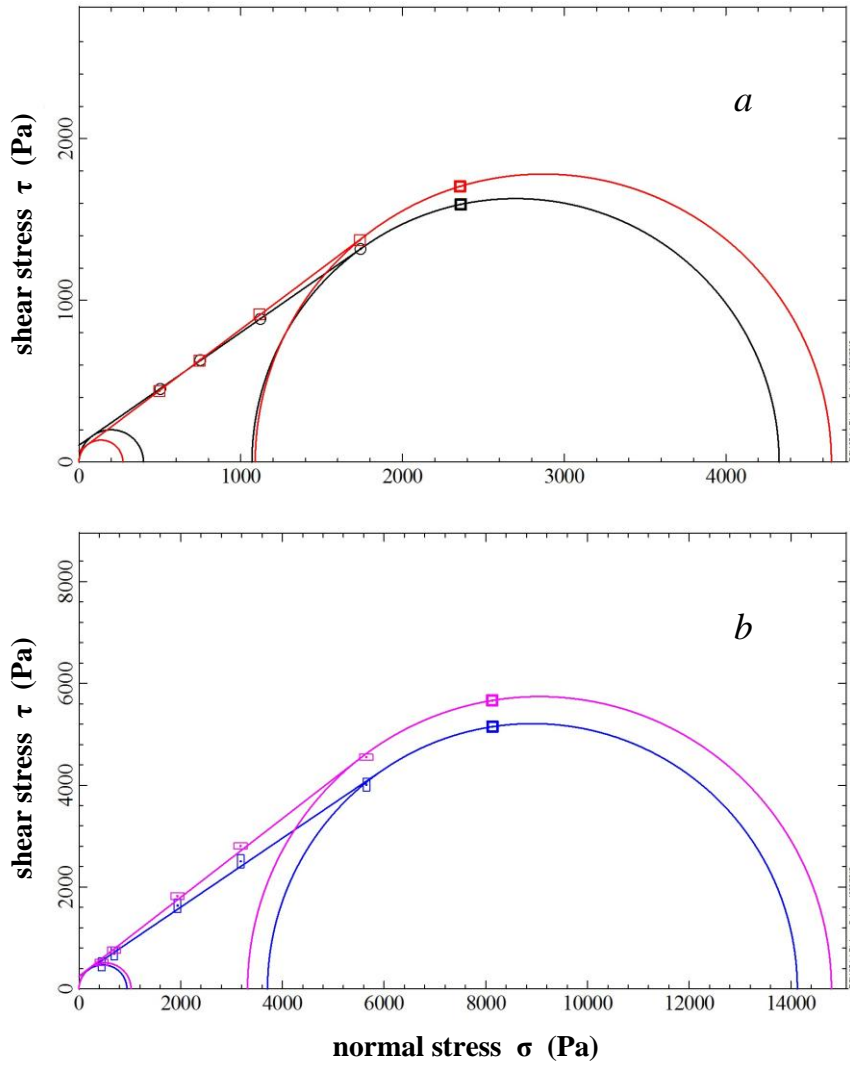


Figure IV.13 Measured yield loci for corundum powder with HT-ASC at (a) $\sigma_1 \approx 4500$ Pa (\circ : $\sigma_1 = 4329$ Pa, $T = 20^\circ\text{C}$; \square : $\sigma_1 = 4652$ Pa, $T = 500^\circ\text{C}$) and (b) $\sigma_1 \approx 14000$ Pa (\square : $\sigma_1 = 14126$ Pa, $T = 20^\circ\text{C}$; \square : $\sigma_1 = 13795$ Pa, $T = 500^\circ\text{C}$).

IV.3.4 Alumina

A sample of a synthetic porous α -alumina powder was tested for major principal stress σ_1 about 4000 Pa and 13500 Pa at room temperature and 500°C .

Differently from natural corundum, a very small increase of the cohesion occurs in this temperature range. Although yield loci measured at room and high temperature in Figure IV.14 are as good as overlapped, this slight effect appears more clearly comparing the flow functions at 20°C and 500°C (Figure IV.15). On the other hand, the level of consolidation does not affect the cohesive behaviour of powder, with an unconfined yield strength f_c virtually constant with the major principal stress σ_1 .

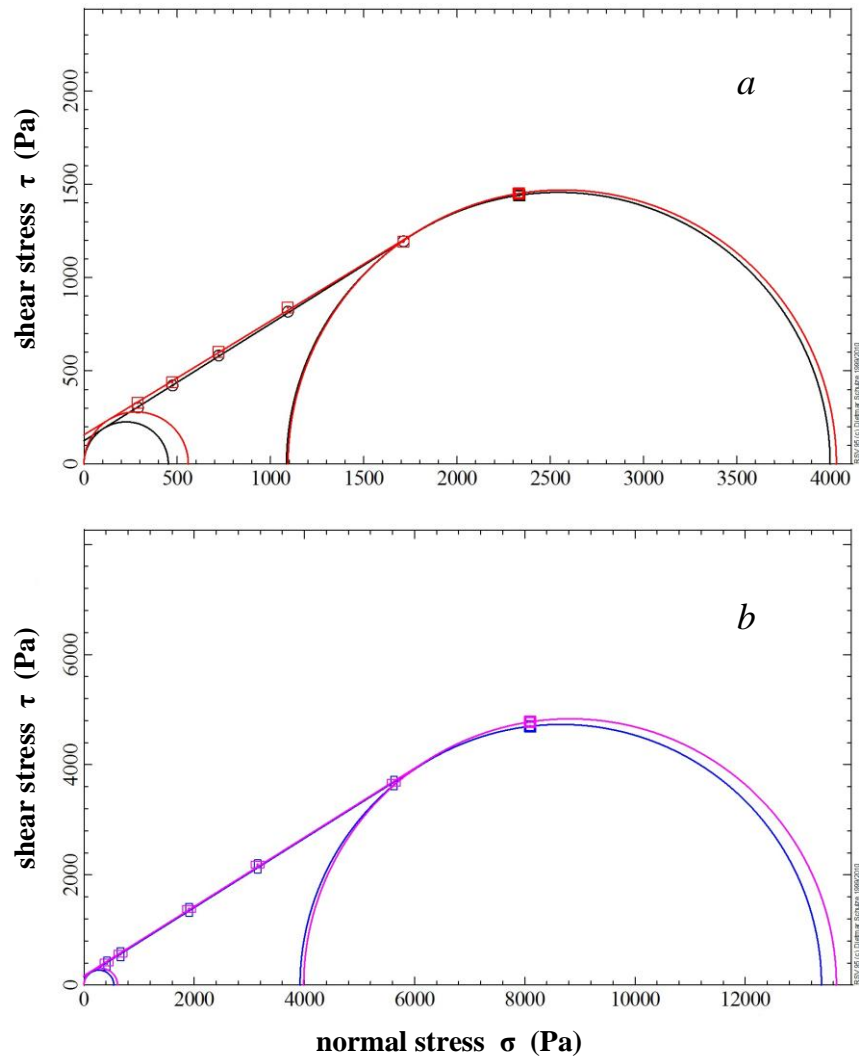


Figure IV.14 Measured yield loci for porous alumina with HT-ASC at (a) $\sigma_1 \approx 4000$ Pa (\circ : $\sigma_1 = 4000$ Pa, $T = 20^\circ\text{C}$; \square : $\sigma_1 = 4033$ Pa, $T = 500^\circ\text{C}$) and (b) $\sigma_1 \approx 13500$ Pa (\blacksquare : $\sigma_1 = 13384$ Pa, $T = 20^\circ\text{C}$; \square : $\sigma_1 = 13654$ Pa, $T = 500^\circ\text{C}$).

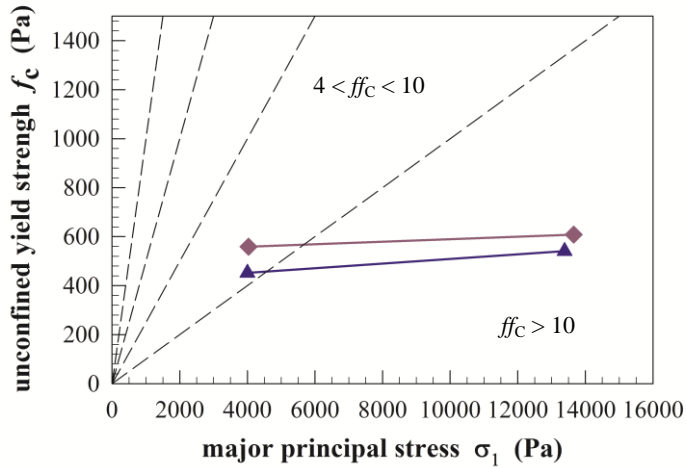


Figure IV.15 Measured flow function for porous alumina at 20°C (▲) and 500°C (◆).

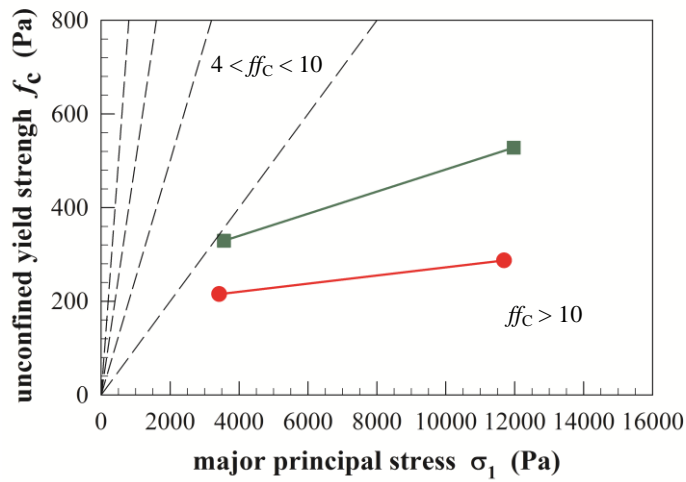


Figure IV.16 Measured flow function for glass beads at 20°C (●) and 500°C (■).

IV.3.5 Glass beads

For their perfectly spherical shape and smooth surface, as showed in SEM magnification (Figure IV.1e), so that to be considered a model material related to the particle-particle approach developed b Rumpf (1974) and

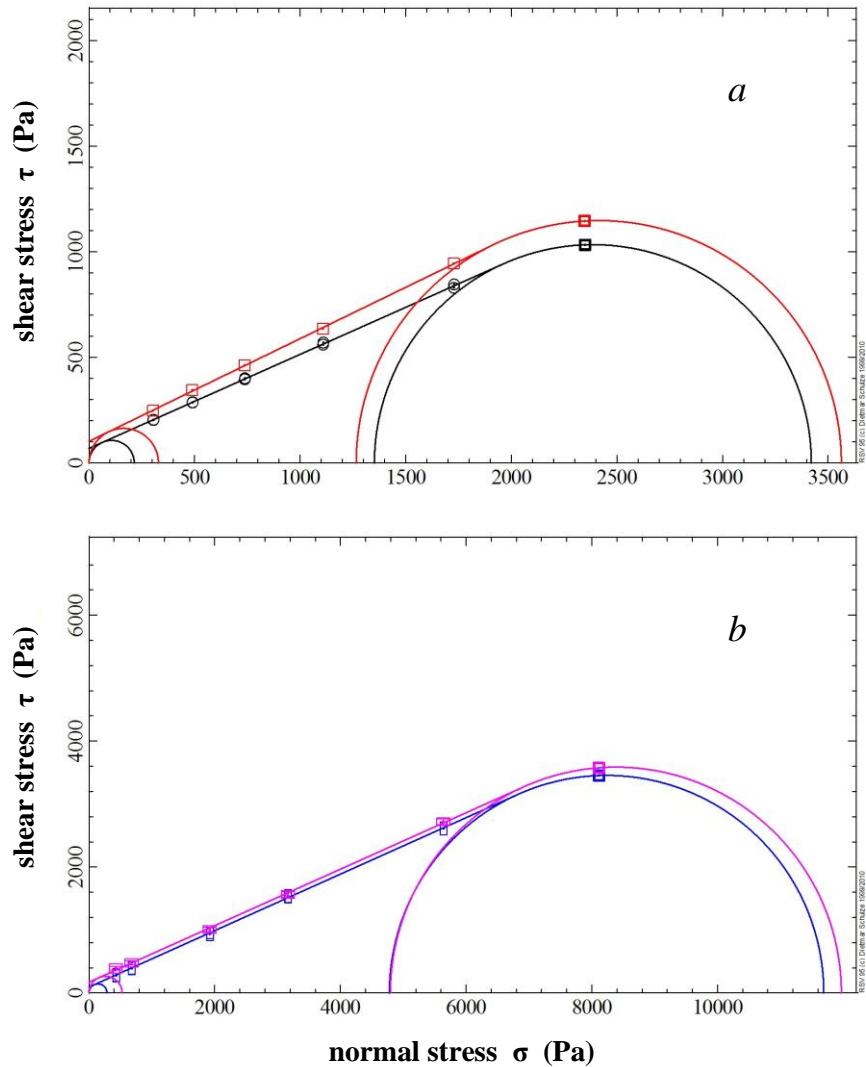


Figure IV.17 Measured yield loci for glass beads with HT-ASC at (a) $\sigma_1 \approx 3500$ Pa (○: $\sigma_1 = 3421$ Pa, $T = 20^\circ\text{C}$; □: $\sigma_1 = 3563$ Pa, $T = 500^\circ\text{C}$) and (b) $\sigma_1 \approx 12000$ Pa (□: $\sigma_1 = 11689$ Pa, $T = 20^\circ\text{C}$; □: $\sigma_1 = 11970$ Pa, $T = 500^\circ\text{C}$).

Molerus(1993), shear tests at high temperature were performed with glass beads.

In particular, yield loci at room temperature and 500°C were evaluated for compaction about 3500 Pa and 12000 Pa (Figure IV.17). In this case, differently from the other materials, a small but significant increase of cohesion and, therefore, of the flow factor were observed, as reported in

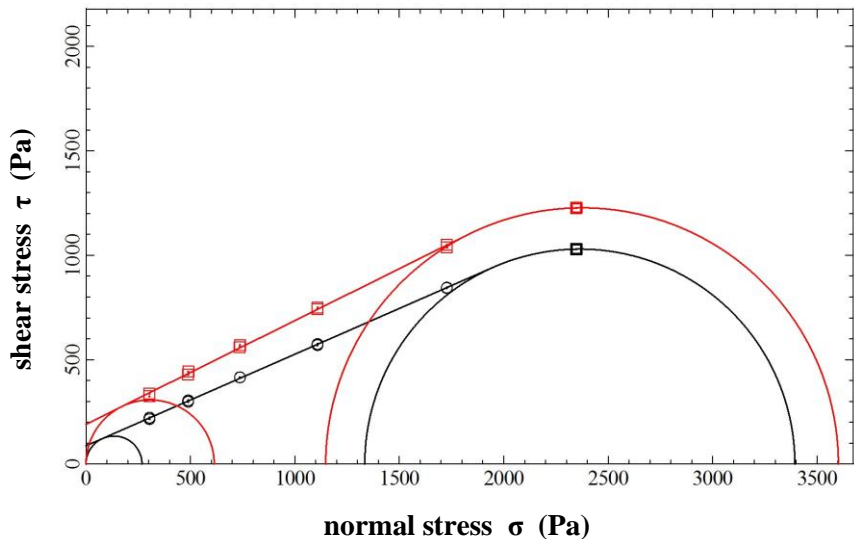


Figure IV.18 Measured yield loci for the mixture of glass beads and HDPE (1%w) measured with HT-ASC at 100°C (O) and 125°C (□) for major principal stress about 3500 Pa.

Table IV.1. It appears more clearly observing flow functions, in Figure IV.16. Although the flow behaviour of powder remains in the free flowing field ($ff_c > 10$) according to the Jenike classification (1964), a reduction of the flow factor from about 30% to 50% was observed. Furthermore, the effect is more evident for the higher consolidation level.

IV.3.6 Glass beads mixed with 1%w of high density polyethylene

The experimental evidences reported in literature induced to analyze the behaviour of powder sample for which some components melt and liquid bridges form, in order to verify the role of the capillary forces on the flow properties of bulk solids at high temperature.

For this purpose, a mixture of pure glass beads and 1%w of HDPE was tested at room temperature, 75°C, 100°C, 125°C, 150°C and 200°C for the specified consolidation stress σ_1 about 3500 Pa. All the experimental results are reported in Table IV.1.

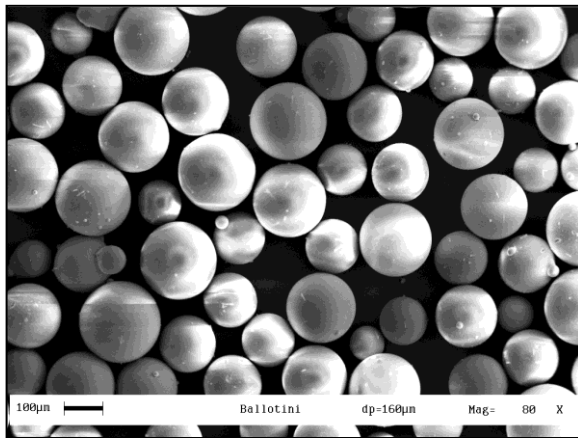
In this case, the powder flow properties did not change up to 100°C, before the melting temperature of HDPE, according to the thermal behaviour observed by DSC analysis (par. IV.2). From 100°C to 125°C, the cohesion immediately increase with significant variations of the powder flow properties. Figure IV.18 represents yield loci measured at 100°C and 125°C where it appears clearer. On the other hand, flow properties remain constant from 125°C to 200°C.

This large enhance of the cohesive behaviour from room to high temperature is attributed to the formation of liquid bridges between particles and the onset of capillary forces between particles that are 2-3 orders of magnitude higher than van der Waals' forces.

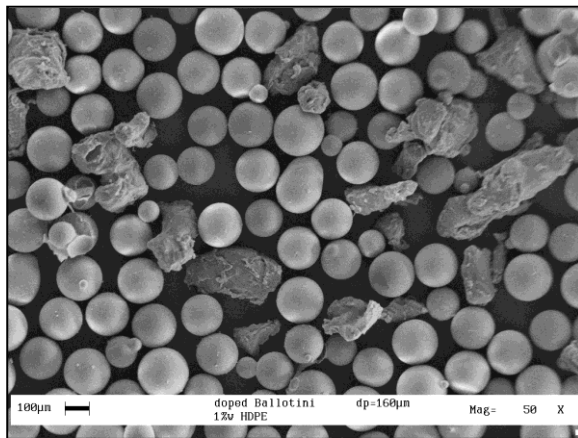
In Figure IV.19, a comparison between “pure” glass beads and the mixture of glass beads and HDPE at room temperature and after a shear test at 125°C is reported. Inspection of this figure shows aggregates in the powder sample formed by the melting of the HDPE particles that remain stable also when the sample returns to the room temperature, at which SEM visualizations were carried out.

The presence of aggregates localized in different point inside in the powder sample which are not homogeneously distributed in the bulk solid is not in agreement with the hypothesis of the theory of Rumpf and Molerus which provides uniform packing and forces transmitted with contact point at the surface of the particles.

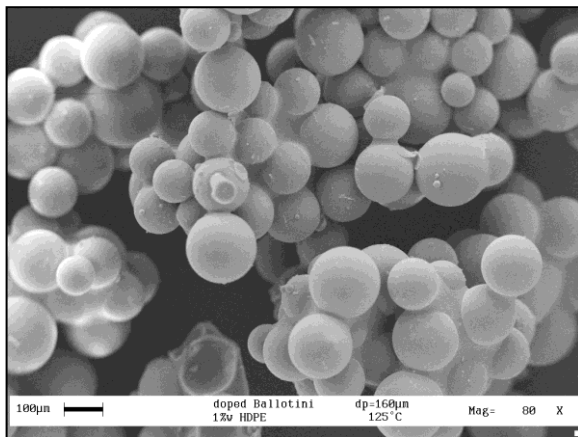
Therefore, the particle-particle analysis, developed in successful chapter, may not be extended to this system. However, these results confirm the experimental evidences reported in literature (Kanaoka *et al.*, 2001; Kamiya *et al.*, 2002; Hurley *et al.*, 2006; Zimmerlin *et al.*, 2008) for which a large increase of the cohesive behaviour of bulk solid at high temperature attains if liquid bridge or sintering take place.



a



b



c

Figure IV.19 SEM magnification of samples of (a) glass beads ($X = 80$); (b) glass beads + HDPE (1%w) at room temperature ($X = 50$); (c) glass beads + HDPE (1%w) after a shear test at 125°C ($X = 80$).

Table IV.1 Results of measurements performed with HT-ASC

Material	T (°C)	σ_1 (Pa)	C (Pa)	ϕ (-)	ϕ_e (-)	f_c (Pa)	ff_c (-)	σ_t (Pa)
FCC powder	20	981	45	32.3	36.6	163	6.02	71.2
FCC powder	500	1004	69	32.7	39.4	252	3.98	107.5
FCC powder	20	1205	65	31.8	36.9	234	5.15	104.8
FCC powder	500	1186	68	31.1	36.5	241	4.92	112.7
Fly ashes	20	4221	319	31.4	38.8	1137	3.71	522.6
Fly ashes	500	4336	338	34.9	42.8	1297	3.34	484.5
Fly ashes	20	13530	553	33.0	36.9	2040	6.63	851.5
Fly ashes	500	13534	506	31.3	34.7	1799	7.52	832.2
Corundum	20	4329	104	34.9	37.1	399	10.86	149.0
Corundum	500	4652	68	37.0	38.3	271	14.98	90.2
Corundum	20	14126	250	34.1	35.7	943	17.14	369.2
Corundum	500	14795	251	37.7	39.3	1023	14.46	324.7
Alumina	20	4000	125	32.1	35	452	8.84	199.3
Alumina	500	4033	157	31.4	35	559	7.21	257.2
Alumina	20	13384	149	32.1	33.1	541	24.74	237.5
Alumina	500	13654	168	32.1	33.2	608	22.44	267.8
Glass beads	20	3421	70	24.0	25.7	215	15.94	157.2
Glass beads	500	3563	103	25.9	28.3	329	10.83	212.1
Glass beads	20	11689	93	24.2	24.8	287	40.76	206.9
Glass beads	500	11970	171	24.2	25.3	528	22.67	380.5
Glass beads + 1%w HDPE	20	3419	82	24.6	26.6	255	13.43	179.1
Glass beads + 1%w HDPE	75	3364	80	23.8	25.8	244	13.77	181.4
Glass beads + 1%w HDPE	100	3393	88	23.7	25.8	268	12.65	200.5
Glass beads + 1%w HDPE	125	3602	190	26.4	31.1	614	5.87	382.8
Glass beads + 1%w HDPE	150	3592	202	25.8	30.8	643	5.59	417.9
Glass beads + 1%w HDPE	200	3493	205	24.8	29.8	641	5.57	443.7

Chapter V

Model results and sensitivity analysis

V.1 Estimate of the mean curvature radius at contact points

Except for the glass beads mixed with low-melting HDPE, the experimental conditions at which shear test were performed provided absence of electrostatic and capillary forces. Furthermore, drying in oven at 200°C before shear tests and the high temperature ensures the absence of liquid bridge due to the humidity. DSC analysis confirmed the absence of melting point for each experimental material in the range of operating temperature. Therefore, the interparticle interactions occurring in these cases can be associated only to van der Waals' forces.

In general, a not univocal effect of temperature on the powder flow properties was observed experimentally. In fact, although for FCC powders, fly ashes and corundum no change with the temperature was measured, a very small increase and a more significant enhance of the cohesion appear from shear tests on porous alumina and glass beads respectively.

A quantitative evaluation was performed in order to better understand the kind of interparticle interactions occurring inside the shear cell, to give an interpretation of the physical phenomena that takes place at room and high temperature at the particle-particle level and to correlate the powder flow properties with the forces that acts between particles with the aim to extend the experimental findings to different compaction conditions.

In particular, a theoretical framework was developed according to the theory of Rumpf (1974) and Molerus (1985 and 1993), already introduced in section I.6. In this approach the following assumptions were considered:

1. particles are assumed to be spherical;
2. the contact areas between particles are small enough in comparison with the particle surfaces. Consequently, contact areas can be assumed as contact points;

3. the contact points are distributed over the sphere surface with equal probability;
4. the packing structure is isotropic;
5. the transmission of an isostatic state of compressive stress occurs with three equal principal stresses.

Following these assumptions, the proper hypothesis made in this work considers the theoretical condition of the tensile strength σ_t as representing a bulk solid in which only van der Waals' kind of forces, F_{vdW} , act at the contact points between particles considering environmental conditions in which liquid bridges and electrostatic forces do not occur, as mentioned above. In fact, tensile strength represents the tensional state of a bulk solid in which only normal binary forces act between particles, without any shear stress or external normal load to take into account. According to this hypothesis, eq. (I.38) is valid for this analysis. Finally, the particle Sauter mean diameter d_{SV} appears in place of the uniform particle diameter as representative of the size distribution of particles and eq. (I.38) becomes:

$$\sigma_t = \frac{F_{vdW}}{d_{SV}^2} \frac{(1-\varepsilon)}{\varepsilon} \quad (V.1)$$

In particular, in this study two main cases were studied, as described in detail in par. I.6.1:

1. a reversible elastic behaviour of powder, for which van der Waals interactions in tensile condition are described by eq. (I.7):

$$F_{vdW} \approx \frac{A\delta}{12z_0^2} \quad (I.7)$$

2. an irreversible plastic behaviour, for which flattenings occur at contact points between particles due the external load applied during the preconsolidation of the powders at the *preshear* of the shear test. In this case, the van der Waals' force can be expressed by eq. (I.37):

$$F_{vdW} = \frac{A\delta}{12z_0^2} \frac{1 + (2F_N/\pi p_f \delta z_0)}{1 - (A/6\pi p_f z_0^3)} \quad (I.37)$$

where p_f is plastic compression yield pressure of hindered material that, according to Molerus (1993), is related to the compressive yield strength σ_f as $p_f \approx 3\sigma_f$ and F_N is the compressive contact force exerted during the *preshear* that, likewise eq. (V.1), is equal to:

$$F_N = \frac{\sigma_f \varepsilon d_{SV}^2}{(1-\varepsilon)} \quad (V.2)$$

defining an implicit dependence of the tensile strength σ_t with the major principal stress σ_1 for the case of plastic deformation.

The main problem of this approach is related to the difficulty to know with greater accuracy the properties of materials appearing in previous equations, such as the Hamaker constant A , the compressive strength σ_f and

Table V.1 Best fitting mean curvature radius δ^* assuming elastic (δ_{el}^*) and plastic (δ_{pl}^*) deformation

	FCC powder	Corundum	Alumina	Glass beads
δ_{el}^* (μm)	1.04	8.57	14.5	78.1
δ_{pl}^* (μm)	0.81	7.75	7.37	27.7

the mean curvature radius δ . In fact, the impossibility of finding these data for fly ashes because of the unknown composition of this material did not allow performing this analysis on it. Furthermore, the voidage calculated from the height of the powder sample in the shear cell is only an averaged value and is not representative of the local value in the shear zone which develops during shear tests and it is not always possible to exactly measure the voidage ε .

In this work, an estimate of the mean curvature radius δ was performed assuming material properties as Hamaker constant A and compressive strength σ_f reported in Table III.2 and a reference porosity $\varepsilon = 0.4$, according to typical values for bulk solids in compacted condition.

For this purpose, for each material, the values of the mean curvature radius δ^* which allow the best fitting of the estimated tensile strengths to the experimental values σ_t at room temperature were calculated for both elastic (δ_{el}^*) and plastic (δ_{pl}^*) case considering eq. (I.7) and eq. (I.37) in eq. (V.1) alternatively. For the elastic case, in particular, the best fitting was applied on the experimental value at lower major principal stress σ_1 , in order to verify, in the successive section, the role of porosity and compressive strength to the prediction of the change of the powder flow properties with the consolidation.

These results are summarized in Table V.1 and indicate an increasing of theoretical curvature radius from FCC powder to corundum and to glass beads respectively. These values somehow confirm what was expected by inspecting SEM images in Figure IV.1. In fact, for FCC it was expected a relevant radius of the contact point of the order of the particle roughness, which is around the micrometer. For corundum it was expected a relevant radius of the contact point of the order of the particle edges, which is few micrometers. For glass beads it was expected a relevant radius of the contact point of the order of the particle size, which is some tens of micrometers.

On the other hand, for porous alumina, despite of the high roughness of surface observed in SEM magnification in Figure IV.1d, slightly higher best fitting values δ^* were evaluated respect to a curvature radius at contact points of the order of the micrometer.

Of course, discrepancies between theoretical and experimental values may be attributed to the many simplifying assumptions adopted in the model. These results, however, confirm that this simple model provides a correct order of magnitude of the tensile strength and, therefore, a reasonable

estimate of van der Waals interactions if a plausible value of the curvature radius is taken into account.

V.2 Sensitivity analysis on the theoretical framework

In the previous section the difficulties related to finding material properties as the Hamaker constant A and the compressive strength σ_f as well as to estimate experimentally the mean curvature radius δ and the porosity ε were mentioned.

On the other hand, a quantitative evaluation on this theoretical framework was needed in order to verify the validity of the assumptions and to better understand the physical phenomena occurring between particles at high temperature.

The mean curvature radius δ was varied in order to evaluate the role of this parameter on the correct estimate of interparticle interactions and flow properties of powders. For this purpose, experimental and estimated tensile strength σ_t were compared considering:

- a perfect spherical shape and no asperities on the surface of the particles with the mean curvature radius corresponding to the radius of the particles ($\delta = d_{sv}/2$);
- a mean curvature radius δ as a fraction n of the mean Sauter diameter d_{sv} , where:

$$\delta = \frac{d_{sv}}{n} \quad (V.3)$$

In particular, the sensitivity analysis was performed for a fraction n of 20 and 100, considering both the case of elastic and plastic deformation.

The sensitivity analysis was developed also with the voidage ε . In this case, in particular, the experimental and estimated tensile strengths for best fitting mean curvature radius δ^* were compared with variations of $\pm 10\%$ than the hypothesized value of $\varepsilon = 0.4$. In fact, theory and experimental experience suggest that no large deviations of the voidage with the consolidation level occur for easy ($4 < ff_c < 10$) and free flowing powders ($ff_c > 10$) like the experimental materials. This analysis proposed to better understand if the change of flow properties with consolidation load and temperature may be imputable only to the change of voidage and thus to the variation of the number of contact points between particles inside the bulk solid or plastic deformations and the increase of the van der Waals' forces due to the presence of flattenings have to be taken into account. Also for the sensitivity analysis, the cases of elastic and plastic resistance at contact points were considered alternatively.

Finally, for the irreversible plastic case, a sensitivity analysis was carried out also for the compressive strength σ_f . This is another key parameter for which values in literature are difficult to find at room and high temperature.

Furthermore, they are often approximated and referred to unhindered condition, differently from the case of a bulk solid, where all the particles are in contact each other. To take into account it the rough correlation $p_f \approx 3\sigma_f$ was considered as previously mentioned. The analysis of the relative weight of this variable helps to understand better comprehension of the behaviour of powders inside the shear cell at room and high temperature. In this analysis, the comparison between experimental and estimated tensile strength was developed considering variations of $\pm 40\%$ of σ_f .

In the following sections the results of this sensitivity analysis are reported for each materials separately, except for fly ashes for which the unknown composition did not allow providing values for the Hamaker constant A and the compressive strength σ_f .

V.2.1 FCC powder

In Figures V.1 and V.2 the estimated tensile strength for reversible elastic and irreversible plastic behaviour are showed. In figures are not reported the cases of perfect spherical shape of particles ($\delta = d_{SV}/2$) for which values of the tensile strength σ_f about 1400 Pa was calculated. However, the sensitivity analysis for 1/20 and 1/100 of the Sauter mean diameter were carried out. This analysis confirmed that an improper value of the mean curvature radius produces significant errors in the evaluation of the tensile strength. Furthermore, an order of magnitude between 1/20 and 1/100 of the particle size are able to describe the surface properties at contact points of the particle.

Considering the best fit mean curvature radius, δ_{el}^* and δ_{pl}^* , the sensitivity analysis on the bed voidage ε was performed. Observing Figures V.3 and V.4, according also to the evidences in Figure V.2, a good estimate at room temperature of the tensile strength with the major principal stress is possible only taking into account both the decrease of voidage, plausibly due to a more compaction of the material, and the plastic deformation at contact points.

Figure V.5, as expected, shows an increase of the slope of the estimated tensile strength as the compressive strength reduces. In particular, from this figure, a decrease of the compressive strength with the temperature appears plausible.

V.2.2 Corundum

For corundum powder, the sensitivity analysis on the mean curvature radius is represented in Figures V.6 and V.7. Both the assumptions of elastic and plastic behaviour are able to described the experimental data for mean curvature radius slightly higher than 1/20 of d_{SV} , according to the results of section V.1.

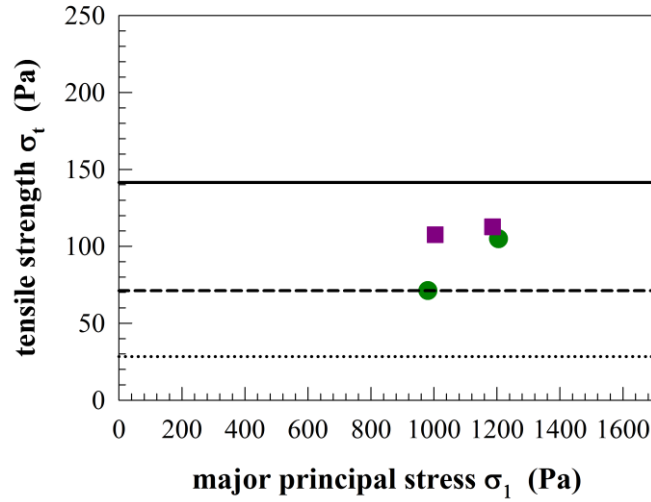


Figure V.1 FCC powder - Sensitivity analysis on the mean curvature radius δ assuming pure elastic contact. ●: $\sigma_{t,exp} - 20^\circ\text{C}$; ■: $\sigma_{t,exp} - 500^\circ\text{C}$; - - -: $\sigma_{t,el} (\delta = \delta_{el}^*)$; —: $\sigma_{t,el} (\delta = d_{SV}/20)$; ⋯: $\sigma_{t,el} (\delta = d_{SV}/100)$.

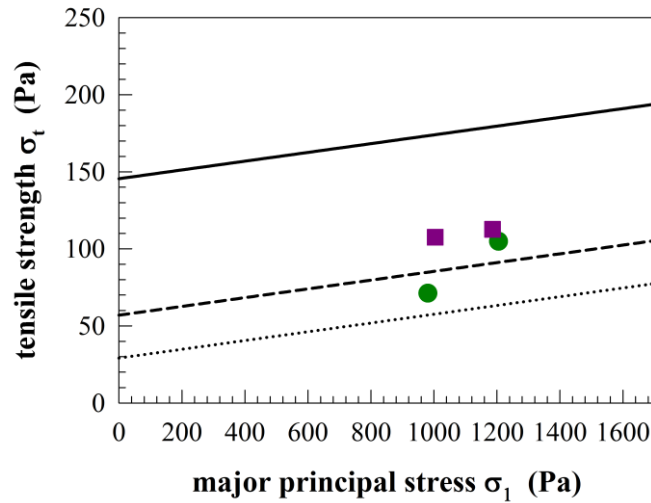


Figure V.2 FCC powder - Sensitivity analysis on the mean curvature radius δ assuming pure plastic contact. ●: $\sigma_{t,exp} - 20^\circ\text{C}$; ■: $\sigma_{t,exp} - 500^\circ\text{C}$; - - -: $\sigma_{t,pl} (\delta = \delta_{pl}^*)$; —: $\sigma_{t,pl} (\delta = d_{SV}/20)$; ⋯: $\sigma_{t,pl} (\delta = d_{SV}/100)$.

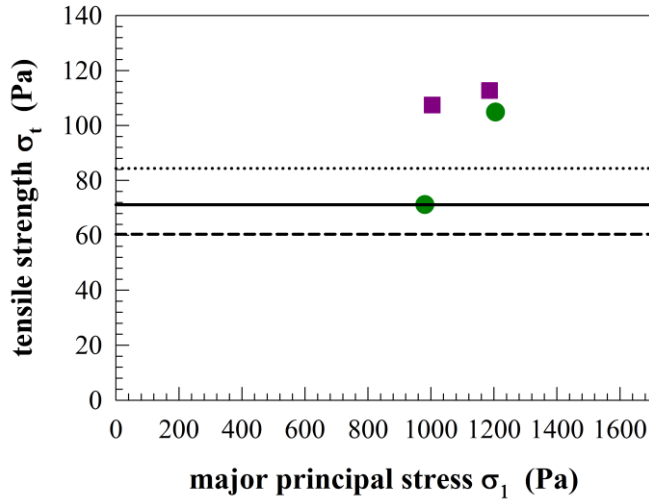


Figure V.3 FCC powder - Sensitivity analysis on the voidage ϵ assuming pure elastic contact. ●: $\sigma_{t,exp} - 20^\circ\text{C}$; ■: $\sigma_{t,exp} - 500^\circ\text{C}$; —: $\sigma_{t,el} (\delta = \delta_{el}^*; \epsilon = 0.4)$; ⋯: $\sigma_{t,el} (\epsilon = 0.36)$; - - -: $\sigma_{t,el} (\epsilon = 0.44)$.

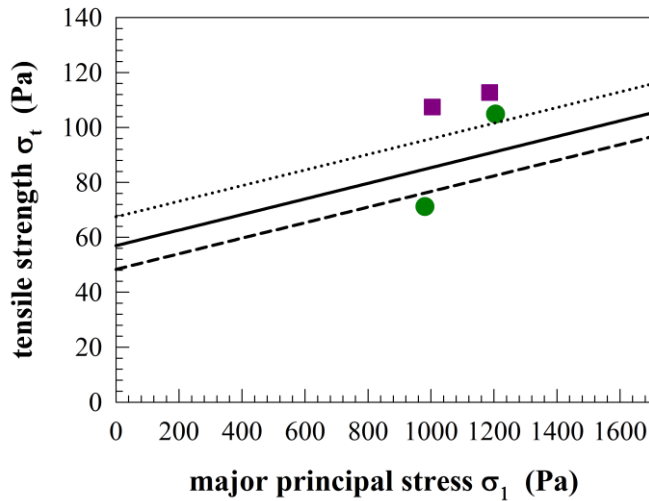


Figure V.4 FCC powder - Sensitivity analysis on the voidage ϵ assuming pure plastic contact. ●: $\sigma_{t,exp} - 20^\circ\text{C}$; ■: $\sigma_{t,exp} - 500^\circ\text{C}$; —: $\sigma_{t,pl} (\delta = \delta_{pl}^*; \epsilon = 0.4)$; ⋯: $\sigma_{t,pl} (\epsilon = 0.36)$; - - -: $\sigma_{t,pl} (\epsilon = 0.44)$.

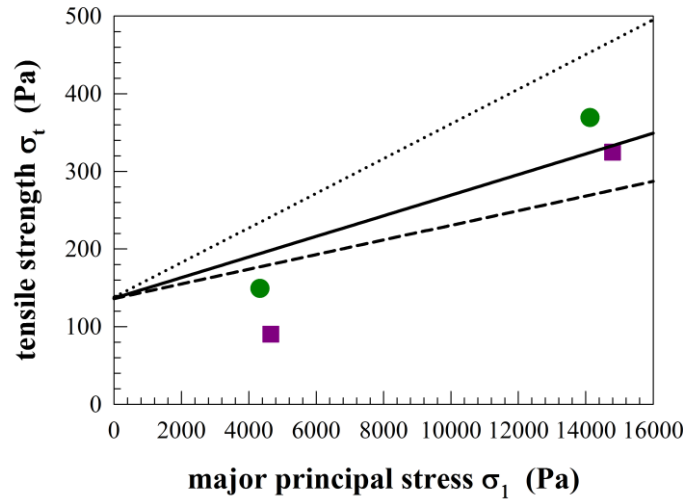


Figure V.5 FCC powder - Sensitivity analysis on the compressive strength σ_f assuming pure plastic contact. ●: $\sigma_{t,exp} - 20^\circ\text{C}$; ■: $\sigma_{t,exp} - 500^\circ\text{C}$; —: $\sigma_{t,pl} (\delta = \delta_{pl}^*)$; ⋯: $\sigma_{t,pl} (\Delta\sigma_f = +40\%)$; - - -: $\sigma_{t,pl} (\Delta\sigma_f = -40\%)$.

Experimental and predicted values have a good agreement at room temperature considering the best fit mean curvature radius δ_{pl}^* and assuming plastic deformation, as in Figure V.7. In particular with these hypotheses the increase of the tensile strength with the consolidation level was predicted. On the other hand, the decrease of voidage for the elastic case is not able to justify the enhance of the tensile strength with the major principal stress (Figure V.8).

Differently from FCC powder, the experimental tensile strength σ_t decreases with the temperature. This singular behaviour, in compliance to the adopted physical model, can be explained only making the hypothesis of increase of the voidage, as suggested by Formisani *et al.* (2002).

Finally, the experimental change of the tensile strength with temperature suggests that no significant change of the physical properties of the material occurs at high temperature for this material, as evaluated with the sensitivity analysis on the compressive strength showed in Figure V.10.

V.2.3 Alumina

The sensitivity analysis on the main parameters of the theoretical framework for porous alumina was performed and reported in following figures.

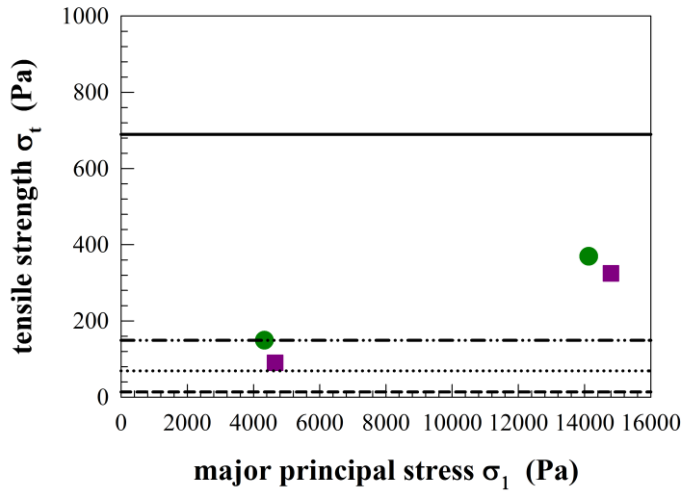


Figure V.6 *Corundum - Sensitivity analysis on the mean curvature radius δ assuming pure elastic contact.* ●: $\sigma_{t,exp} - 20^\circ\text{C}$; ■: $\sigma_{t,exp} - 500^\circ\text{C}$; —: $\sigma_{t,el} (\delta = d_{SV}/2)$;: $\sigma_{t,el} (\delta = d_{SV}/20)$; - - -: $\sigma_{t,el} (\delta = d_{SV}/100)$; - · - ·: $\sigma_{t,el} (\delta = \delta_{el}^*)$.

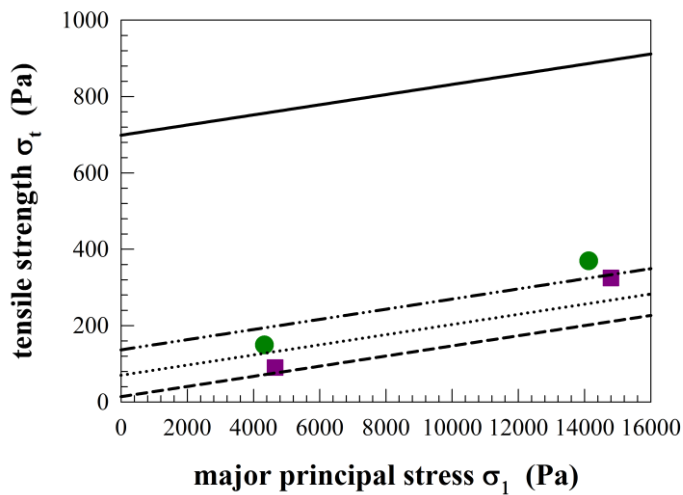


Figure V.7 *Corundum - Sensitivity analysis on the mean curvature radius δ assuming pure plastic contact.* ●: $\sigma_{t,exp} - 20^\circ\text{C}$; ■: $\sigma_{t,exp} - 500^\circ\text{C}$; —: $\sigma_{t,pl} (\delta = d_{SV}/2)$;: $\sigma_{t,pl} (\delta = d_{SV}/20)$; - - -: $\sigma_{t,pl} (\delta = d_{SV}/100)$; - · - ·: $\sigma_{t,pl} (\delta = \delta_{pl}^*)$.

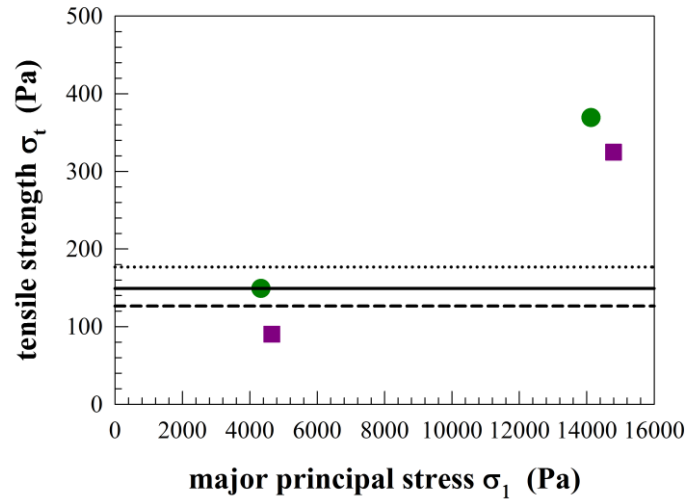


Figure V.8 Corundum - Sensitivity analysis on the voidage ε assuming pure elastic contact. ●: $\sigma_{t,\text{exp}} - 20^\circ\text{C}$; ■: $\sigma_{t,\text{exp}} - 500^\circ\text{C}$; —: $\sigma_{t,\text{el}} (\delta = \delta_{\text{el}}^*; \varepsilon = 0.4)$; ⋯: $\sigma_{t,\text{el}} (\varepsilon = 0.36)$; - - -: $\sigma_{t,\text{el}} (\varepsilon = 0.44)$.

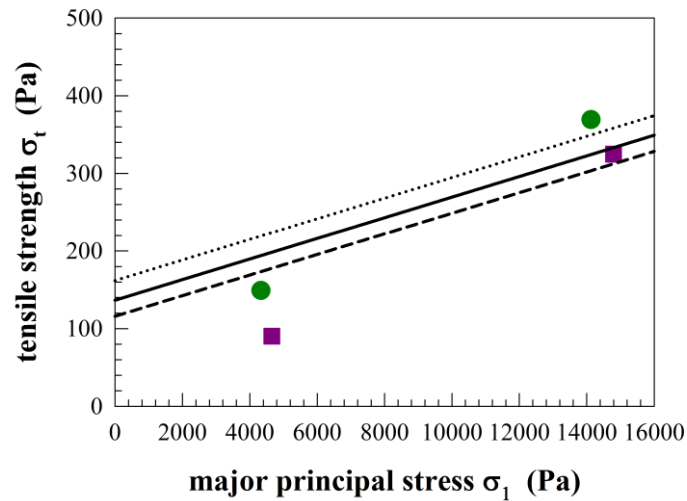


Figure V.9 Corundum - Sensitivity analysis on the voidage ε assuming pure plastic contact. ●: $\sigma_{t,\text{exp}} - 20^\circ\text{C}$; ■: $\sigma_{t,\text{exp}} - 500^\circ\text{C}$; —: $\sigma_{t,\text{pl}} (\delta = \delta_{\text{pl}}^*; \varepsilon = 0.4)$; ⋯: $\sigma_{t,\text{pl}} (\varepsilon = 0.36)$; - - -: $\sigma_{t,\text{pl}} (\varepsilon = 0.44)$.

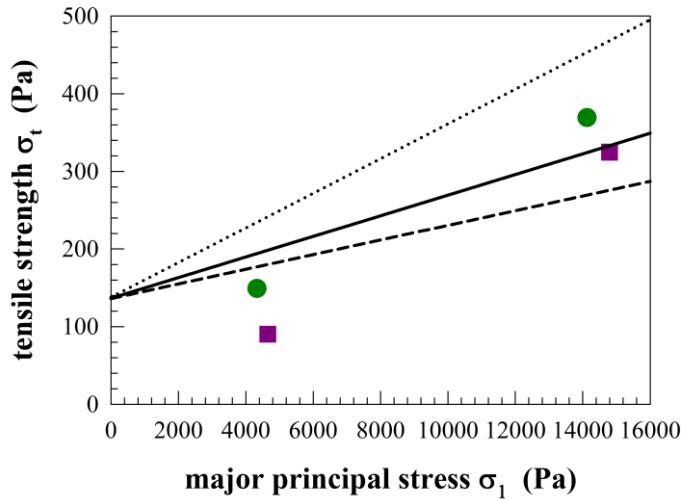


Figure V.10 Corundum - Sensitivity analysis on the compressive strength σ_f assuming pure plastic contact. ●: $\sigma_{t,exp} - 20^\circ\text{C}$; ■: $\sigma_{t,exp} - 500^\circ\text{C}$; —: $\sigma_{t,pl} (\delta = \delta_{pl}^*)$;: $\sigma_{t,pl} (\Delta\sigma_f = +40\%)$; - - -: $\sigma_{t,pl} (\Delta\sigma_f = -40\%)$.

In general, the very small variation of the experimental tensile strength with the major principal stress suggests that elastic behaviour at contact point occurs between particles, as confirmed by the good match between experimental and predicted value in Figure V.11.

As mentioned in par. V.1, a discrepancy between the best fitting mean curvature radius estimated for elastic and plastic behaviour was calculated for porous alumina. It can be also observed comparing Figures V.11 and V.12. Assuming elastic resistance at the contact point, the decrease of the 10% of the voidage seems to be sufficient to validate the small increase of the experimental tensile strength with the consolidation at room temperature (Figure V.13).

On the other hand, the hypothesis of plastic behaviour is not able to predict the tensile strength of the powder, as showed in Figures V.14 and V.15.

However, no one approach distinctly assumed is able to justify the slight increase of the tensile strength with the temperature. In this case, probably, an “intermediate” behaviour between pure elastic and pure plastic deformation can be hypothesized.

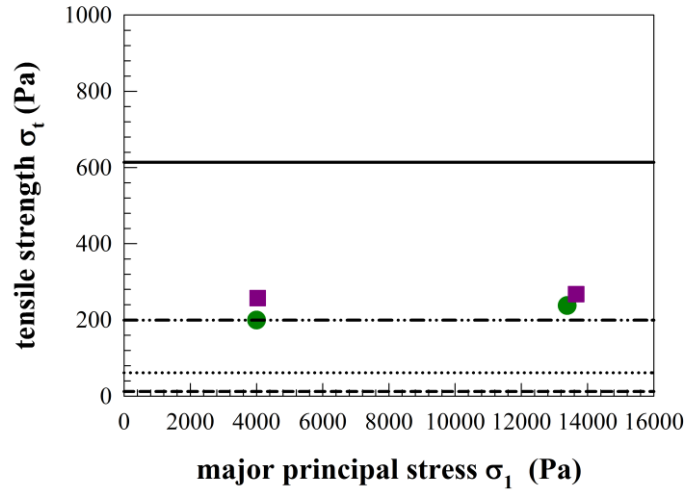


Figure V.11 Alumina - Sensitivity analysis on the mean curvature radius δ assuming pure elastic contact. ●: $\sigma_{t,\text{exp}} - 20^\circ\text{C}$; ■: $\sigma_{t,\text{exp}} - 500^\circ\text{C}$; —: $\sigma_{t,\text{el}} (\delta = d_{\text{SV}}/2)$;: $\sigma_{t,\text{el}} (\delta = d_{\text{SV}}/20)$; - - -: $\sigma_{t,\text{el}} (\delta = d_{\text{SV}}/100)$; - · - ·: $\sigma_{t,\text{el}} (\delta = \delta_{\text{el}}^*)$.

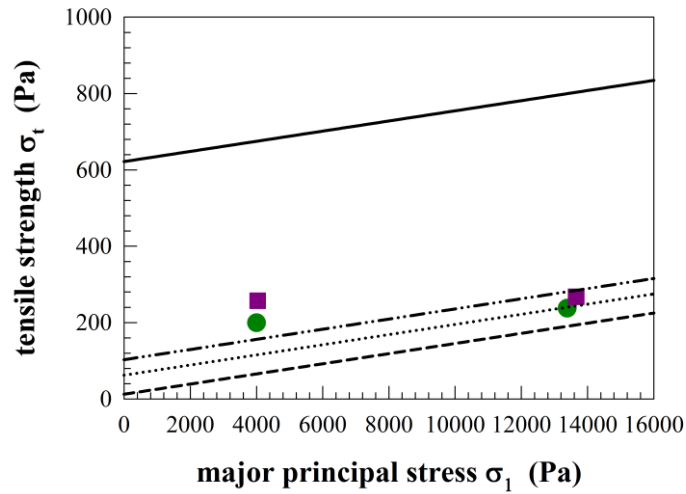


Figure V.12 Alumina - Sensitivity analysis on the mean curvature radius δ assuming pure plastic contact. ●: $\sigma_{t,\text{exp}} - 20^\circ\text{C}$; ■: $\sigma_{t,\text{exp}} - 500^\circ\text{C}$; —: $\sigma_{t,\text{pl}} (\delta = d_{\text{SV}}/2)$;: $\sigma_{t,\text{pl}} (\delta = d_{\text{SV}}/20)$; - - -: $\sigma_{t,\text{pl}} (\delta = d_{\text{SV}}/100)$; - · - ·: $\sigma_{t,\text{pl}} (\delta = \delta_{\text{pl}}^*)$.

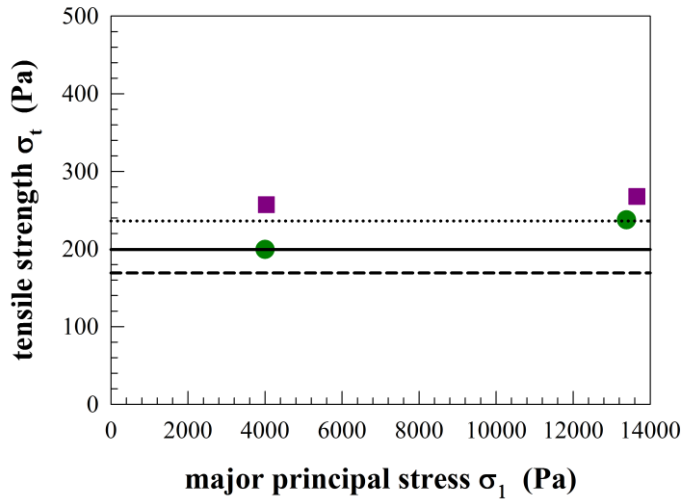


Figure V.13 Alumina - Sensitivity analysis on the voidage ε assuming pure elastic contact. ●: $\sigma_{t,exp} - 20^\circ\text{C}$; ■: $\sigma_{t,exp} - 500^\circ\text{C}$; —: $\sigma_{t,el} (\delta = \delta_{el}^*; \varepsilon = 0.4)$; ⋯: $\sigma_{t,el} (\varepsilon = 0.36)$; - - -: $\sigma_{t,el} (\varepsilon = 0.44)$.

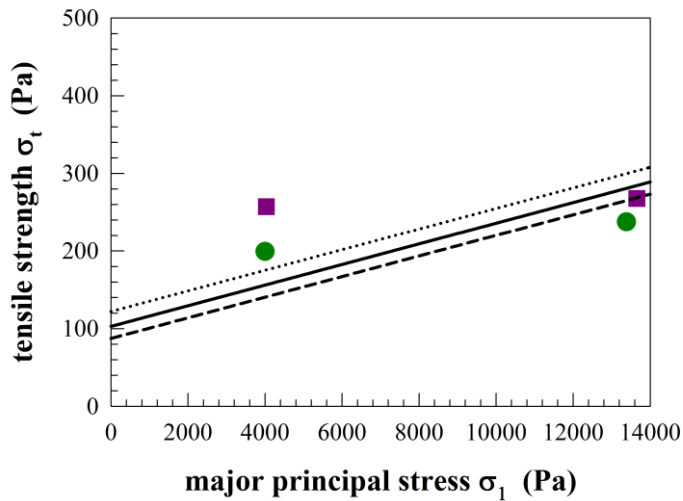


Figure V.14 Alumina - Sensitivity analysis on the voidage ε assuming pure plastic contact. ●: $\sigma_{t,exp} - 20^\circ\text{C}$; ■: $\sigma_{t,exp} - 500^\circ\text{C}$; —: $\sigma_{t,pl} (\delta = \delta_{pl}^*; \varepsilon = 0.4)$; ⋯: $\sigma_{t,pl} (\varepsilon = 0.36)$; - - -: $\sigma_{t,pl} (\varepsilon = 0.44)$.

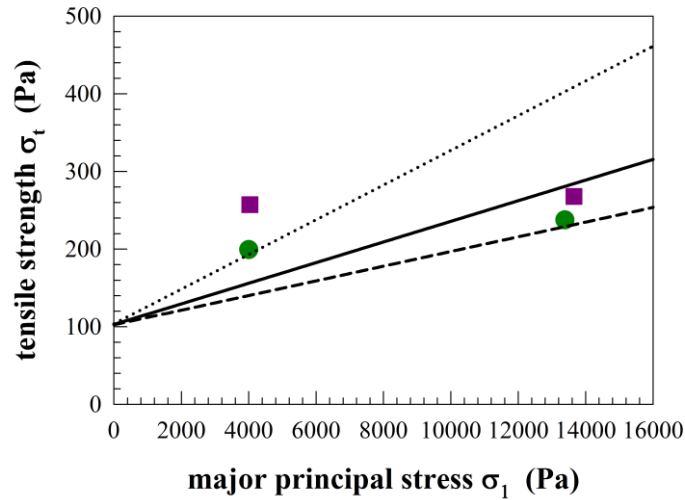


Figure V.15 Alumina - Sensitivity analysis on the compressive strength σ_f assuming pure plastic contact. ●: $\sigma_{t,exp} - 20^\circ\text{C}$; ■: $\sigma_{t,exp} - 500^\circ\text{C}$; —: $\sigma_{t,pl} (\delta = \delta_{pl}^*)$; ⋯: $\sigma_{t,pl} (\Delta\sigma_f = +40\%)$; - - -: $\sigma_{t,pl} (\Delta\sigma_f = -40\%)$.

V.2.4 Glass beads

Glass beads were chosen in this work as reference material for their perfectly spherical shape and smooth surface for which are in according to the hypotheses of Rumpf (1974) and Molerus (1985 and 1993).

The sensitivity analysis on the mean curvature radius δ confirmed the results of the best fitting mean curvature radius δ^* evaluated in previous section and of the same order of magnitude of the particle size. As showed in Figure V.16 and V.17, a mean curvature radius lower than 1/20 of the particle size underestimates the tensile strength both for elastic and plastic deformation. In this analysis the high sensitivity of the tensile strength with the curvature radius appears especially for great values of δ .

For this material, the experimental results show a slight increase of the tensile strength as the consolidation stress increases, with a more evident effect at high temperature. The sensitivity analysis on the porosity, reported in Figures V.18 and V.19 suggests that irreversible plastic behaviour becomes prominent at high temperature respect to room temperature, for which the experimental values of the tensile strength are better estimated assuming pure elastic contacts between particles. This is probably due the decrease of the compressive strength of the material with the temperature, which seems plausible observing Figure V.20.

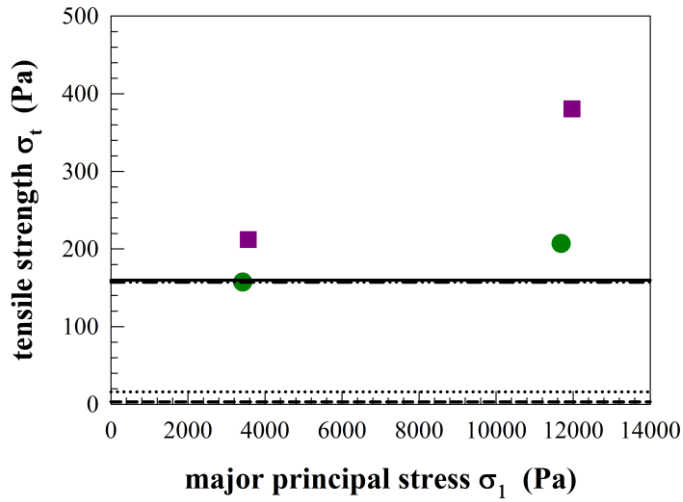


Figure V.16 Glass beads - Sensitivity analysis on the mean curvature radius δ assuming pure elastic contact. ●: $\sigma_{t,\text{exp}} - 20^\circ\text{C}$; ■: $\sigma_{t,\text{exp}} - 500^\circ\text{C}$; —: $\sigma_{t,\text{el}} (\delta = d_{\text{SV}}/2)$;: $\sigma_{t,\text{el}} (\delta = d_{\text{SV}}/20)$; - - -: $\sigma_{t,\text{el}} (\delta = d_{\text{SV}}/100)$; - · - ·: $\sigma_{t,\text{el}} (\delta = \delta_{\text{el}}^*)$.

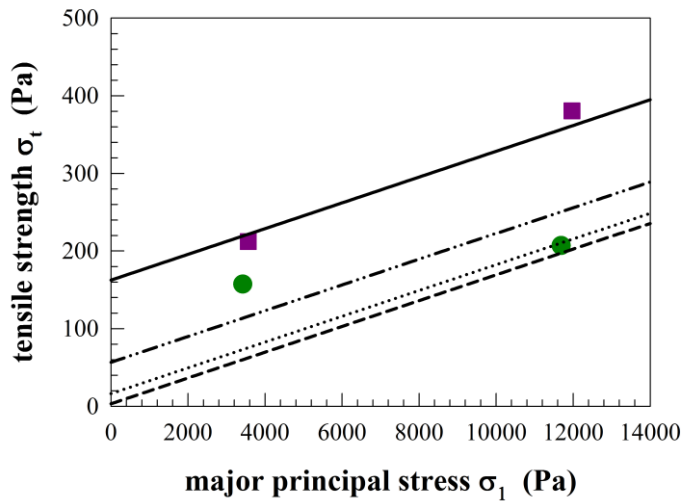


Figure V.17 Glass beads - Sensitivity analysis on the mean curvature radius δ assuming pure plastic contact. ●: $\sigma_{t,\text{exp}} - 20^\circ\text{C}$; ■: $\sigma_{t,\text{exp}} - 500^\circ\text{C}$; —: $\sigma_{t,\text{pl}} (\delta = d_{\text{SV}}/2)$;: $\sigma_{t,\text{pl}} (\delta = d_{\text{SV}}/10)$; - - -: $\sigma_{t,\text{pl}} (\delta = d_{\text{SV}}/100)$; - · - ·: $\sigma_{t,\text{pl}} (\delta = \delta_{\text{pl}}^*)$.

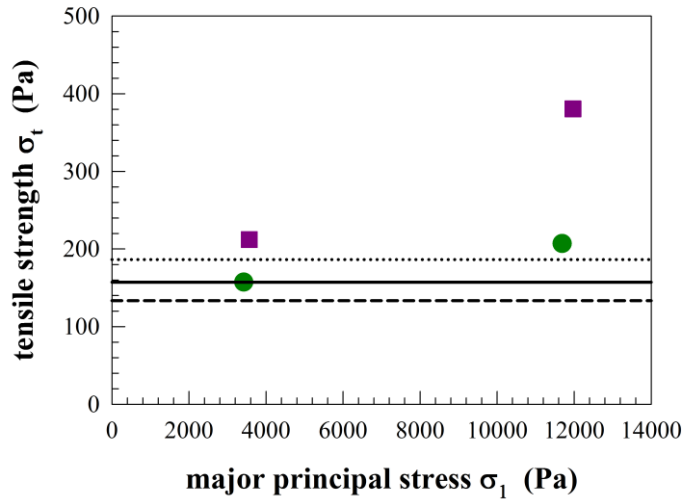


Figure V.18 Glass beads - Sensitivity analysis on the voidage ε assuming pure elastic contact. ●: $\sigma_{t,\text{exp}} - 20^\circ\text{C}$; ■: $\sigma_{t,\text{exp}} - 500^\circ\text{C}$; —: $\sigma_{t,\text{el}} (\delta = \delta_{\text{el}}^*, \varepsilon = 0.4)$; ⋯: $\sigma_{t,\text{el}} (\varepsilon = 0.36)$; - - -: $\sigma_{t,\text{el}} (\varepsilon = 0.44)$.

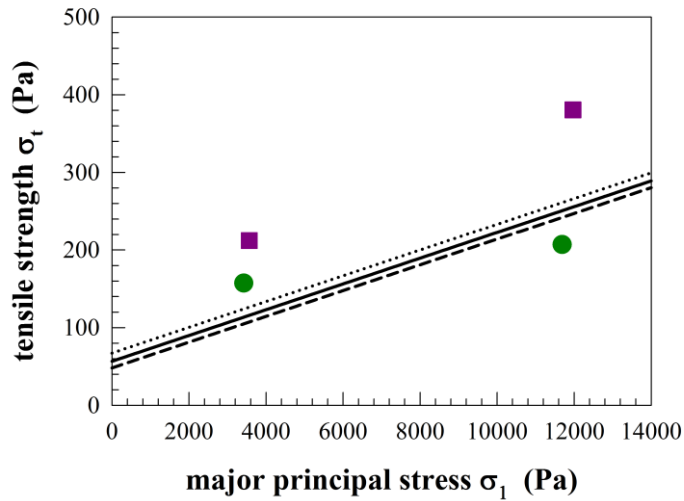


Figure V.19 Glass beads - Sensitivity analysis on the voidage ε assuming pure plastic contact. ●: $\sigma_{t,\text{exp}} - 20^\circ\text{C}$; ■: $\sigma_{t,\text{exp}} - 500^\circ\text{C}$; —: $\sigma_{t,\text{pl}} (\delta = \delta_{\text{pl}}^*, \varepsilon = 0.4)$; ⋯: $\sigma_{t,\text{pl}} (\varepsilon = 0.36)$; - - -: $\sigma_{t,\text{pl}} (\varepsilon = 0.44)$.

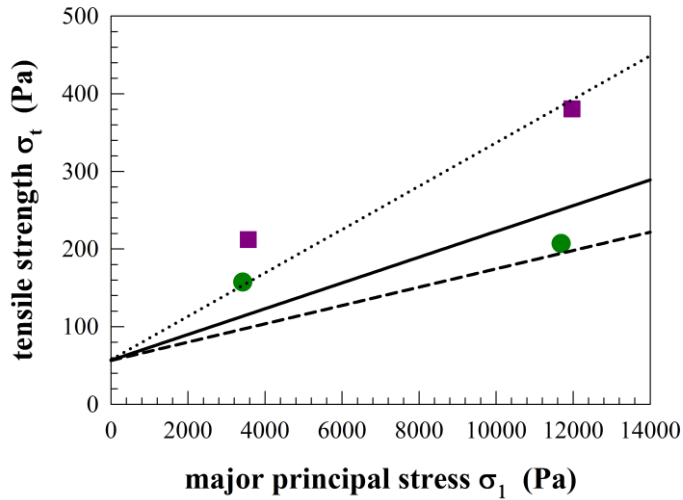


Figure V.20 Glass beads - Sensitivity analysis on the compressive strength σ_f assuming pure plastic contact. ●: $\sigma_{t,exp} - 20^\circ\text{C}$; ■: $\sigma_{t,exp} - 500^\circ\text{C}$; —: $\sigma_{t,pl} (\delta = \delta_{pl}^*)$; ⋯: $\sigma_{t,pl} (\Delta\sigma_f = +40\%)$; - - -: $\sigma_{t,pl} (\Delta\sigma_f = -40\%)$.

V.3 Discussion about the results of the sensitivity analysis

First of all, this analysis highlights the significant sensitivity of the theoretical framework from the mean curvature radius δ and the compressive strength σ_f , for which an accurate evaluation is necessary for the correct prediction of the tensile strength and the interparticle interactions.

Furthermore, the theoretical framework developed in this work provides correct order of magnitude if a plausible value of the mean curvature radius is assumed.

One of the main assumptions of the theory of Rumpf and Molerus is to consider a uniform distribution of contact force on the surface of particles. With this hypothesis, the same response occurs at each contact point, elastic or plastic, when submitted to forces and stresses, depending on these stresses exceeds or not the plastic yield of the material.

Although the original statements of the theoretical framework allowed providing correct order of magnitude of the estimated tensile strength and of the van der Waals' interactions, a different distribution of contact forces appears more correct and reasonable. Induced anisotropy during *preshear* is probably one of the more intuitive causes of non-uniform packing, distribution of stress and thus of contact force inside the bulk solid.

Let us consider a system with a non-uniform distribution of contact force submitted to the *preshear*. At this moment, elastic and plastic deformations

are distributed for all the contact points between particles. When the external consolidation load is removed, reversible elastic deformations return to the state before consolidation while flattenings at the contact surface due to the irreversible plastic deformation remain. In this case, the mean contact force attributed to van der Waals interactions F_{vdw} of eq. (V.1) cannot be estimated considering pure elastic (eq. (I.7)) or pure plastic (eq. (I.37)) behaviour, but a mean value taking into account both the case has to be considered. In other words, pure elastic and pure plastic deformations represent extreme cases of the behaviour of all the contact points of particles.

This could be the case of porous alumina, where the experimental evidences from room to high temperature represent a mid-span case between completely elastic and plastic behaviour.

For FCC powder, the sensitivity analysis suggests that the slight increase of tensile strength at high temperature was explained as the effect of the decrease of the compressive strength. In any case, this is not in agreement with the results of Xie and Geldart (1995) which asserted that variations of the properties of fluidized bed at high temperature was the result of the increase of the relative weight of the interparticle forces.

Similar conclusions were developed by Formisani *et al.* (2002) for which the increase of the bed voidage in fixed and fluidized conditions from room to high temperature for the same corundum analyzed in this work was attributed to an increase of the van der Waals' forces. Although an enhance of the cohesive behaviour of this material was not experimentally observed (par. VI.3.3), the sensitivity analysis suggested a possible increase of the porosity from room to high temperature according to the experimental findings of the authors.

According to these findings, the sensitivity analysis suggests that the increase of the cohesive behaviour with the temperature is mostly related to the plastic deformation of contact points and to the strength of the material, but could be partially compensated by an increase of powder porosity.

Finally, it is important to highlight that for glass beads for which significant change of physical properties as the compressive strength was hypothesized from room to high temperature according to the sensitivity analysis, only very small variations of the macroscopic flow properties for this material were experimentally observed.

Conclusions

This PhD work was aimed to investigate the effect of temperature on powder flow properties.

A High Temperature Annular Shear Cell (HT-ASC), originally designed at the Department of Industrial Engineering of University of Salerno, was developed and set-up in order to perform direct measurements on powder samples at high temperature.

FCC powder, commonly used as catalyst in cracking of oil, fly ashes, collected by filtering flue gas of combustion, corundum, for which literature attributed an increase of the interparticle interactions at high temperature (Formisani *et al.*, 2002), porous α -alumina and glass beads as reference material were analyzed.

The thermal behaviour of the materials was studied by Differential Scanning Calorimetry (DSC) analysis up to 500°C. From the DSC curves no melting and any phase transitions were observed for these materials. A high content of humidity was measured for FCC powder. A drying treatment in an oven at 200°C was scheduled in experimental procedure in order to remove moisture before the test. In this condition, only van der Waals' kind of interactions was considered plausible inside the powder sample without formation of liquid bridges.

Yield loci up to 500°C were measured with HT-ASC.

For FCC powder and corundum, experimental evidences did not show significant change of flow properties with the temperature. These results disagree with the literature for which change of fluidized behaviour for the same powders were found between room and high temperature, attributed to the increase of van der Waals' forces (Xie and Geldart, 1995; Formisani *et al.*, 2002).

Measured yield loci and flow functions for fly ashes up to 500°C did not show change with the temperature, according with the DSC curve of this material for which melt does not occur in this range of temperature. This is in agreement with the literature for which an increase of the cohesive behaviour due to sintering phenomena was observed only at temperature above 800°C (Kanaoka *et al.*, 2001).

Conclusions

On the other hand, for glass beads and, at a lower extent, for porous alumina, a slight increase of cohesion and of the unconfined yield strength was measured.

In general, a not univocal effect of the temperature on the macroscopic powder flow properties can be outlined.

In order to give an interpretation of the experimental evidences and to better understand the physical phenomena occurring at particle-particle level, a theoretical framework was developed according to the theory of Rumpf (1974) and Molerus (1985 and 1993). The tensile strength experimentally evaluated by shear tests was correlated to van der Waals' force acting between particles assuming pure elastic and pure plastic deformation at contact points alternatively.

Both the assumptions provided correct order of magnitude in terms of tensile strength, once a plausible value of the local curvature at contact points of particles has been taken into account by correctly considering the effect of surface roughness and asperities. The calculated best fitting values of mean curvature radius confirmed the evidences of the SEM magnifications where rough surfaces, as FCC powder and alumina, and not perfectly spherical shapes, as corundum, were observed.

A sensitivity analysis was performed on the main parameters of the theoretical framework.

This analysis suggested that the effect of consolidation at room temperature seems to be correctly predicted considering plastic deformation and the decrease of the voidage.

At high temperature, the increase of the tensile strength with the temperature was mostly related to the plastic deformation of contact points and to the mechanical properties of the material, partially compensated by an increase of powder porosity, as observed for corundum. Although an effect of the temperature on the powder flow properties did not appears clearly, the increase of the voidage with the temperature for a powder bed was in agreement with experimental findings of Formisani *et al.* (2002) about this material.

Finally, a significant increase of the macroscopic cohesive behaviour of powder with the temperature was measured in presence of a liquid phase which promoted the aggregation of the particles, as verified with shear tests and SEM magnifications performed on a prototype sample of glass beads mixed with the low-melting component high-density polyethylene powder.

It could be reasonable to hypothesize a non-uniform distribution of contact forces inside the bulk solid. Only for the contact points where the compression force exceed the elastic yield of materials a plastic deformation would occur and would explain some of the experimental results. This assumption deserves further investigations in the future.

However, the results of this PhD work are promising and encourage further studies concerning the possibility of estimating interparticle cohesive interactions from measurements of powder flow properties with shear test and to extend these results also to different compaction conditions, in particular lower ones, like those relevant to fluidization. For this purpose, the development of a mathematical model and the analysis with more powerful tools (i.e. DEM) in order to have a rigorous evaluation of the contact forces inside the shear cell would give a significant contribution in this research field also considering the occurrence of liquid bridge and aggregation.

In this research field, in parallel to the enhance in the modeling, improvements and novel technique for a more accurate evaluation of mechanical (i.e. compressive strength) and surface properties (i.e. dimensions of asperities) of particles are needed, also aimed to increase the availability of materials data.

A final suggestion for future work is the further development of the HT-ASC in order to operate at higher temperature and to extend the area of application of the novel tester to the main industrial applications using granular materials at high temperature.

References

Bergström, L., 1997, Hamaker constants for inorganic materials, *Advances in Colloid and Interface Science*, **70**, 125-169.

Bruni, G., 2005, An investigation of the influence of fines size distribution and high temperature on the fluidization behaviour of gas fluidized beds linked with rheological studies, *PhD Thesis*, University College London.

Bruni, G., Lettieri, P., Newton, D., Yates, J., 2006, The influence of fines size distribution on the behaviour of gas fluidized beds at high temperature, *Powder Technology*, **163**, 88-97.

Carman, P.C., 1954, Properties of capillary-held liquids, *The Journal of Physical Chemistry*, **57**, 56-64.

Dahneke, B., 1972, The influence of flattening on the adhesion of particles, *Journal of Colloid and Interface Science*, **40**, 1-13.

Donsì, G. and Massimilla, L., 1973, Bubble-free expansion of gas-fluidized beds of fine particles, *A.I.Ch.E. Journal*, **19**, 1104-1110.

Fisher, R. A., 1926, On the capillary forces in a idea soil: correction of formulae given by W. B. Hines, *Journal of Agriculture Science*, **16**, 492

Formisani, B., Girimonte, R., Mancuso, L., 1998, Analysis of the fluidization process of particle beds at high temperature, *Chemical Engineering Science*, **53**, 951-961.

Formisani, B., Girimonte, R., Pataro, G., 2002, The influence of operating temperature on the dense phase properties of bubbling fluidized beds of solids, *Powder Technology*, **125**, 28-38.

Geldart, D., 1973, Types of gas fluidization, *Powder Technology*, **7**, 285.

References

- Geldart, D. and Wong, A. C. Y., 1985, Fluidization of powders showing degrees of cohesiveness – II. Experiments on rates of de-aeration, *Chemical Engineering Science*, **40**, 653-661.
- Hurley, P. J., Mukherjee, B., Mann, M. D., 2006, Assessment of Filter Dust Characteristics that Cause Filter Failure during Hot-Gas Filtration, *Energy and Fuels*, **20**, 1629-1638.
- Israelaschvili, J. N., 1992, *Intermolecular and Surface Forces*, Academic Press.
- Jenike, A. W., 1964, Storage and Flow of Solids, *Bull. 123, Engineering Experiment Station*, University of Utah.
- Kamiya, H., Kimura, A., Yokoyama, T., Naito, M., Jimbo, G., 2002, Development of a split-type tensile strength and analysis of mechanism of increase of adhesion behaviour of inorganic fine powder bed at high-temperature conditions, *Powder Technology*, **127**, 239-245.
- Kanaoka, C., Hata, M., Makino, H., 2001, Measurement of adhesive force of coal flyash particles at high temperatures and different gas compositions, *Powder Technology*, **118**, 107 - 112.
- Krupp, H., 1967, Particle adhesion theory and experiment, *Advances in Colloid and Interface Science*, **1**, 211-239.
- Lifshitz, E. M., 1956, The theory of molecular attractive forces between solids, *Soviet Physics JETP*, **2**, 73-83.
- London, F., 1930, Theory and systematics of molecular forces, *Z. Phys.* **63**, 245.
- Lettieri, P., Yates, J. G., Newton, D., 2000, The influence of interparticle forces on the fluidization behaviour of some industrial materials at high temperature, *Powder Technology*, **110**, 117-127.
- Lettieri, P., Newton, D., Yates, J. G., 2001, High temperature effects on the dense phase properties of gas fluidized beds, *Powder Technology*, **120**, 34-40.
- Liu, D., Kwauk, M., Li, H., 1996, Aggregative and particulate fluidization – The two extremes of a continuo spectrum, *Chemical Engineering Science*, **51**, 4045-4063.

-
- Masuda, H., Higashitani, K., Yoshida, H., 2006, *Powder Technology Handbook*, CRC Taylor and Francis Group.
- Massimilla, L., Donsì, G., Zucchini, C., 1972, The structure of bubble-free gas fluidized beds of fine fluid cracking catalyst particles, *Chemical Engineering Science*, **27**, 2005-2015.
- Molerus, O., 1982, Interpretation of Geldart's type A, B, C and D powders by taking into account Interparticle Cohesion forces, *Powder Technology*, **33**, 81-87.
- Molerus, O., 1985, Theory of yield of cohesive powders, *Powder Technology*, **12**, 259-275.
- Molerus, O., 1993, *Principles of Flow in Disperse Systems*, Chapman and Hall.
- Mutsers, S. M. P., and Rietema, K., 1977, The effect of Interparticle Forces on the expansion of a homogenous gas-fluidized bed, *Powder Technology*, **18**, 239-248.
- Neddermann, R. M., 1992, *Statics and kinematics of granular materials*, Cambridge University Press.
- Pagliai, P., Simons, S. J. R., Rhodes, D., 2004, Towards a fundamental understanding of defluidisation at high temperatures: a micro-mechanistic approach, *Powder Technology*, **148**, 106-112.
- Pagliai, P., Simons S. J. R., Rhodes, D., 2007, A novel experimental study of temperature enhanced cohesive interparticle forces, *Powder Technology*, **174**, 71-74.
- Prieve, D. C., and Russel, W. B., 1988, Simplified predictions of Hamaker constants from Lifshitz theory, *Journal of Colloid and Interface Science*, **125**, 1-13.
- Rumpf, H., 1974, Die Wissenschaft des Agglomerierens, *Chemie Ingenieur Technik*, **46**, 1-11.
- Schubert, H., 1982, *Capillarity in porous solid material system*, Springer Verlag Berlin
- Schulze, D., 1994, Development and application of a novel ring shear tester, *Aufbereitungstechnik* 35, **10**, 524-535.

References

Seville, J., Tüzün, U., Clift, R., 1998, *Processing of Particulate Solids*, Blackie Academic & Professional.

Shackelford, J. F., Alexander, W., 2000, *Material Science and Engineering Handbook*, CRC Press.

Shamlou, P. A., 1988, *Handling of bulk solids*, Butterworth-Heinemann Ltd.

Smith, W. O., Foote, P. D., Busang, P. F., 1929, Packing of Homogenous Spheres, *Physical Review*, **34**, 1271-1274.

Standard Shear Testing Technique for Particulate Solids using the Jenike Shear Cell, 1989, The Institution of Chemical Engineers, UK

Subramani, H. J., Balaiyya, M. M. B., Miranda, L. R., 2007, Minimum fluidization velocity at elevated temperatures for Geldart's group-B powders, *Experimental Thermal and Fluid Science*, **32**, 166–173.

Van der Waals, J. D., 1873, On the continuity of liquid and gaseous states, *Ph.D. Thesis*, University of Leiden.

Visser, J., 1972, On Hamaker Constants: A comparison between Hamaker Constants and Lifshitz-van der Waals Constants, *Advances in Colloid and Interface Science*, **3**, 363.

Wang, Z., Kwauk, M., Li, H., 1998, Fluidization of fine particles, *Chemical Engineering Science*, **53**, 377-395.

Xie, H. Y., 1997, The role of interparticle forces in the fluidization of fine particles, *Powder Technology*, **94**, 99-108.

Xie, H. Y, Geldart, D., 1995, Fluidization of FCC powders in the bubble-free regime: effect of types of gases and temperature, *Powder Technology*, **82**, 269-277.

Yang, W., 2007, Modification and re-interpretation of Geldart's classification of powders, *Powder Technology*, **171**, 69-74.

List of symbols

A	Hamaker constant (J)
Ar	Archimedes number (-)
A_w	wall adhesion (Pa)
C	cohesion (Pa)
d	particle diameter (μm)
d_{SV}	Sauter mean diameter (μm)
d_{10}	10 th percentile diameter (μm)
d_{50}	volume median diameter (μm)
d_{90}	90 th percentile diameter (μm)
e_{DOWN}	difference between the set-point temperature T_{SP} and the bottom temperature T_{DOWN} ($^{\circ}\text{C}$)
e_{UP}	difference between the set-point temperature T_{SP} and the top temperature T_{UP} ($^{\circ}\text{C}$)
f_c	unconfined yield strength (Pa)
ff_c	flow factor (Pa)
F	force (N)
F_A	force exerted by balancing system in Schulze Ring Shear Tester (N)
F_c	mean isotropic contact force (N)
F_{cap}	capillary force (N)
F_{ec}	coulombic electrostatic force (N)
F_{ei}	electrostatic force induced by a charged particle (N)
F_g	gravitational force (N)
F_N	force at contact point due to the external consolidation (N)
F_{pl}	resistance force at contact point due to plastic deformation (N)
F_{vdw}	Van der Waals' force (N)
F_w	resistance force of the material at the contact point (N)
g	acceleration due to gravity (m s^{-2})
k	coordination number (-)
h	height of flattenings at contact surface (m)
H_{mf}	height of a bed of powder at minimum fluidization (m)
N	normal load applied in shear test (N)
p_f	plastic compressive yield pressure of hindered material (Pa)
P	pressure (Pa)

Listo of symbols

q	electric charge of a particle (C)
r_1	radius curvature in the plane of the meridian of the liquid bridge (m)
r_2	radius curvature in the plane orthogonal to the meridian of the liquid bridge (m)
R	particle radius (m)
Re	Reynolds number (-)
t_{DOWN}	time percentage of operation of the lower heater of HT-ASC (-)
t_{UP}	time percentage of operation of the upper heater of HT-ASC (-)
T	temperature ($^{\circ}\text{C}$)
T_{DOWN}	measured temperature at the bottom of the HT-ASC ($^{\circ}\text{C}$)
T_{MID}	measured temperature in the middle of the HT-ASC ($^{\circ}\text{C}$)
T_{SP}	set-point temperature of the HT-ASC ($^{\circ}\text{C}$)
T_{UP}	measured temperature on the top of the HT-ASC ($^{\circ}\text{C}$)
u_{mb}	minimum bubbling velocity (m s^{-1})
u_{mf}	minimum fluidization velocity (m s^{-1})
z	separation distance between particles (m)
z_0	separation distance between particles usually assumed in air (m)

Greek letters

α	half-angle of the liquid bridge (deg)
β	angle defining a generic plane in the Mohr's circle (deg)
δ	mean curvature radius at contact surface (m)
δ^*	best fitting mean curvature radius at contact surface (m)
ε	voidage of the bulk solid (-)
ε_i	inner voidage of a particle (-)
ε_{mf}	voidage of a bed of powder at minimum fluidization (-)
ϕ	angle of internal friction (deg)
ϕ_e	effective angle of internal friction (deg)
ϕ_w	angle of wall friction (deg)
η	viscosity of the fluidizing gas (or fluid) ($\text{kg m}^{-1} \text{s}^{-1}$)
λ	angle of the principal planes in the Mohr's circle (deg)
μ	coefficient of internal friction (-)
μ_w	coefficient of wall friction (-)
θ	contact angle of the liquid on a surface (deg)
ρ_b	bulk density (kg m^{-3})
ρ_f	fluid density (kg m^{-3})
ρ_p	particle density (kg m^{-3})
ρ_s	solid density (kg m^{-3})
σ	normal stress (Pa)
σ_c	normal stress of <i>preshear</i> in shear test (Pa)
σ_f	compressive yield strength (Pa)
σ_i	normal stress on a plane orthogonal to <i>i</i> -direction (Pa)
σ_s	surface tension (Pa)

σ_t	tensile strength (Pa)
σ_w	normal stress at the wall (Pa)
σ_1	major principal stress (Pa)
σ_2	minor principal stress (Pa)
τ	shear stress (Pa)
τ_c	shear stress of <i>preshear</i> in shear test(Pa)
τ_{ij}	shear stress in <i>j</i> -direction exerted on a plane orthogonal to <i>i</i> -direction (Pa)
τ_w	shear stress at the wall (Pa)
ξ	dielectric constant (F m ⁻¹)
ξ_0	dielectric constant of the free space (C ² N ⁻¹ m ⁻¹)
ξ_r	relative dielectric constant (-)
ψ	sphericity of a particle (-)

Subscripts

el	estimated value assuming elastic deformation
exp	experimental value
pl	estimated value assuming plastic deformation

Appendix A

The exact analysis of the transmission of stresses in a packed bed

In the following, the exact analysis of Molerus (1993) concerning with the transmission of stresses in a randomly packed bed of monodisperse spheres is reported.

According to the hypothesis of par. I.6, assuming the equal probability of contact point over the sphere surface, the average number of contacts per surface element dA_s of a sphere may then be computed as:

$$dK = k \frac{dA_s}{4\pi R^2} \quad (\text{A.1})$$

Let us consider the transmission of an isostatic stress σ through an arbitrarily oriented plane AA, cutting an arbitrary sphere and which is distant ξ from the centre of the sphere, as represented in Figure A.1. It can be defined the absolute number of particles with centers distant from the plane AA between ξ and $\xi + d\xi$ as:

$$n(\xi) = \frac{n}{R} d\xi \quad (\text{A.2})$$

where n is the total number of particles cut by plane AA.

The total compressive force transmitted by particles with centers distant from the plane AA in the interval $(\xi, \xi + d\xi)$ then follows from eqs. (A.1) and (A.2), according to Figure A.1:

$$dF = \left(\frac{k}{4\pi R^2} \int_{A_s} F_N \cos \alpha dA_s \right) \frac{n}{R} d\xi \quad (\text{A.3})$$

According to Figure A.1:

$$\int_{A_s} \cos \alpha dA_s = \int_{A_\xi} dA_\xi = \pi(R^2 - \xi^2) \quad (\text{A.4})$$

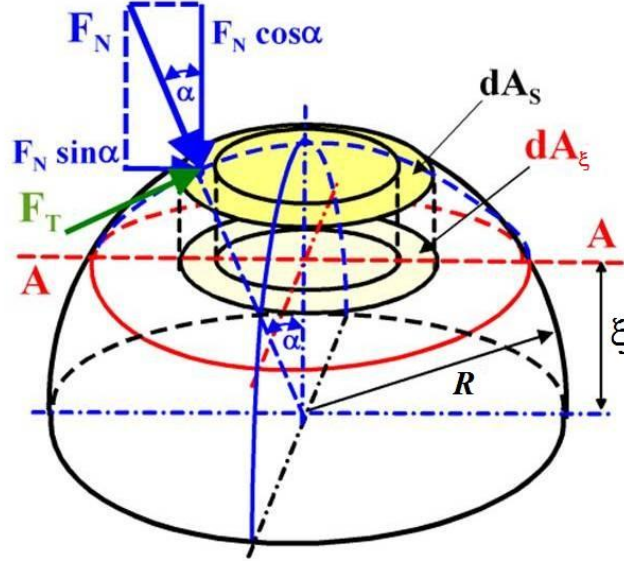


Figure A.1 Force in an interparticle contact (Molerus, 1993).

from eq. (A.3), considering the assumption of uniform distribution of forces on the contact surface, follows:

$$dF = \frac{knF_N \pi (R^2 - \xi^2)}{4\pi R^3} d\xi \quad (\text{A.5})$$

The compressive normal force transmitted in the cross-section AA of the packing is then:

$$F = \frac{knF_N}{4R^3} \int_0^R (R^2 - \xi^2) d\xi = \frac{knF_N}{6} \quad (\text{A.6})$$

The area of particle cut by the plane AA having the distance with the centers in the interval $(\xi, \xi + d\xi)$ is:

$$dA_C = \pi (R^2 - \xi^2) \frac{n}{R} d\xi \quad (\text{A.7})$$

Consequently, the total area of the cut particles in the plane AA is:

$$A_C = \frac{n\pi}{R} \int_0^R (R^2 - \xi^2) d\xi = n \frac{2\pi R^2}{3} \quad (\text{A.8})$$

According to the hypothesis of random packing, assuming volume void fraction ε equal to the area void fraction, it follows that the total area of the cut plane AA through which the force is transmitted is equal to:

$$A = \frac{A_C}{(1-\varepsilon)} = n \frac{2\pi R^2}{3(1-\varepsilon)} \quad (\text{A.9})$$

The isostatic normal compressive stress $\sigma = F/A$ is given by:

$$\sigma = \frac{F_N}{4R^2} \frac{k(1-\varepsilon)}{\pi} \quad (\text{A.10})$$

which, with $R = d/2$, and considering contact force F_c transmitted only by normal interactions, is equivalent to eq. (I.32).